

General Disclaimer

One or more of the Following Statements may affect this Document

- This document has been reproduced from the best copy furnished by the organizational source. It is being released in the interest of making available as much information as possible.
- This document may contain data, which exceeds the sheet parameters. It was furnished in this condition by the organizational source and is the best copy available.
- This document may contain tone-on-tone or color graphs, charts and/or pictures, which have been reproduced in black and white.
- This document is paginated as submitted by the original source.
- Portions of this document are not fully legible due to the historical nature of some of the material. However, it is the best reproduction available from the original submission.

(NASA-CR-158641) HIGH-EFFICIENCY THIN-FILM
GaAs SOLAR CELLS Final Report (Jet
Propulsion Lab.) 99 p HC A05/MF A01 N79-24463

CSCl 10A

G3/44

Unclassified
22331

High-Efficiency Thin-Film GaAs Solar Cells

Final Report

Richard J. Stirn

April 15, 1979

Prepared for
U.S. Department of Energy
Through an agreement with
National Aeronautics and Space Administration
by

Jet Propulsion Laboratory
California Institute of Technology
Pasadena, California



High-Efficiency Thin-Film GaAs Solar Cells

Final Report

Richard J. Stirn

April 15, 1979

Prepared for
U.S. Department of Energy
Through an agreement with
National Aeronautics and Space Administration
by
Jet Propulsion Laboratory
California Institute of Technology
Pasadena, California

ABSTRACT

A continuation of a solar cell research task previously funded by ERDA was initiated March 1, 1978 for the Department of Energy. The overall objective is to demonstrate the feasibility of producing high-efficiency (15% or greater) thin-film gallium arsenide (GaAs) solar cells with costs suitable for terrestrial power generation. The approach is that of growing GaAs by organo-metallic chemical vapor deposition (OM-CVD) on recrystallized germanium (Ge) films previously deposited on metal substrates, and fabricating AMOS (Anti-reflecting Metal-Oxide-Semiconductor) solar cells on the GaAs. New work will investigate CVD-grown n/p homojunction GaAs solar cells on the large-grain Ge layers.

Studies of the interfacial oxide layer of AMOS single-crystal solar cells emphasized the formation and stability of vacuum-deposited non-native oxides. High evaporation temperatures and stoichiometry control problems suggested flash evaporation by pulsed laser beams. Several oxides, including Cr₂O₃, Al₂O₃, and SiO₂, were investigated using a 50-watt Co₂ laser in both pulsed and CW-mode operation. Difficulties with film-thickness monitoring precluded reproducible results or optimization; however, conversion efficiencies of about 15% were observed. After about 6 months exposure to laboratory air, SiO₂-AMOS solar cells showed negligible degradation, while cells fabricated with Al₂O₃ and Cr₂O₃ degraded substantially. Variations in sheet resistance for the Schottky barrier (SB) metallization were observed between the different oxides due to differing nucleation properties.

Experiments with gallium/silver (Ga/Ag) SB metallization for stability testing were inconclusive due to difficulties in handling the alloy for flash evaporation. Initial barrier heights, and hence efficiencies, were somewhat reduced using 12%-Ga/88%-Ag alloy, with varying reproducibility.

Continuing lifetesting experiments at elevated temperatures show promising results, particularly for native oxide (grown in water vapor-saturated oxygen) and MoO₃-deposited oxide AMOS solar cells. Degradation in efficiency, primarily in open-circuit voltage, is less than 15% and 10%, respectively, after nearly 14 months at 100 C. Ancillary experiments indicate a potential life of 20 years at room temperature for Sb₂O₃-oxides--the type showing the highest degradation rate. All experiments, however, were performed under non-illuminated, unloaded conditions.

Germanium recrystallization studies using spot-scanned Nd/YAG laser beams showed that multiple passes with the spot improved the surface morphology and decreased the etch-pit density. Largest grain-development occurred with the highest laser and background-heating levels, but metallurgical reactions with the tungsten (W) coating at these levels caused the appearance of W micro-precipitates at the Ge surface. Experiments at the Spire Corporation with pulsed e-beams resulted in Ge grain sizes of only about 10 μm . Subcontracted studies with Chemetal Corporation showed that CVD-W coatings on Ni-plated steel did not properly passivate the steel against reaction with the Ge.

However, a finer-grain, 1% carbon-in-tungsten CVD coating showed considerably more promise. Estimated add-on costs for a 2 μm coating are about \$0.56 per ft^2 for WF_6 or \$0.40 per ft^2 for WC_{16} starting materials for the CVD process.

GaAs CVD growth on single-crystal GaAs substrates was investigated over a temperature range of 600 to 750 $^\circ\text{C}$, As/Ga mole-ratio range of 3 to 11, and gas mole-fraction range of 5×10^{-9} to 7×10^{-7} for H_2S doping. The highest Hall mobilities of $7800 \text{ cm}^2/\text{V}\cdot\text{s}$ at room temperature ($41,000 \text{ cm}^2/\text{V}\cdot\text{s}$ at 77 K) were obtained for 700 $^\circ\text{C}$ and an As/Ga mole ratio of 5. Evidence of impurity conduction at low temperatures appeared when the As/Ga ratio was equal to 8 or larger. The electron carrier concentration was found to vary linearly with H_2S mole fraction over 2 orders of magnitude above a mole fraction of 10^{-8} (for which $n = 1 \times 10^{15} \text{ cm}^{-3}$).

GaAs CVD growth on recrystallized Ge films was investigated for a temperature range of 550 to 700 $^\circ\text{C}$, an As/Ga mole ratio of 5, and for various H_2S mole fractions. The surfaces contained faceted large grains correlating with the Ge grains, but there were regions where smaller grain-growth predominates. The latter regions, which contain fewer etch pits, had the highest breakdown voltages, but lowest short-circuit current densities (I_{sc}). AMOS solar cells fabricated on GaAs films grown at temperatures near or just above 600 $^\circ\text{C}$ show little tendency for shunting, but exhibited lower I_{sc} values than cells made on GaAs grown at 650-700 $^\circ\text{C}$. In general, the values of I_{sc} for individual 2-mm dots in an array of dots were low at the leading edge of the gas flow, increasing toward the opposite edge.

Copper contamination from the e-gun hearth is a problem when evaporating Ge films. Hence, a germane (GeH_4) source was recently added to the CVD facility. Experiments are now underway to optimize the Ge growth on W and W-coated steel and to assure strong bonding between the Ge and W during subsequent recrystallization and GaAs growth.

Schottky barrier solar cells were fabricated on a number of polycrystalline GaAs films, usually using a dot array for uniformity studies. Correlations were seen between I_{sc} and the CVD gas-flow direction relative to the laser-scan direction. Furthermore, the lowest values of I_{sc} occur at the leading edge (upstream side), increasing toward the opposite edge. Samples made on GaAs grown near the low end of the temperature range ($\sim 600 \text{ }^\circ\text{C}$) had poor values of I_{sc} , but showed no shunting effects -- opposite to that observed for growth temperatures above 650 $^\circ\text{C}$.

SEM photographs using the EBIC mode clearly show variations in response, with induced-current values in the highest-response regions equal to those obtained with single-crystal GaAs samples. Correlations between the laser-scan pattern and the localized induced-current response can be seen. The highest efficiency cell observed on these films with 2-mm dots was 4.8% (8% when AR-coated). Improvements in fill factor and open-circuit voltage by about 40% each are required in order to obtain efficiencies of 15% or greater.

CONTENTS

| | | |
|------------------|---|------|
| I. | INTRODUCTION ----- | 1-1 |
| II. | AMOS SOLAR CELL RESEARCH ----- | 2-1 |
| A. | INTERFACIAL LAYER FORMATION ----- | 2-1 |
| 1. | Native Oxide ----- | 2-2 |
| 2. | Deposited Oxide ----- | 2-3 |
| B. | METALLIZATION ----- | 2-14 |
| C. | LIFE TESTING ----- | 2-16 |
| III. | THIN-FILM POLYCRYSTALLINE GaAs ----- | 3-1 |
| A. | GERMANIUM RECRYSTALLIZATION ----- | 3-1 |
| 1. | Recrystallization ----- | 3-1 |
| 2. | Substrate Passivation ----- | 3-9 |
| B. | GaAs GROWTH ON GERMANIUM LAYERS ----- | 3-17 |
| 1. | Properties of OM-CVD GaAs Grown on Single-Crystal GaAs ----- | 3-17 |
| 2. | GaAs Growth on Recrystallized Germanium Thin Films ----- | 3-34 |
| C. | THIN-FILM POLYCRYSTALLINE SOLAR CELLS ----- | 3-44 |
| REFERENCES ----- | | 3-56 |
| APPENDIX ----- | | A-1 |

Figures

| | | |
|-------|--|------|
| 1-1. | Thin-Film GaAs AMOS Solar Cell ----- | 1-2 |
| 2-1. | Photograph of Laser Deposition System ----- | 2-5 |
| 2-2. | Light I-V Characteristics for an AMOS Solar Cell with Al_2O_3 Laser- Deposited Oxide ----- | 2-10 |
| 2-3. | Light I-V Characteristics for an AMOS Solar Cell with SiO_2 Laser- Deposited Oxide ----- | 2-11 |
| 2-4. | Light I-V Characteristics for an AMOS Solar Cell with Cr_2O_3 Laser- Deposited Oxide ----- | 2-12 |
| 2-5. | Results of 100 C Exposure in the Dark of Three AMOS Solar Cells Without Intentional Oxide Layer ----- | 2-18 |
| 2-6. | Results of 100 C Exposure in the Dark of Three AMOS Solar Cells Fabricated with 38-Å Deposited Sb_2O_3 ----- | 2-19 |
| 2-7. | Stability of V_{oc} with 100 C Exposure in the Dark for Several Types of AMOS Solar Cells ----- | 2-20 |
| 2-8. | Stability of Fill Factor with 100 C Exposure in the Dark ----- | 2-22 |
| 2-9. | Results of 100 C Exposure in the Dark on Reverse Saturation Current Density ----- | 2-23 |
| 2-10. | Results of 100 C Exposure in the Dark on the Diode Ideality Factor ----- | 2-24 |
| 3-1. | Influence of Background Heating on Grain Size of Recrystallized Ge ----- | 3-4 |
| 3-2. | Low-Magnification SEM Photograph of Recrystallized Ge Film with Single Laser Pass ----- | 3-6 |
| 3-3. | Low-Magnification SEM Photograph of Recrystallized Ge Film with Three Laser Passes ----- | 3-6 |
| 3-4. | High-Magnification SEM Photograph of Recrystallized Ge Film with Single Laser Pass ----- | 3-7 |
| 3-5. | High-Magnification SEM Photograph of Recrystallized Ge Film with Three Laser Passes ----- | 3-7 |
| 3-6. | SEM Photograph of Pulsed e-Beam Melted Ge on Tungsten Substrate ----- | 3-9 |

Figures (continued)

| | |
|--|------|
| 3-7. SEM Photograph of Low Laser-Power (50 W) Recrystallized Ge/W/Ni ----- | 3-12 |
| 3-8. SEM Photograph of High Laser-Power (80 W) Recrystallized Ge/W/Ni ----- | 3-12 |
| 3-9. Cross-section Photomicrograph of Recrystallized Ge/Si/W/Ni Substrate with High Background Heating (530 C) and High Laser-Power (80 W) ----- | 3-13 |
| 3-10. Elemental Map of Sample in Figure 3-9 ----- | 3-14 |
| 3-11. SEM Photograph of Ge Recrystallized on CM500/W/Ni/1018 Steel Substrate ----- | 3-16 |
| 3-12. Photograph of JPL OM-CVD Facility ----- | 3-18 |
| 3-13. Typical SEM Photomicrograph of GaAs Grown on Single-Crystal GaAs Substrate with As/Ga Ratio of Less than 3 ----- | 3-20 |
| 3-14. Temperature Dependence of Resistivity of OM-CVD GaAs Layers ----- | 3-22 |
| 3-15. Temperature Dependence of Hall Coefficient of OM-CVD GaAs Layers ----- | 3-23 |
| 3-16. Temperature Dependence of Hall Mobility of OM-CVD GaAs Layers ----- | 3-25 |
| 3-17. Temperature Dependence of Carrier Concentration of OM-CVD GaAs Layers ----- | 3-26 |
| 3-18. Carrier Concentration vs Hydrogen Sulfide Concentration for OM-CVD GaAs ----- | 3-32 |
| 3-19. Mobility and Compensation Ratio of S-doped and Undoped OM-CVD GaAs ----- | 3-33 |
| 3-20. Cross-Section Photomicrograph of GaAs Thin Film Grown on Ge/W Substrate ----- | 3-37 |
| 3-21. Elemental Map of Sample in Figure 3-20 ----- | 3-38 |
| 3-22. Low-Magnification SEM Photograph of GaAs Thin Film Grown on Ge/W Substrate at 650 C ----- | 3-40 |
| 3-23. High-Magnification SEM Photograph of a Low-Breakdown-Voltage Region Inside Figure 3-22 ----- | 3-40 |

Figures (continued)

| | |
|---|------|
| 3-24. High-Magnification SEM Photograph of a High-Breakdown-Voltage Region Inside Figure 3-22 ----- | 3-41 |
| 3-25. Low-Magnification SEM Photograph of a Region with Low Short-Circuit Current ----- | 3-42 |
| 3-26. High-Magnification SEM Photograph of Sample in Figure 3-25 ----- | 3-43 |
| 3-27. Optical Photograph of Thin-Film GaAs Solar Cells Dot Array ----- | 3-45 |
| 3-28. Diagram of Resulting Photovoltaic Parameters of Sample in Figure 3-27 ----- | 3-46 |
| 3-29. EBIC Photograph (36X) of Region with Poor Short-Circuit ----- | 3-48 |
| 3-30. SEM Photograph of Same Region Shown in Figure 3-29 (36X) ----- | 3-48 |
| 3-31. EBIC Photograph (36X) of Region with Fair Short-Circuit Current ----- | 3-50 |
| 3-32. SEM Photograph of Region Shown in Figure 3-31 (36X) ----- | 3-50 |
| 3-33. Magnified EBIC Photograph of the Region Shown in Figure 3-31 (120X) ----- | 3-51 |
| 3-34. SEM Photograph of the Region Shown in Figure 3-33 (120X) ----- | 3-51 |
| 3-35. Higher-Magnification EBIC Photograph of the Region Shown in Figure 3-31 (3000X) ----- | 3-52 |
| 3-36. SEM Photograph of the Region Shown in Figure 3-35 (3000X) ----- | 3-52 |
| 3-37. EBIC Current Signals Derived From the Three Different Line Locations Shown in Figure 3-31 as Bright Lines ----- | 3-53 |
| 3-38. Light I-V of the Best Small-Area, Thin-Film AMOS Solar Cell in the Array of Figure 3-27 ----- | 3-55 |

Tables

| | |
|---|------|
| 2-1. Summary of Laser Deposited Al ₂ O ₃ AMOS Cells ----- | 2-7 |
| 2-2. Summary of Laser Deposited SiO ₂ AMOS Cells ----- | 2-8 |
| 2-3. Summary of Laser Deposited Cr ₂ O ₃ AMOS Cells ----- | 2-8 |
| 2-4. Life Test of H ₂ O/O ₂ Oxide AMOS Cell in N ₂ at 205 C in the Dark ----- | 2-25 |
| 3-1. Electrical Parameters of OM-CVD GaAs Samples With As/Ga Mole Ratio of 5, 8, 11 at 300 and 77 K ----- | 3-29 |
| 3-2. Estimates of Compensation Ratio K, Using T-fit, Wolfe, or Rode Method ----- | 3-30 |
| 3-3. Typical Doping Concentrations for Single and Polycrystalline GaAs Films Obtained from C-V Measurements ----- | 3-43 |

DEFINITION OF ABBREVIATIONS

| | |
|------|--|
| AMOS | Antireflecting Metal-Oxide-Semiconductor |
| CVD | Chemical Vapor Deposition |
| CW | Continuous Wave |
| EBIC | Electron Beam-Induced Current |
| EDAX | Energy Dispersive Analysis of X-ray |
| FF | Fill Factor |
| PL | Passivation Layer |
| SEM | Scanning Electron Microscope |
| TM | Thickness Monitor |
| XPS | X-ray Photoelectron Spectroscopy |

SECTION I

INTRODUCTION

A solar-cell research task was begun in January 1976, under NSF/RANN funding, with the following objectives: (1) to investigate the feasibility of growing large-grain polycrystalline gallium arsenide (GaAs) films by chemical vapor deposition on laser beam recrystallized germanium (Ge) layers, (2) to fabricate AMOS (Antireflecting Metal-Oxide-Semiconductor) solar cells on the polycrystalline layers (Figure 1), and (3) to investigate the physics and chemistry of the oxide-GaAs interface on single-crystal GaAs. Technical overview of the task was transferred to the Division of Solar Energy of the then-existing Energy Research and Development Administration in August, 1976. A final report has been completed (Ref. 1) describing concepts of the device structure and processing, material availability and cost considerations, results of studies on a variety of oxidation techniques, X-ray photoelectron spectroscopy (XPS) results of the interface chemistry, and effects of melting Ge films on tungsten substrates with line-focused heat lamps and Nd/YAG laser beams.

A new task was initiated March 1, 1977, under ERDA/NASA Inter-agency Agreement EG-77-A-29-1074 for the Division of Solar Energy, which is now the Division of Distributed Solar Technology in the Department of Energy. The task was, in part, a continuation of the previous NSF task, with an overall objective of demonstrating the feasibility of producing high-efficiency (15% or greater) thin-film GaAs solar cells with costs suitable for terrestrial solar electric power generation.

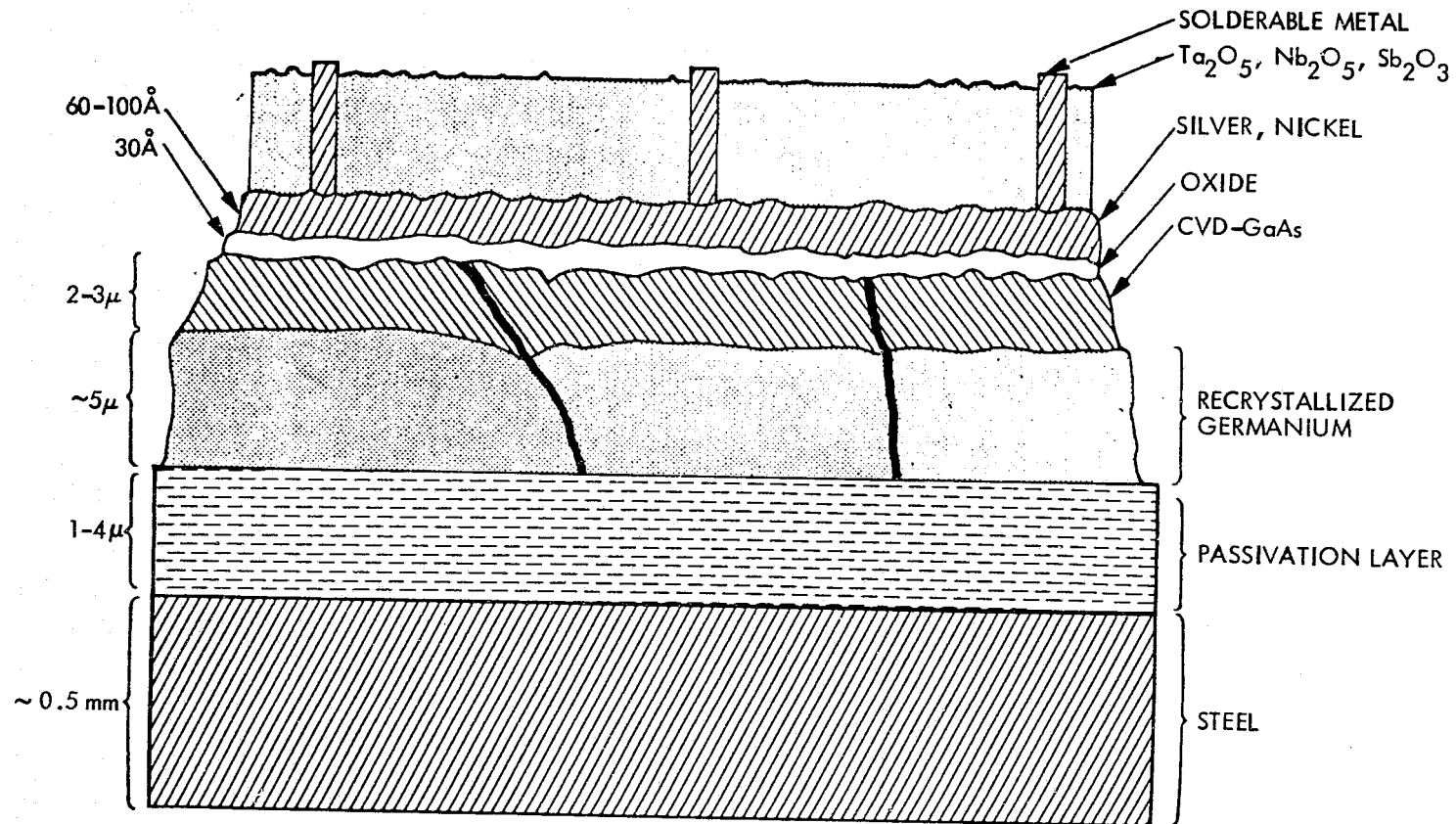


Figure 1-1. Thin-Film GaAs AMOS Solar Cell

Two reports (Refs. 2 and 3) described progress during that task, detailing: (1) improvements in the water vapor-grown native oxide process; (2) a deposited non-native oxide process which further improved the initial conversion efficiency; (3) metal substitutes for gold; (4) expanded analytical studies of the AR coating; (5) a new chemical etchant for depth profiling the native oxide; (6) a double layer Schottky barrier solar cell concept which can lead to efficiencies up to 16% without oxide interfacial layers and to 20-22% with such layers; (7) AMOS solar cell fabrication on sliced polycrystalline GaAs wafers having up to 14% cell efficiency; (8) unsuccessful attempts to recrystallize Ge films on non-treated metal substrates other than tungsten; and (9) preliminary results of chemical vapor deposition (CVD) GaAs films grown on the recrystallized Ge layers.

A follow-on task was initiated March 1, 1978, under the same Interagency Agreement for the Division of Distributed Solar Technology, Department of Energy. Technical overview of the task was transferred to the Solar Energy Research Institute, Golden, Colorado in July, 1978. This report summarizes the activities for the period from March 1, 1978 to February 28, 1979.

SECTION II
AMOS SOLAR CELL RESEARCH

A. INTERFACIAL LAYER FORMATION

Prior to this reporting period, it had been established that high conversion efficiency could be achieved with single-crystal AMOS GaAs solar cells. During this reporting period, the primary emphasis has been on the stability of the AMOS solar cells and, of course, on its application to thin films, rather than on further improvement of the conversion efficiency. The ultimate goal of this task is to demonstrate the feasibility of low-cost, high-efficiency, polycrystalline thin-film solar cells. However, it is imperative to initiate stability studies on single-crystal AMOS solar cells in parallel with the development of thin-film AMOS solar cells. This is because, with thin-film solar cells, various processes (passivation of the low-cost substrate, recrystallization of the germanium thin-film, deposition of the gallium arsenide active layer, etc.) will influence the type of impurities, impurity distribution and density, crystalline grain sizes and orientations, defect densities and distributions, etc. -- any of which may influence the stability of the solar cell.

Ideally, for an intrinsically stable AMOS solar-cell structure, one should choose the barrier metal and interfacial dielectric layer material to be compatible with the gallium arsenide such that inter-diffusion between constituent materials is small. One should also choose a dielectric material which is stable in the presence of both the barrier metal and gallium arsenide. In addition, it is desirable to choose a metal and a dielectric material which are resistant to mechanical and thermal stresses.

In practice, additional constraints must be imposed. For instance, a barrier metal of high work function and low reactivity should be chosen to maintain the higher barrier height as obtained with interfacial dielectric layers. These modify the surface state distribution which influences the surface Fermi level of GaAs, and thus, enhances the output voltage of the AMOS solar cell.

1. Native Oxide

A wide variety of oxidation techniques, including thermal, glow-discharge, and anodic oxidation have been investigated previously (Refs. 4 and 5). It was found that the native oxide grown at room temperature with exposure to water-vapor saturated oxygen was most effective with respect to high V_{oc} and reproducibility. With the increased attention given to deposited non-native oxides, discussed below, few oxidations by exposure to water-vapor-saturated oxygen (H_2O/O_2) at room temperature were made during most of the previous reporting period (1 March 1977 - 28 February 1978). When it became apparent that AMOS solar cells having an oxide layer formed by H_2O/O_2 exhibit better stability at elevated temperatures, as discussed later, that process was renewed. However, the previous results could not be entirely reproduced since the highest value of V_{oc} was about 700 mV instead of about 810 mV as obtained previously (see Ref. 3). In the previous reporting period, two changes were made in the experimental set-up for H_2O/O_2 oxidation: (1) bottled gaseous O_2 was used for the O_2 source instead of oxygen boiled from liquid O_2 , (2) changes were made in the sample temperature control to eliminate moisture condensation. Previously, such condensation was often found on the sample due to fluctuations in the laboratory temperature when the air conditioning was cycled over evenings or

weekends. After converting to the earlier experimental set-up, with the exception of using the bottled gaseous O₂ source, the high V_{oc} values of 800 mV and above were reproduced. This indicated that the O₂ source was not the cause of the problem and that a super-saturated oxygen environment is required for the best native-oxide formation.

2. Deposited Oxide

Deposited oxides for AMOS solar cells are attractive for the following reasons: (1) short interfacial-layer formation time (it takes more than 48 hours at 23 C for the H₂O/O₂ oxidation of GaAs as compared with only a few minutes for 38 Å Sb₂O₃ deposition); (2) compatibility with other evaporation steps such as Schottky-barrier-metal and conducting-grid-pattern deposition; (3) potential for better stability, because unlike the native oxide which is restricted to oxides of the constituent atoms of GaAs, the deposited dielectric offers a much wider range of possible materials which may meet the stability criterion stated earlier; and (4) potential for further improvement in cell efficiency. Compounds such as oxides, nitrides, carbides, borides and silicides are all possible choices.

During an earlier investigation of alternate oxides, such as MoO₃, WO₃ and Y₂O₃, evaporated from a resistance-heated boat, it quickly became apparent that stoichiometry control was impossible, leading to highly variable results. The reasons for this are: (1) the source material undergoes changes in composition by repeated heatings in vacuum, (2) oxide reduction occurs from contact with the hot refractory boat metal, and (3) the partial pressure of background oxygen differs from run to run.

In order to minimize the stoichiometry problem, a Model 500 CO₂ laser was leased from Apollo Lasers, Inc. A photograph of the laser deposition system is shown in Figure 2-1. In this system, the horizontal laser beam is deflected by a gold-coated flat mirror through a germanium focusing lens. The focused beam passes through a NaCl window onto the dielectric evaporant located inside an ion-pumped vacuum system with cryo-sorption roughing pumps. A Kronos Model ADS-200 digital thickness monitor (TM) system was used for monitoring the thickness of the deposited oxides with the crystal oscillator located close to the sample substrate. The initial intent was to operate the CO₂ laser in the pulsed mode, such that the stoichiometry of the oxide can be preserved by flash deposition. The CO₂ laser was operated in the TEM₀₀ mode with a Gaussian beam diameter of 6 mm ($1/e^2$ point) focused by a germanium lens having a focal length of 250 mm. Hence, the effective f-number of the optical system was 42, and the minimum spot size of the focused laser beam was 0.54 mm. A maximum power density of $\sim 100 \text{ kW/cm}^2$ can be obtained when the laser is operated in the pulsed mode with a pulse duration of 250 μs .

Unfortunately, when the focused CO₂ laser beam was operated in the pulsed mode, it tended to create a hole in the dielectric source material which changed the deposition pattern. In addition, excessive spitting at the surface further complicated the deposition pattern of the evaporant. As a result, although the thickness monitor was placed very close to the sample substrate, there was no correlation of the actual thickness of the oxide layer on the sample substrate (measured by ellipsometry and correlated with photovoltaic measurements) with the mass thickness as indicated by the quartz-crystal monitor. For this

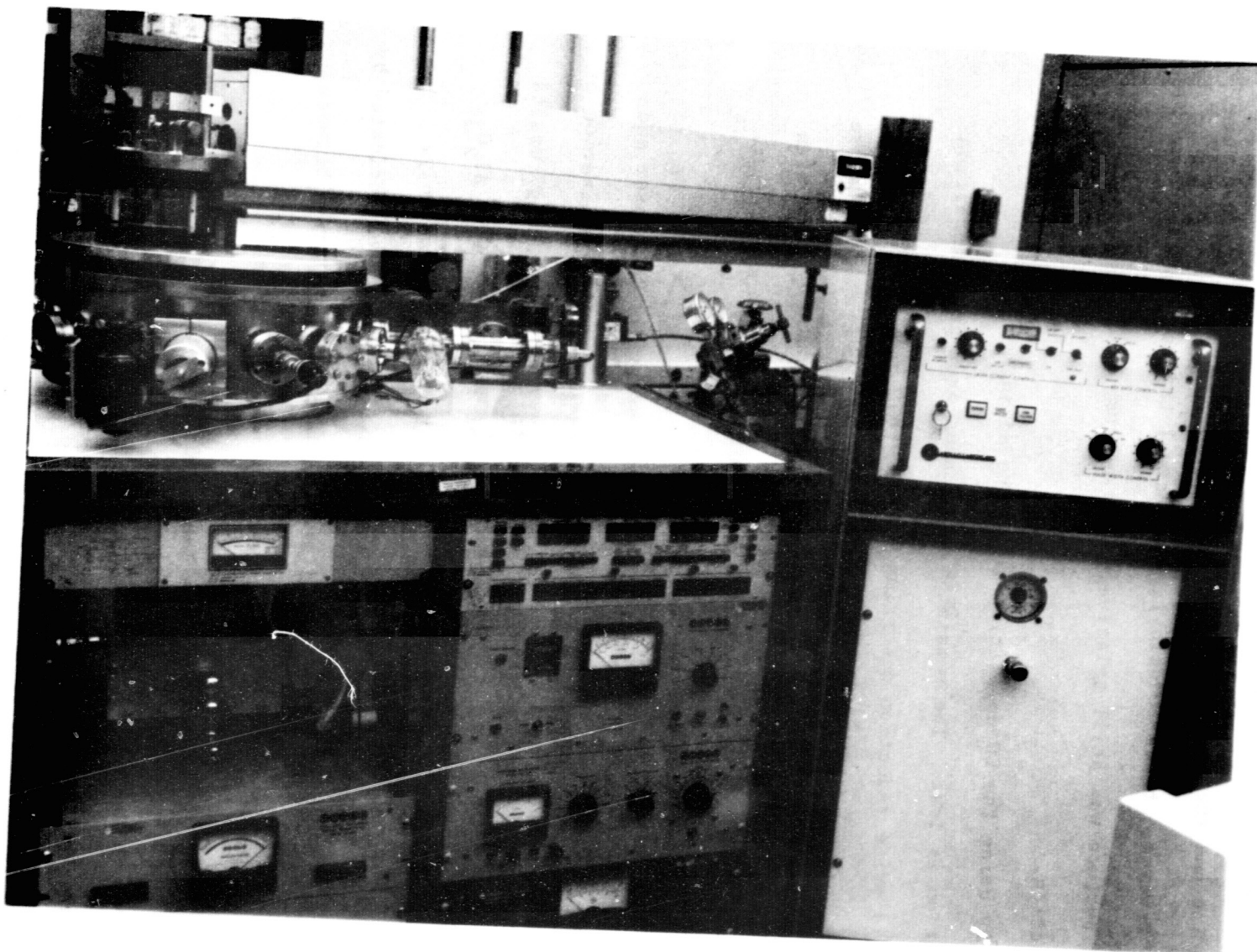


Figure 2-1. Photograph of Laser Deposition System

reason, the deposition of oxides using the pulsed laser mode was discontinued and most oxide depositions were done using the continuous wave (CW) mode. In this deposition mode, the correlation between the TM reading and the actual oxide thickness on the sample improved somewhat. However, the reproducibility in actual thickness obtained on the sample surface was still relatively poor as compared to ordinary boat evaporation.

By using the CW deposition mode, the advantage of flash deposition is lost. The remaining advantages over boat deposition are: (1) oxide reduction occurring from contact with hot refractory metal is eliminated, (2) a much higher evaporant source temperature can be achieved; hence, more stable dielectric materials with high free energy of formation (typically with high melting and boiling temperatures) can be evaporated.*

Due to the limited time involved in leasing the CO₂ laser and the problems encountered in thickness control, no true optimization of oxide thickness was feasible. Nevertheless, some interesting results were obtained. Summary photovoltaic data of laser-deposited Al₂O₃, SiO₂, and Cr₂O₃ are given in Tables 2-1, 2-2, 2-3, respectively. In the last two columns of these tables, oxide thicknesses indicated by the TM and by ellipsometry are listed. The poor correlation between these thicknesses is clearly evident.

For Al₂O₃ AMOS cells (see Table 2-1), one interesting observation was noted. Often, a nominal 60 Å-thick Ag layer (the standard thickness used for H₂O/O₂ oxide and Sb₂O₃ AMOS solar

*Although an electron beam gun can achieve similar source temperatures, the detrimental effects of the high-energy charged particles as well as x-ray radiation limit the usefulness of the e-gun as the means for forming the interfacial dielectric layer.

Table 2-1. Summary of Laser-Deposited Al_2O_3 AMOS Cells

| Sample ID | Ag Thickness (Å) | J_o (A/cm^2) | n | V_{oc} (V) | J_{sc} (mA/cm^2) | FF | η (%) | Oxide Thickness TM (Å) | Ellipsometer (Å) |
|-----------|------------------|----------------------------------|-----|--------------|--------------------------------------|-----|------------|------------------------|------------------|
| F30S | 60 | * | * | .70 | 14.7 | .82 | 8.3 | 35 | 30 |
| F51S | 60 | * | * | .71 | 0.7 | .25 | 0.1 | 13 | 43 |
| F50S | 60 | * | * | .70 | 6.8 | .26 | 1.8 | 17 | 30 |
| F72S | 60 | * | * | .71 | 12.7 | .78 | 7.0 | 12 | -- |
| F21S** | 80 | 3.5×10^{-13} | 1.1 | .75 | 23.7 | .80 | 14.2 | 12 | 61 |
| F80S | 80 | * | * | .75 | 14.6 | .73 | 8.0 | 10 | 40 |
| F41S | 100 | * | * | .76 | 13.5 | .75 | 7.6 | 10 | 38 |
| F62C | 100 | 6.0×10^{-14} | 1.1 | .76 | 13.2 | .80 | 8.0 | 11 | 38 |
| F63S | 100 | * | * | .67 | 10.2 | .54 | 3.7 | 10 | 40 |
| F64S | 100 | 6.0×10^{-14} | 1.0 | .67 | 11.8 | .64 | 5.0 | 10 | 54 |

*Dark I-V in the semi-log plot is nonlinear--meaningful data cannot be obtained

**Antireflection (AR) coated cell. (Other cells have no AR coating)

Table 2-2. Summary of Laser-Deposited SiO_2 AMOS Cells

| Sample ID | Ag Thickness (Å) | J_o (A/cm^2) | n | V_{oc} (V) | J_{sc} (mA/cm^2) | FF | η (%) | Oxide Thickness TM (Å) | Ellipsometer (Å) |
|---------------------|------------------|----------------------------------|-----|--------------|--------------------------------------|-----|------------|------------------------|------------------|
| G85S** | 60 | 5×10^{-14} | 1.1 | .74 | 25.6 | .81 | 15.3 | 14 | 30 |
| G50S | 60 | 5×10^{-13} | 1.1 | .69 | 16.0 | .80 | 8.8 | 15 | 30 |
| G51S | 60 | 5×10^{-14} | 1 | .71 | 14.0 | .81 | 8.0 | 25 | 32 |
| G22S | 60 | -- | -- | .74 | 0.0 | -- | -- | 20 | 65 |
| F73S ^(p) | 100 | 7.5×10^{-14} | 1.1 | .75 | 11.5 | .78 | 6.7 | 15 | 67 |
| D7 | 100 | 7×10^{-15} | 1.0 | .76 | 13.6 | .81 | 8.3 | 10 | 46 |
| F44S ^(p) | 160 | 6×10^{-13} | 1.1 | .69 | 10.6 | .79 | 5.8 | 15 | 38.2 |

(p) Pulsed laser deposition

** Antireflection (AR) coated cell. (Other cells have no AR coating)

Table 2-3. Summary of Laser-Deposited Cr_2O_3 AMOS Cells

| Sample ID | Ag Thickness (Å) | J_o (A/cm^2) | n | V_{oc} (V) | J_{sc} (mA/cm^2) | FF | η (%) | Oxide Thickness TM (Å) | Ellipsometer (Å) |
|-------------------|------------------|----------------------------------|-----|--------------|--------------------------------------|-----|------------|------------------------|------------------|
| F43S | 80 | -- | -- | .67 | 15.4 | .80 | 8.2 | 15 | 44 |
| F42S | 80 | H | H | .72 | H | H | H | 12 | 48 |
| F82S | 60 | 2×10^{-13} | 1.1 | .74 | 14.9 | .77 | 8.4 | 15 | 48 |
| F83S** | 60 | 9×10^{-13} | 1.2 | .74 | 27.4 | .77 | 15.6 | 15 | 47 |
| D7 ^(p) | 60 | 3.7×10^{-6} | 2.1 | .71-.66 | H | H | H | 15 | 72 |

** Antireflection (AR) coated. (Other cells have no AR coating)

(p) Pulsed laser deposition

H Hysteresis

cells) would not form a continuous film. The discontinuous nature of the Ag film is indicated by unusually low values of short-circuit current and fill-factor (FF) in some of the 60-Å Ag/Al₂O₃ AMOS cells shown in Table 1-1. This is due to the fact that in the early stages of heterogeneous nucleation of thin metal films, subsequent film-coalescence depends on the structure and composition of the substrate surface. Al₂O₃ apparently does not favor early coalescence of Ag films, in contrast to Sb₂O₃. Interestingly, improved conductivity and transmission of Ag films have been observed elsewhere due to early film-coalescence when Sb₂O₃ film is used as a nucleation-modifying layer (Ref. 6).

After studying Tables 2-1, 2-2, and 2-3, some general observations of AMOS cells made with laser-deposited oxides can be made: (1) the best V_{oc} values of all three oxides are in the 0.74 - .76 V range, (2) the diode ideality factor, n, for all three oxides of moderate thickness is very close to unity, (3) the reverse saturation current density, J_o , is in the 10^{-13} to 10^{-14} A/cm² range, (4) the best energy conversion efficiency under AMI simulation (ELH) is in the 14-15% range for 1-cm² area, fully gridded and antireflection (AR)-coated AMOS solar cells using either type of interfacial-oxide layer. Since the oxide thickness has not been optimized in this research, it is possible that the best initial values of V_{oc} or conversion efficiency may be comparable with what can be achieved using an Sb₂O₃ or H₂O/O₂ oxide. Light I-V characteristics of 1-cm², fully gridded and AR-coated AMOS cells using laser-deposited interfacial layers are shown in Figures 2-2, 2-3, and 2-4 for Al₂O₃, SiO₂, and Cr₂O₃ oxides, respectively. In all three

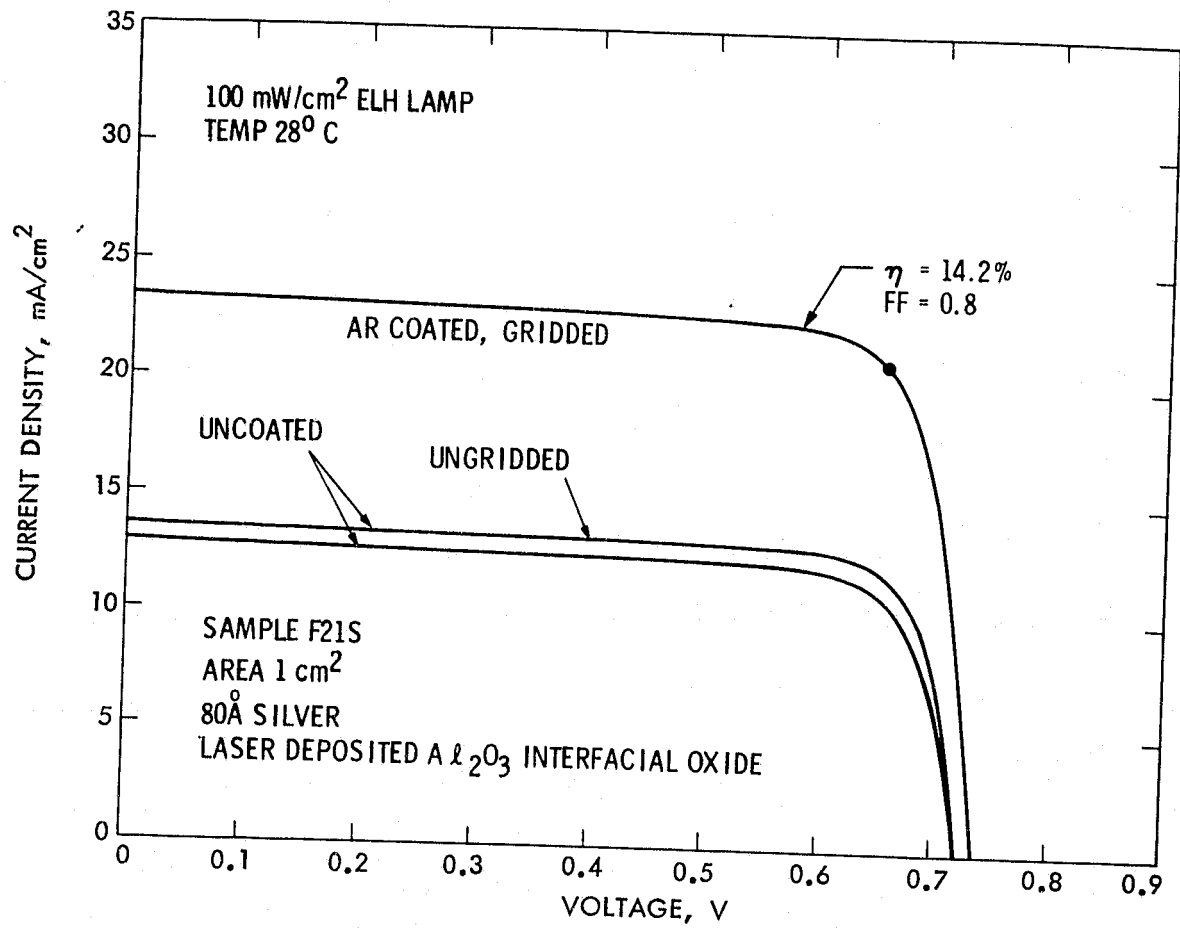


Figure 2-2. Light I-V Characteristics for an AMOS Solar Cell with Al₂O₃ Laser-Deposited Oxide

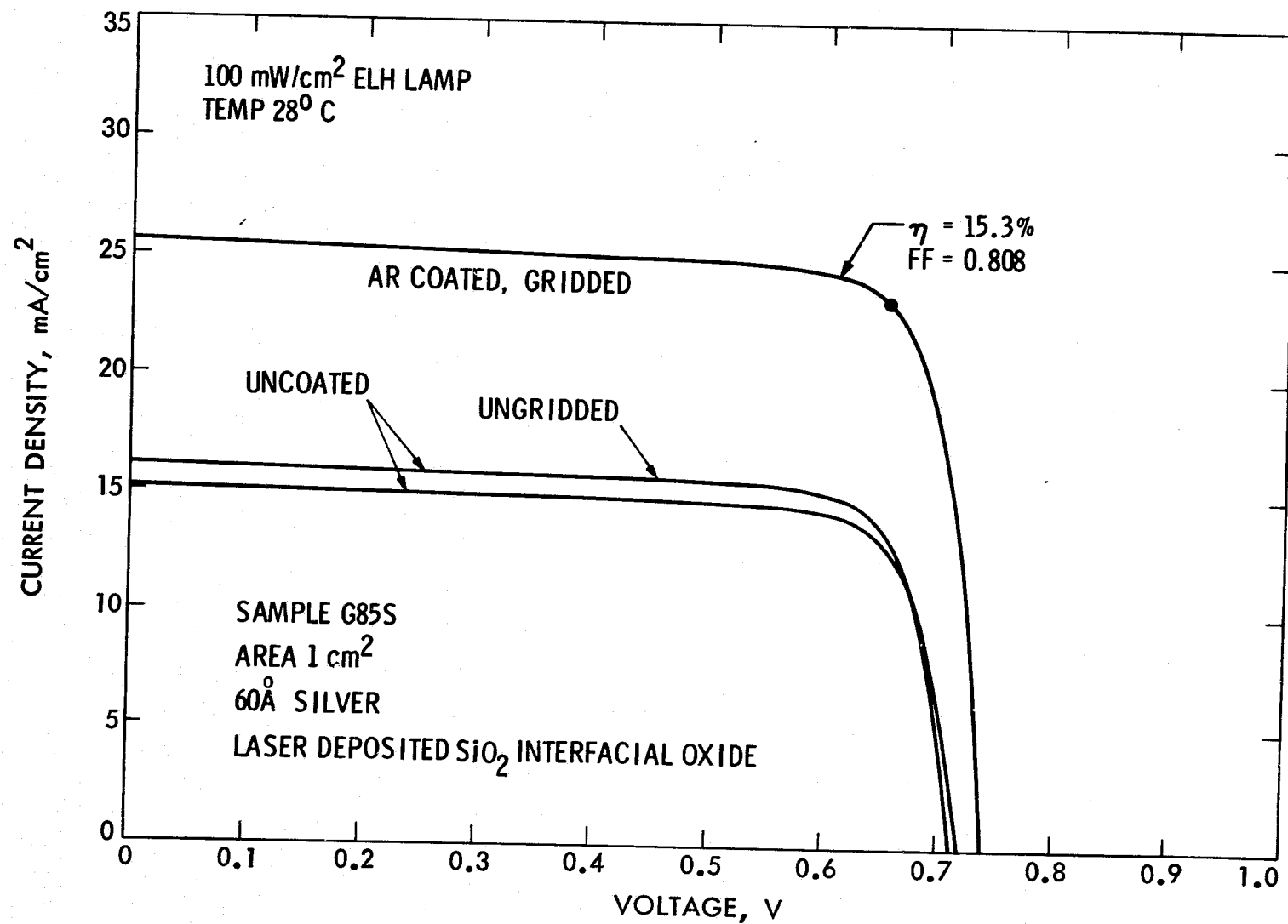


Figure 2-3. Light I-V Characteristics for an AMOS Solar Cell with SiO₂ Laser-Deposited Oxide

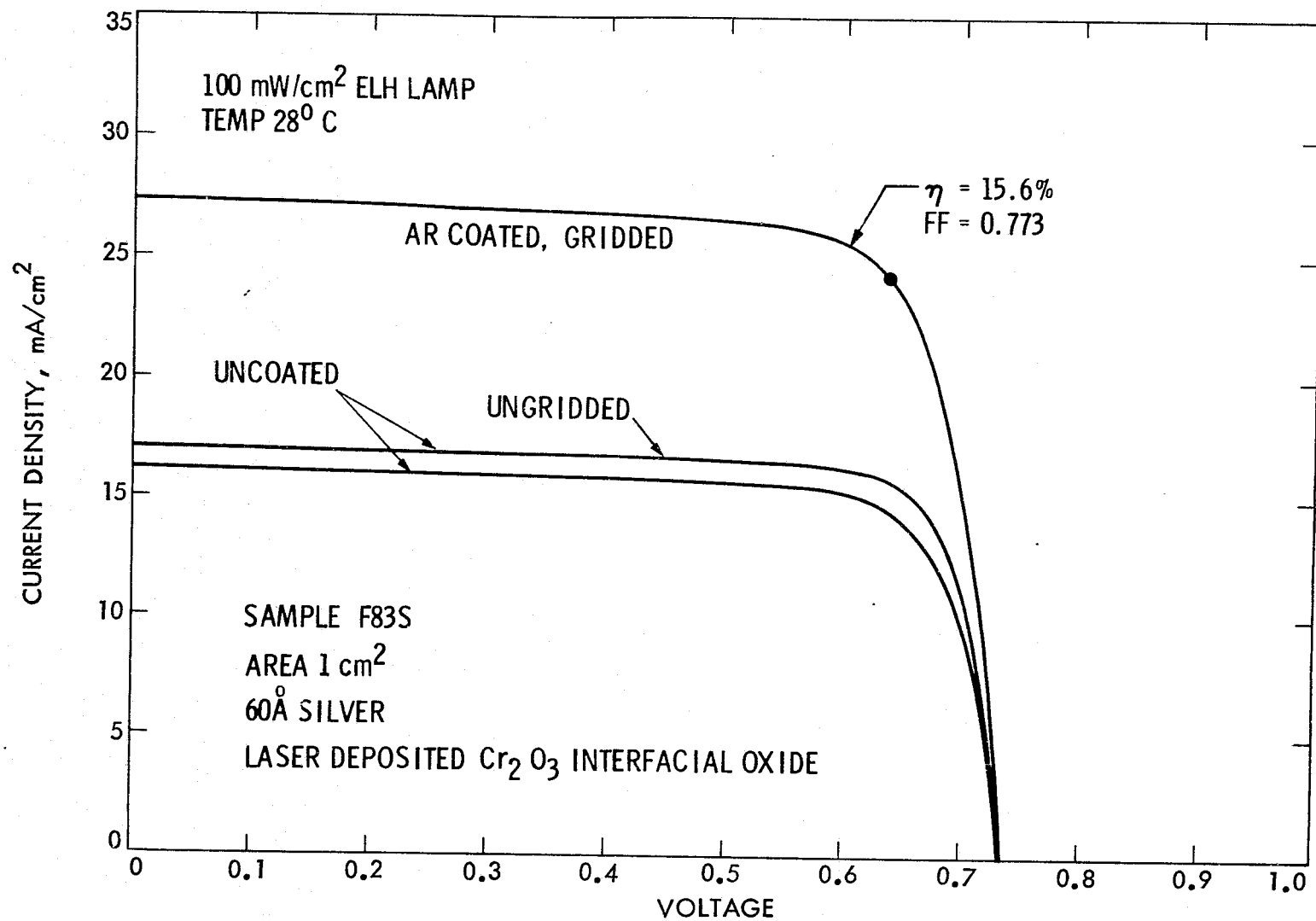


Figure 2-4. Light I-V Characteristics for an AMOS Solar Cell with Cr₂O₃ Laser-Deposited Oxide

cases, Ag was used as the Schottky barrier (SB) metal and grid structure, and Sb_2O_3 (600 Å) was used as the AR coating. A thicker Ag (80 Å) layer was needed for the Al_2O_3 AMOS cell to form a continuous SB film, in contrast to the 60 Å thickness used for a SiO_2 or Cr_2O_3 AMOS cell. As a result, a slightly lower short-circuit current, and hence, lower conversion efficiency was observed for the Al_2O_3 AMQS solar cell.

Since the interfacial layer thickness has not been optimized and only a small number of suitable cells (1-cm² fully gridded and AR-coated solar cells) were life tested, no accelerated life testing was conducted. However, room temperature "life tests" of 1-cm² AMOS cells with Al_2O_3 , SiO_2 , and Cr_2O_3 interfacial layers were performed. After exposure in laboratory air for about 6 months, AMOS cells using Al_2O_3 and Cr_2O_3 interfacial layers showed severe degradation. For the Al_2O_3 AMOS cell, more than 20% degradation in both V_{oc} and FF was observed, which, with a slight degradation in I_{sc} , resulted in more than 44% reduction in conversion efficiency. About 10% degradation was observed for the Cr_2O_3 AMOS cell in V_{oc} , I_{sc} , and FF, resulting in a 29% reduction in conversion efficiency. On the other hand, the SiO_2 AMOS solar cell showed negligible degradation in all parameters, resulting in less than 3% reduction in conversion efficiency. Consequently, future studies of alternative deposited-oxide layers will concentrate on SiO_x evaporated in a cryo-pumped vacuum system with controlled oxygen partial pressures.

B. METALLIZATION

Experiments have shown that gold-GaAs Schottky barriers cannot withstand even a moderate temperature increase above room temperature without a large decrease in the barrier height, ϕ_B , and increase in the diode ideality factor, n. Although the exact mechanism for the degradation is uncertain, it is known to be associated with a large interdiffusion of gold into the GaAs bulk, and of Ga to the surface of the gold contact (Ref. 7). More recently, Guha et al. discovered that saturating the gold film with Ga metal and flash-evaporating the alloy onto GaAs will prevent Ga out-diffusion even at temperatures as high as 400 C (Ref. 8). The values of ϕ_B and n were found to be only slightly modified after an hour at 300 C.

In order to investigate the concept of using Ga-saturated barrier metals to reduce or eliminate the out-diffusion of gallium in the AMOS system, a flash-deposition system was set up for the deposition of Ag:Ga alloys of different compositions. Since this is a proof-of-concept project, no in situ thickness monitoring system was used. A preheated, 20-mil-thick W boat (made of two W boats spot-welded together with a small hole on the top as the entrance for the gravity-fed Ag:Ga charge) was used to assure good thermal conductance and large thermal mass for true flash-deposition. The flash-deposition system was initially designed for flashing metal in thin wire form (Ref. 9). Unfortunately, after long delay and many tries, the vendor (Wilkinson Co.) was unable to deliver the Ag:Ga wire with 12% Ga content (by weight) due to excessive work hardening of the alloy. Consequently, a compromise was made to accept the Ag:GA alloy (12% Ga) in rod form (~3 mm diameter) together with an additional supply of 2% Ga:Ag alloy.

The flash-deposition system was redesigned to accept evaporation material in small lumps. The reason for choosing 12% and 2% Ga alloys was to obtain information regarding the stability of AMOS cells made with both saturated and unsaturated Ga:Ag alloys at room and at elevated temperatures.

The solid solubility of Ga in Ag is about 12% at 370 C and 8% at 200 C as indicated by the Ag-Ga phase-diagram of Hanson and Anderko (Ref. 10). Due to lack of information for lower temperatures, the solubility of Ga at 20 C can only be estimated to be more than 3% by weight using extrapolated values obtained from the Ag-Ga phase diagram.

True flash-depositions, using ~4 mg of alloy per charge, were verified by observing semitransparent films formed instantaneously on a glass substrate, when each charge was dropped into the preheated tungsten boat. (It was found that if 8-mg charges were used, flash-deposition conditions could not be achieved and the alloy would evaporate slowly in one to two seconds.) The thickness of the flash-deposited Ag alloy was determined by interferometry to be 300 \AA for two 4-mg alloy charges.

The photovoltaic results of solar cells made of flash-deposited Ag:Ga alloys can be summarized in the following manner. For Ag (12% Ga) baseline SB solar cells, a very low barrier height was indicated by the low output voltage observed (0.35 V for an equivalent I_{sc} of 25 mA/cm², the near unity diode ideality factor, n (observed in the dark I-V characteristics), and the high reverse saturation current density ($J_o = 4 \times 10^{-8} \text{ A/cm}^2$). On the other hand, the barrier height observed for Ag (2% Ga) baseline SB solar cells based on C-V, light I-V, and dark I-V measurements was very close to that obtained with pure Ag barrier metal. Subsequently, Sb_2O_3 AMOS solar cells

were made using Ag (2% Ga) and Ag (12% Ga). However, the data obtained varied widely and were not reproducible, thus preventing a conclusion from being drawn. Further experiments will be needed to clarify the situation.

C. LIFE TESTING

Long-term stability of the AMOS solar cell under normal operating conditions is as important as the solar cell's initial conversion efficiency. Since AMOS solar cells have dissimilar materials forming the charge-collecting junction, unlike that of a homojunction solar cell, special attention should be given to the possibility of interdiffusion and chemical reactions at the junction.

In order to separate the roles of the barrier metal and that of the interfacial oxide layer on the stability of the AMOS structure, accelerated life testing of both baseline (no intentional oxide) and AMOS solar cells are being performed. Life testing of solar cells was initiated in the previous reporting period at an elevated temperature (100 C) in order to provide some acceleration to the testing. Because a number of barrier metals and interfacial oxides have yet to be investigated for their potential beginning-of-life efficiency, no evaluation of activation energies or detailed studies of the chemical or diffusion dynamics, which can be made using Auger, ESCA, SIMS, etc., have been attempted on the particular systems discussed below. However, a few life tests at 205 C and at room temperature have been conducted to provide some correlation between accelerated and normal life testing.

A stable metal/GaAs system without an oxide layer is crucial to a stable AMOS solar cell because the interfacial oxide layer is too thin to prevent metallurgical interreactions between the metal and GaAs. Hence, testing in the dark of baseline SB solar cells at 100 C with the metals Ag, Cu, and Ni was initiated in the previous reporting period -- accumulating more than 10,000 hours through the current reporting period for most cells (Figure 2-5). All cells fabricated for life testing were 1-cm² in area, fully gridded and AR coated, contacted with brass foil and silver paste, covered with 6-mil cover glass, and sealed with epoxy. The barrier heights, and hence the initial efficiencies with these metals, appear to correlate weakly with the metal electronegativity. From Figure 2-5, one can see virtually no detectable changes in efficiency for baseline Ag and Ni solar cells. However, in the case of Cu, the conversion efficiency went through an initial fast degradation followed by a more gradual degradation -- suggesting that there may be two or more mechanisms involved.

Life-testing results at 100 C for Ag, Ni, and Cu AMOS solar cells using Sb₂O₃ interfacial oxide layers are shown in Figure 2-6. With the addition of an Sb₂O₃ oxide layer, the observed stability was reduced substantially. The figure does show that the choice of metal can be important for reliability as well as for efficiency. Figure 2-7 shows that for a given metal, Ag in this case, there also were differences in degradation between the various oxides. The degradation of V_{oc} for baseline cells and AMOS cells using vacuum-deposited Sb₂O₃ and MoO₃ oxides and the native oxide grown by H₂O/O₂ at room temperature is clearly illustrated in this figure. In general, the primary degradation at 100 C is a reduction in open-

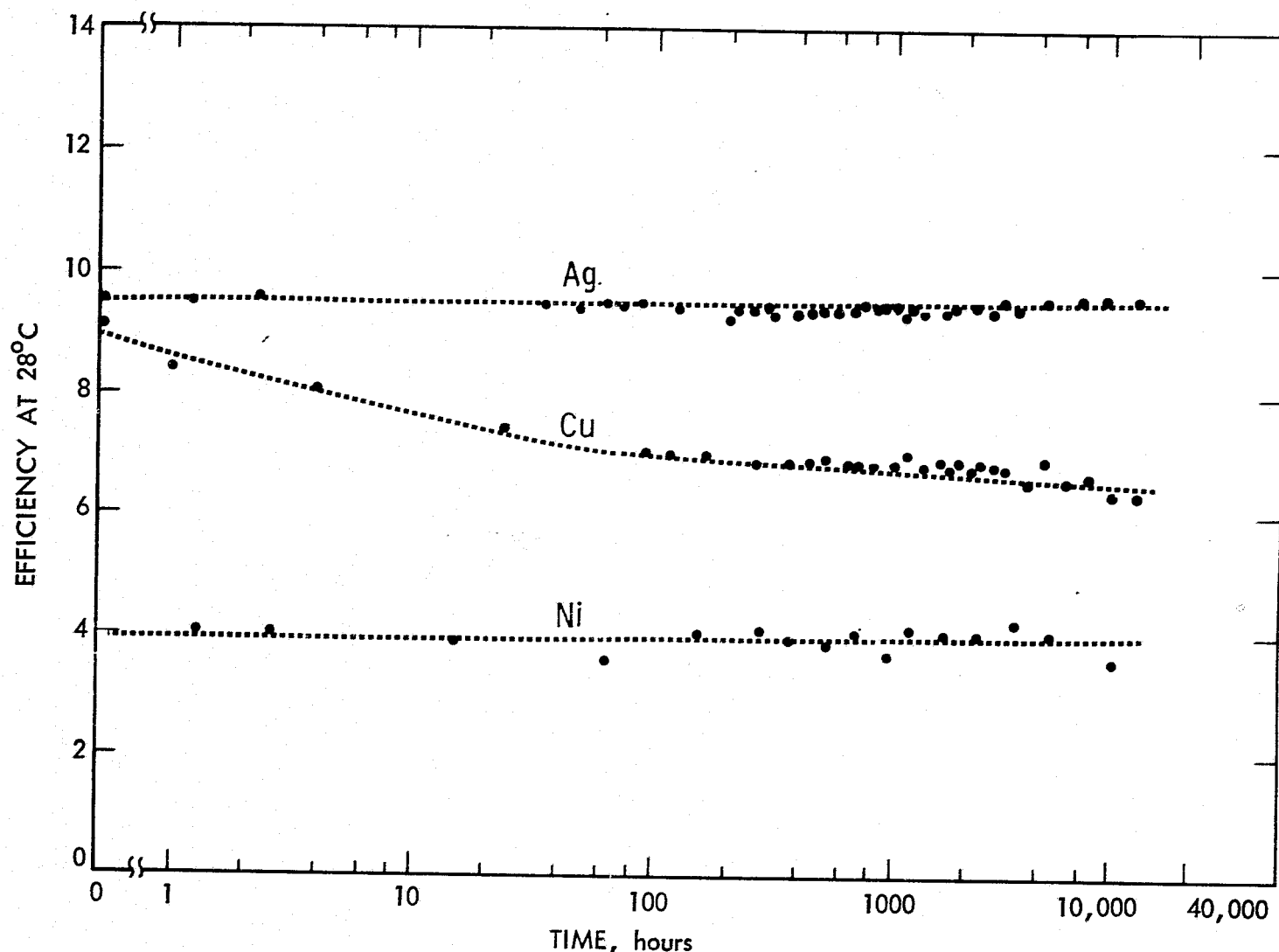


Figure 2-5. Results of 100 C Exposure in the Dark of Three AMOS Solar Cells Without Intentional Oxide Layer

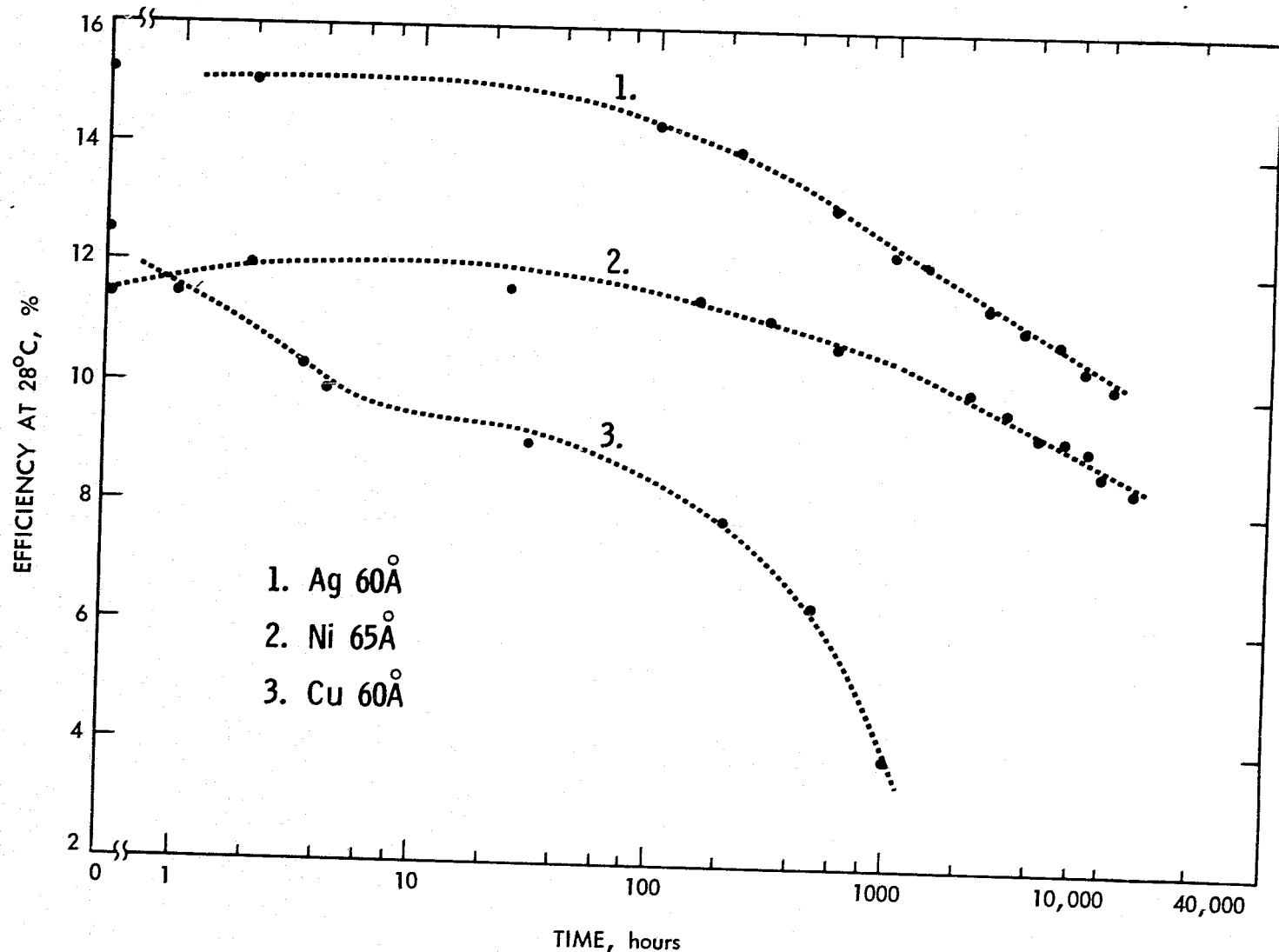


Figure 2-6. Results of 100 C Exposure in the Dark of Three AMOS Solar Cells Fabricated with $38\text{-}\text{\AA}$ Deposited Sb_2O_3

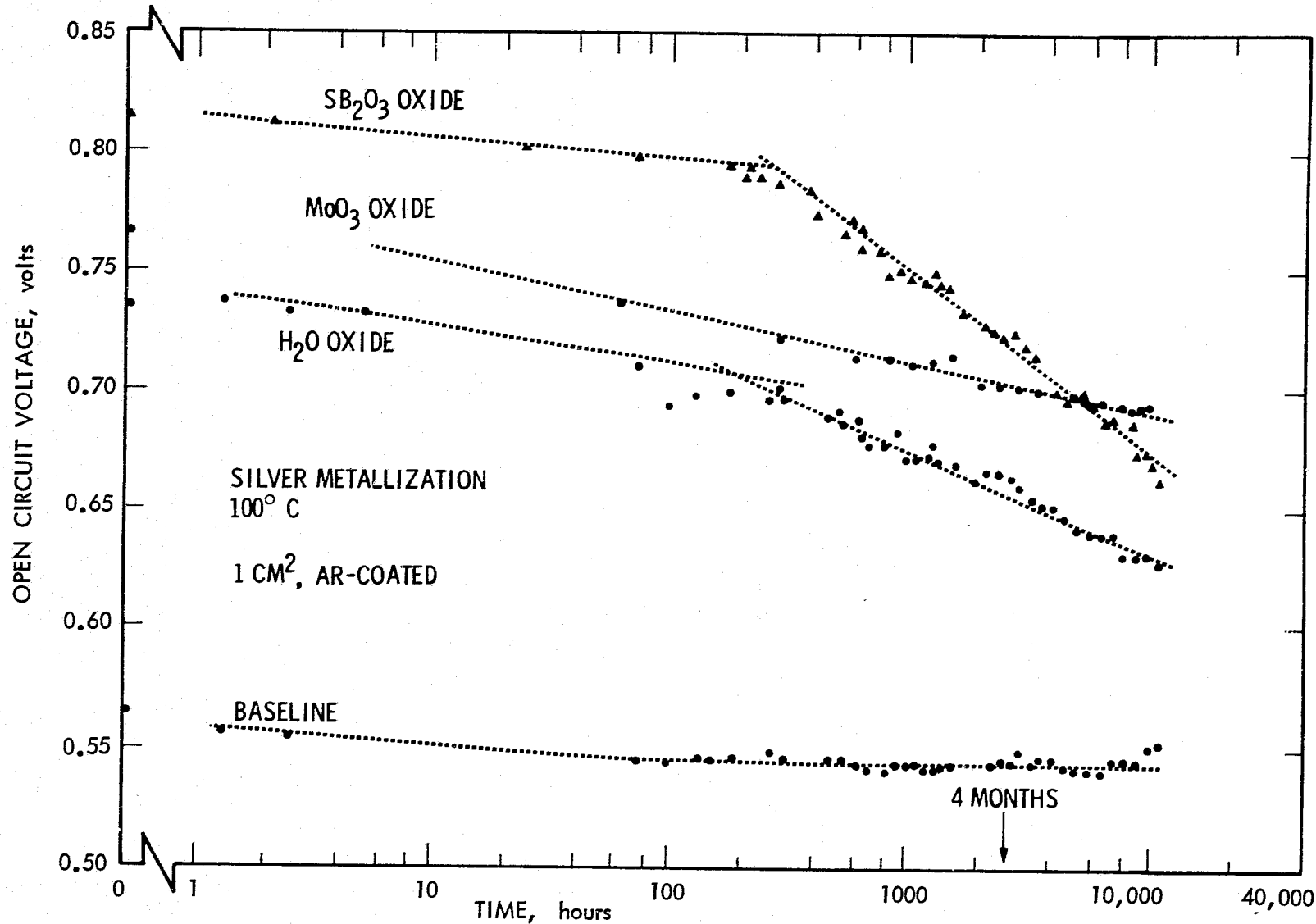


Figure 2-7. Stability of V_{oc} with 100 C Exposure in the Dark for Several Types of AMOS Solar Cells

circuit voltage and fill factor. The native H_2O/O_2 AMOS cell shows a slower degradation rate in contrast to the Sb_2O_3 AMOS cell. The MoO_3 AMOS cell showed an even lower degradation rate in V_{oc} relative to H_2O/O_2 or Sb_2O_3 AMOS cells. It should be pointed out that these results are based on a sampling of one for each type. Also, since the deposited oxides were evaporated from a resistance-heated boat, stoichiometry control was difficult. Means to flash deposit or reactively evaporate oxides in a controlled oxygen environment are being pursued, as discussed above.

Figure 2-8 shows the change in fill factors for the same baseline, Sb_2O_3 AMOS, and H_2O/O_2 AMOS solar cells referred to in Figure 2-7. The dramatic reduction in FF for the Sb_2O_3 AMOS cell occurred after a slight initial degradation. The rapid reduction in FF continued at approximately the same rate, reaching a fill-factor value of about 60% after 10,000 hours. Simultaneously, the reverse saturation current for Sb_2O_3 AMOS cells had increased more than 5 orders of magnitude (Figure 2-9), while the ideality factor had increased from 1.2 to 2.8 (Figure 2-10), after 10,000 hours. The reason for the observed degradation with time at 100 C may be related to the formation of new interface states within the forbidden band gap farther removed in energy from the valence band edge. These states could cause a decrease in barrier height, resulting in the observed V_{oc} and FF degradation for the AMOS cells investigated to date. In addition, particularly for the Sb_2O_3 cells, new interface states were apparently being introduced which acted as recombination centers with a large capture cross-section for majority carriers (electrons), resulting in very large values of J_o .

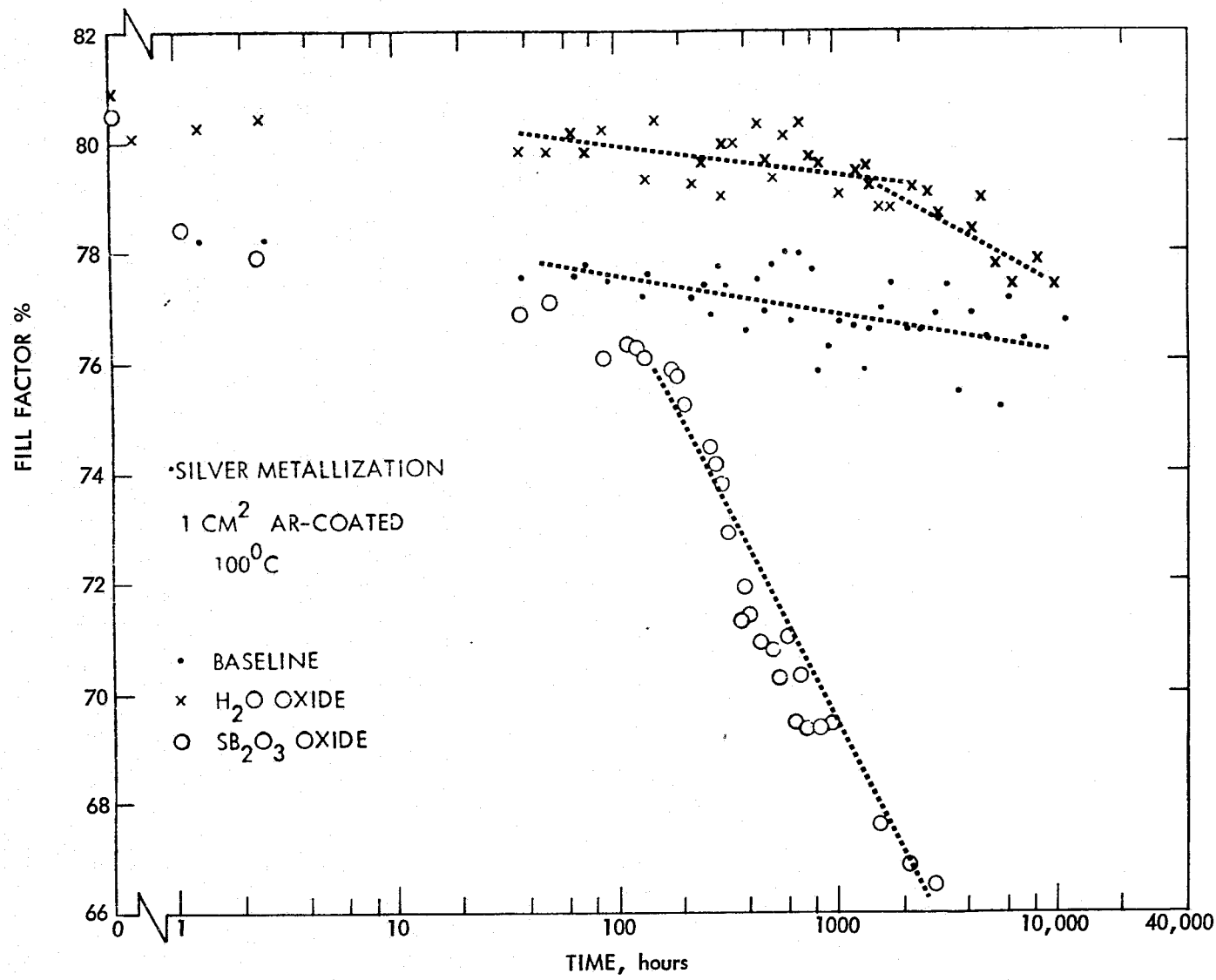


Figure 2-8. Stability of Fill Factor with 100 C Exposure in the Dark

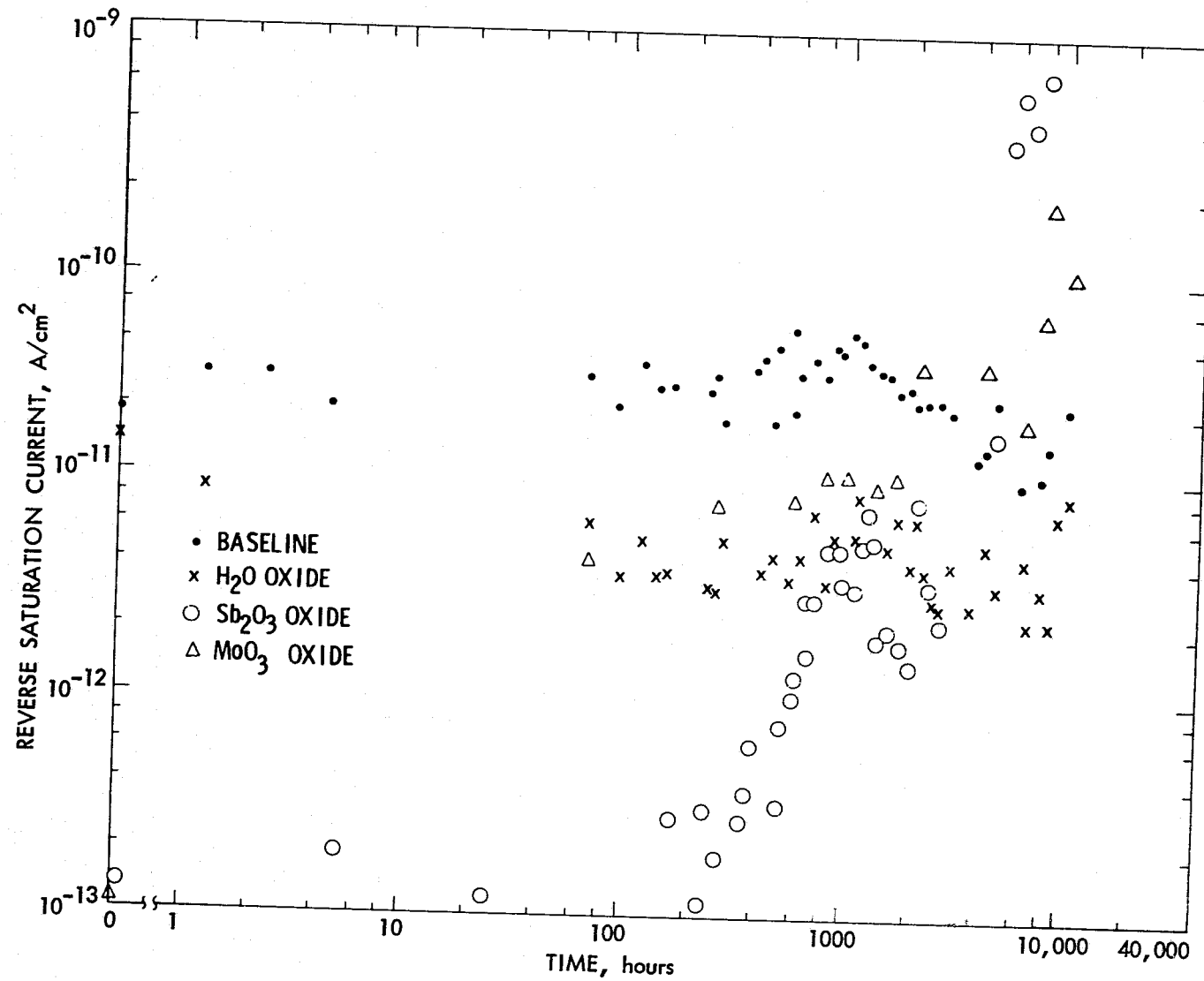


Figure 2-9. Results of 100 C Exposure in the Dark
on Reverse Saturation Current Density

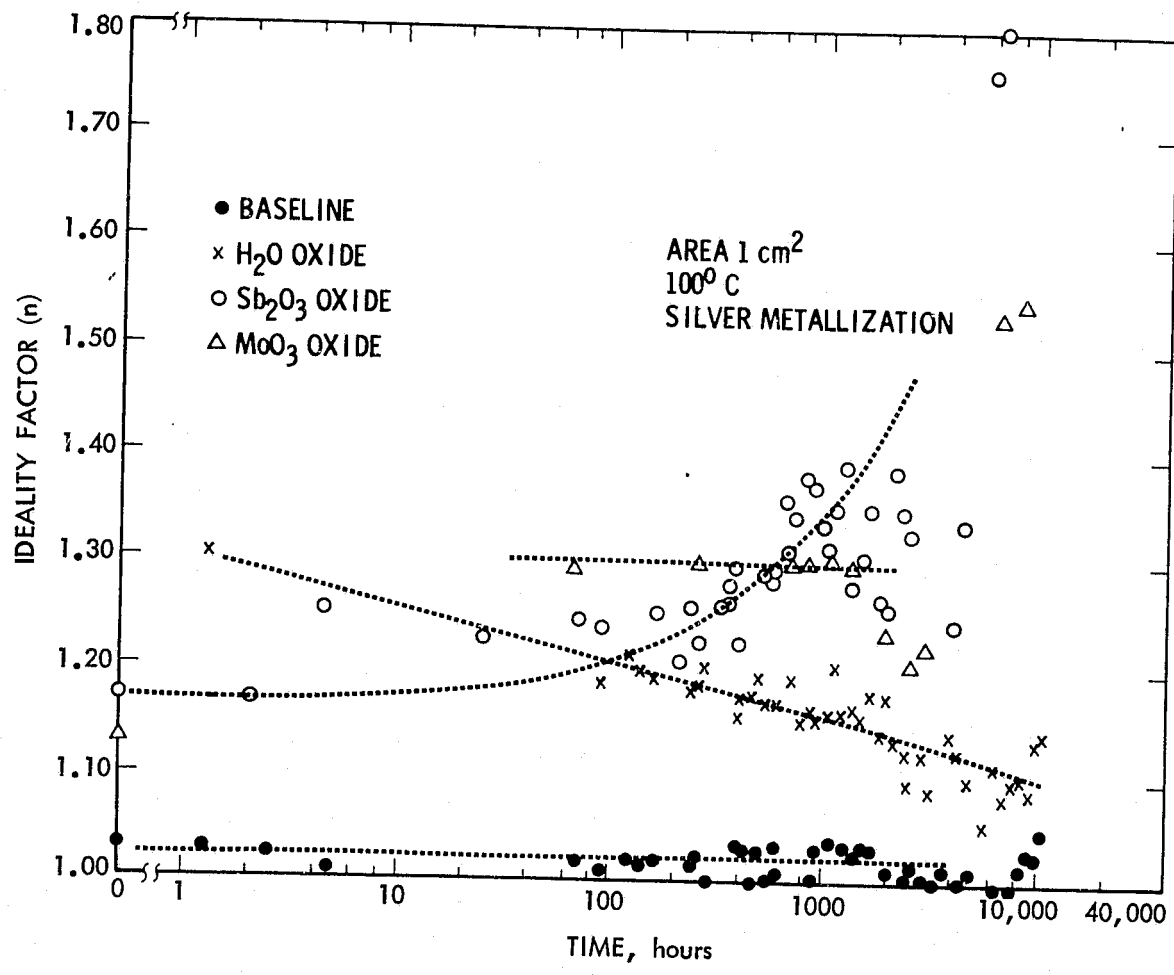


Figure 2-10. Results of 100°C Exposure in the Dark on the Diode Ideality Factor

Accelerated life testing needs to be conducted more rapidly in order to characterize a larger number of structures in the available time. Hence, a low-mass oven system was built having a thermal time constant less than 5 minutes and the capability of being continuously purged with nitrogen gas. Life testing at 205 C for a 1-cm², fully gridded, and AR-coated H₂O/O₂ oxide AMOS solar cell was conducted to establish a base for future comparisons. The result of such a life test is shown in Table 2-4. Note that for 205 C, the degradation rate is largest for V_{oc} with lower rates for the FF and the I_{sc} -- similar to 100 C testing. The percentage degradation in the H₂O/O₂ AMOS cells in 2 hours and 4 hours at 205 C is almost the same as that in about 1000 hours and 10,000 hours at 100 C , respectively.

Table 2-4. Life Test of H₂O/O₂ Oxide AMOS Cell
in N₂ at 205 C in the Dark

| Time (hr) | V _{oc} (V) | J _{sc} (mA/cm ²) | FF | (%) |
|--------------|------------------------|--|-------|------|
| 0 | 0.75 | 25.2 | 0.759 | 14.4 |
| 2 | 0.68 | 25.0 | 0.754 | 12.8 |
| 4 | 0.63 | 24.5 | 0.739 | 11.4 |
| 25 | 0.55 | 23.6 | 0.675 | 8.7 |
| 47 | 0.53 | 23.0 | 0.664 | 8.1 |
| 180 | 0.50 | 22.5 | 0.587 | 6.7 |

In order to correlate the accelerated life test at 100 C to the operating life at room temperature, an Sb_2O_3 oxide AMOS solar cell was tested at room temperature under the same encapsulation condition and laboratory-air exposure. After 7300 hours, the energy conversion efficiency of the Sb_2O_3 AMOS cell dropped from an original value of 16.9% to 16.4% (97% of the original conversion efficiency). This is equivalent to the percentage degradation of a Sb_2O_3 AMOS cell exposed at 100 C for 10 hours. By defining the operating life of the solar cell as the time during which the solar cell degrades to 90% of the initial conversion efficiency, then the operating life of the Sb_2O_3 AMOS cell is about 250 hours at 100 C. For the same degradation, doubling the time of testing at 205 C is equivalent to 10 times the time of testing at 100 C, as a conservative estimate. The corresponding operating life at room temperature should be similarly proportional to that at 100 C. Thus, the operating life at room temperature may be estimated to be at least $7300 \text{ hours} \times (250 \text{ hr}/10 \text{ hr}) = 182,500 \text{ hours}$, or about 20 years. Since the H_2O/O_2 and MoO_3 AMOS cells were more stable than the Sb_2O_3 AMOS cell in the 100 C life test, one may conclude that H_2O/O_2 and MoO_3 AMOS cells are more stable at room temperature.

However, it should be pointed out that all life tests were done under dark or ambient light conditions. The lifetime of solar cells under AML condition and loaded to deliver maximum power may give quite different results. Further life testing of AMOS solar cells under simulated AML condition will be conducted.

SECTION III
THIN-FILM POLYCRYSTALLINE GaAs

A. GERMANIUM RECRYSTALLIZATION

1. Recrystallization

The ultimate goal of this research task is to extend the previously discussed single-crystal processing for AMOS solar cells to the low-cost GaAs thin-film structures, shown in Figure 1-1, as well as to investigate the feasibility of grown p/n structures.

The use of a recrystallized germanium (Ge) layer between the GaAs film and the low-cost substrate is a key element in this thin-film approach. Although there could be 25% added cost by using a Ge interlayer, the potentially higher efficiency achievable with the large grain sizes should lead to a lower cost per watt, especially if p/n junctions were utilized. The Ge layer also provides: (1) a low-resistance ohmic back contact, (2) a buffer layer against diffusion of deep-level impurities from the substrate, and (3) a stress-relief layer reducing the built-in stress between the GaAs and the substrate due to differences in thermal expansion.

Initial recrystallization experiments involved the use of line-focused heat lamps, giving uneven surfaces due to the large area of melting. Subsequent experiments used a CW Nd/YAG laser beam as described previously (see Refs. 1 and 2). When the laser operating with multi-mode power of 40 W CW was focused to a line having a width of 7 mils at the half-power point, very smooth surfaces with grain sizes of millimeter dimensions were obtained. However, in the

line-focusing mode, the power density is inherently non-uniform laterally -- high at the center and low at the ends. This resulted in non-uniform melting of the Ge throughout the thickness of the film across the substrate. Consequently, the laser beam was focused to an approximately 1-mm diameter spot and slowly scanned at a frequency less than 1 Hz perpendicular to the substrate pull direction, with a pull speed of about 10 mm/min. Due to low laser power (40 W), large spot size (\sim 1 mm), and low background-heating temperature, no apparent crystal growth could be observed when the frequency was increased beyond 1 Hz, scanning the full width of the substrate (22 mm). During this reporting period, a modification was made to increase the background heat by introducing light-directing mirrors between the background heating lamp and the substrate susceptor. A larger diameter Nd/YAG laser rod was installed to increase the maximum multi-mode CW power from 40 W to more than 80 W. In addition, the laser optics were modified to yield a smaller spot size of 0.5 mm. As a result of these modifications, grain growth was observed at a scanning frequency higher than 1 Hz, and a systematic study of the influence of grain size versus different recrystallization parameters was then performed.

At the maximum background temperature (565 C) and maximum usable laser power (80 W), a scanning frequency at or lower than 8 Hz was needed to achieve visible grain growth when a 22 mm scanning amplitude was used. The inability to achieve grain growth at a scanning frequency higher than 8 Hz can be attributed to excessive heat loss, leading to incomplete melting in the bulk germanium.

It was found that the pulling speed is not a sensitive parameter for obtaining good grain growth. The largest grain size and smoothest surface was achieved with a pulling speed from 10 to 40 mm/min at a background temperature of 565 C, laser power of 80 W, and a scanning frequency of 2 to 8 Hz.

Relatively high laser power was required to produce a recrystallized germanium film with large crystallite sizes on conducting metal substrates. At 565 C background temperature, 4 Hz scan frequency, 22 mm scan amplitude, and 20 mm/min substrate pull speed, reasonably large grains could be obtained only for laser powers higher than 60 W.

With the other parameters fixed, the largest grain sizes were obtained at the highest background temperature (565 C). However, at the highest laser power (80 W), the best surface (large grain size with smooth surfaces) is achieved at a background temperature of 495 to 530 C. The influence of background heating on the grain size can best be illustrated by Figure 3-1. In this case, the recrystallization was done on a 10- μ m thick Ge film vacuum-deposited on 10-mm thick tungsten, using 80 W laser power, 20 mm/min pull speed, 22 mm scan amplitude and 4 Hz scan frequency. The background temperatures were 565 C, 530 C, 495 C, 465 C, 420 C, 375 C, and 320 C for the seven bands from left to right in the figure. The top half of the sample was etched to reveal the grain structure more clearly. The narrow matte-surface regions between the bands are regions not subjected to laser heating.

Besides large crystallite sizes, surface smoothness is also important for polycrystalline thin-film solar cells, particularly for Schottky barrier solar cells. Excessive surface roughness will cause high sheet resistance or even a discontinuous barrier-metal film with

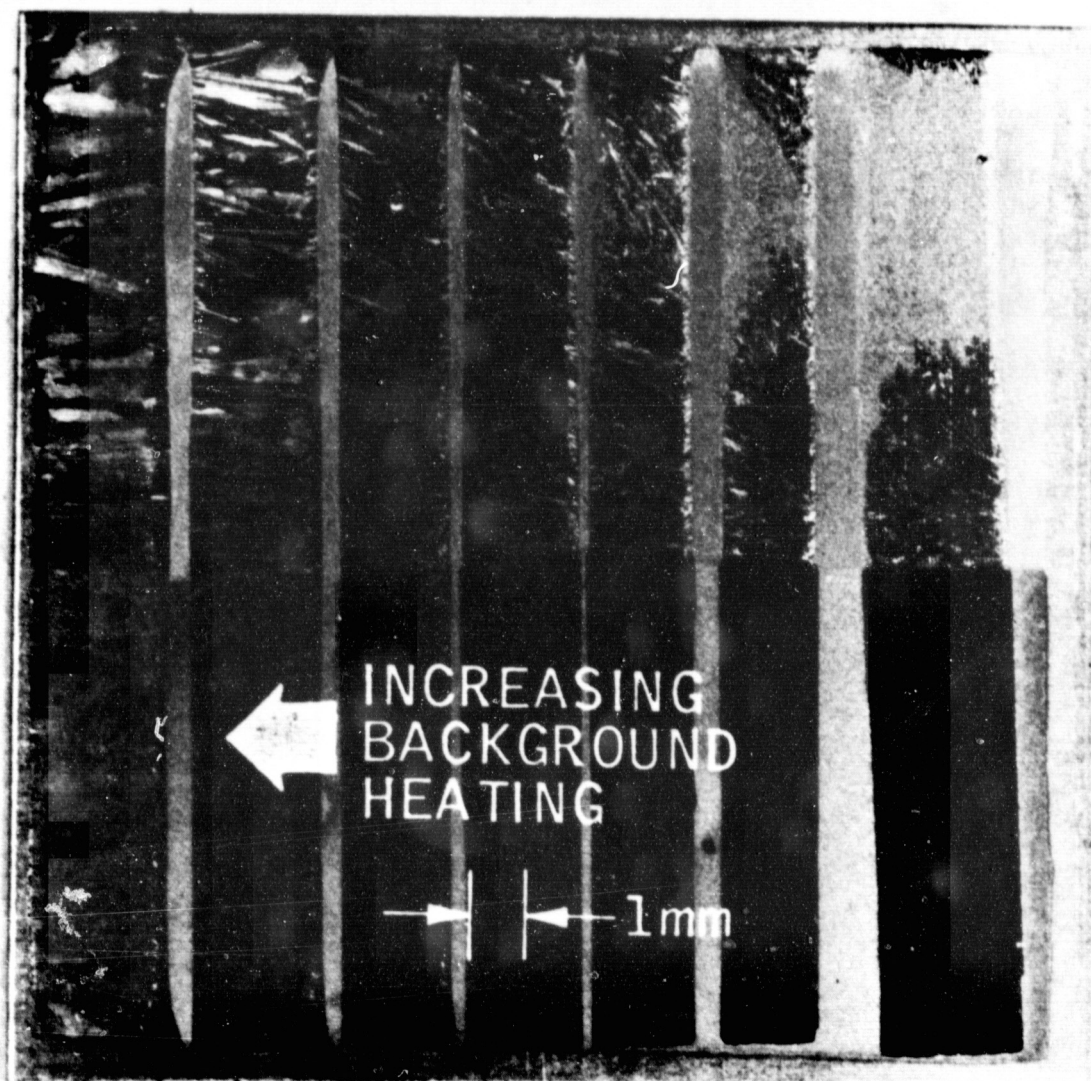


Figure 3-1. Influence of Background Heating
on Grain Size of Recrystallized Ge

the SB solar cell. Hence, experiments were performed to see if smoother surfaces could be achieved by reducing the pulling speed of the substrate which resulted in overlapping molten zones.

Unfortunately, the results were unsatisfactory.

Subsequently, experiments were conducted with fixed recrystallization parameters with the substrates undergoing a second pass with the laser. The results showed that the second pass improved the surface morphology. However, additional passes did not further improve the smoothness. To illustrate the effect of multiple passes, a low-magnification SEM photograph of a single-pass recrystallized Ge film (background temperature of 530 C, laser power of 80 W, scan amplitude of 22 mm, scan frequency of 2 Hz and substrate pull speed of 10 mm/min) is shown in Figure 3-2. For comparison, a similar photograph of a triple-pass recrystallized Ge film using the same parameters is shown in Figure 3-3. It is evident that the latter Ge surface is indeed much smoother than that of the former.

Figures 3-4 and 3-5 are high-magnification photographs of the same samples that had undergone single and triple passes, respectively. The sample surfaces were etched in a solution of $\text{HF:H}_2\text{O}_2:\text{H}_2\text{O}=1:1:4$ for 30 seconds. One can see that there are fewer defects in the triple-pass recrystallized germanium film in contrast to the single-pass sample. The small, white lumps seen in both SEM photos were identified by EDAX (Energy Dispersive Analysis of X-rays) as W and Ge alloys or compounds. The large, asymmetrical lumps seen in Figure 3-5 were identified as a mixture of Sb, Cu, Fe, and Ge. The presence of Cu/Fe was due to contamination from the e-gun system during vacuum deposition of Sb-doped Ge. To avoid the contamination

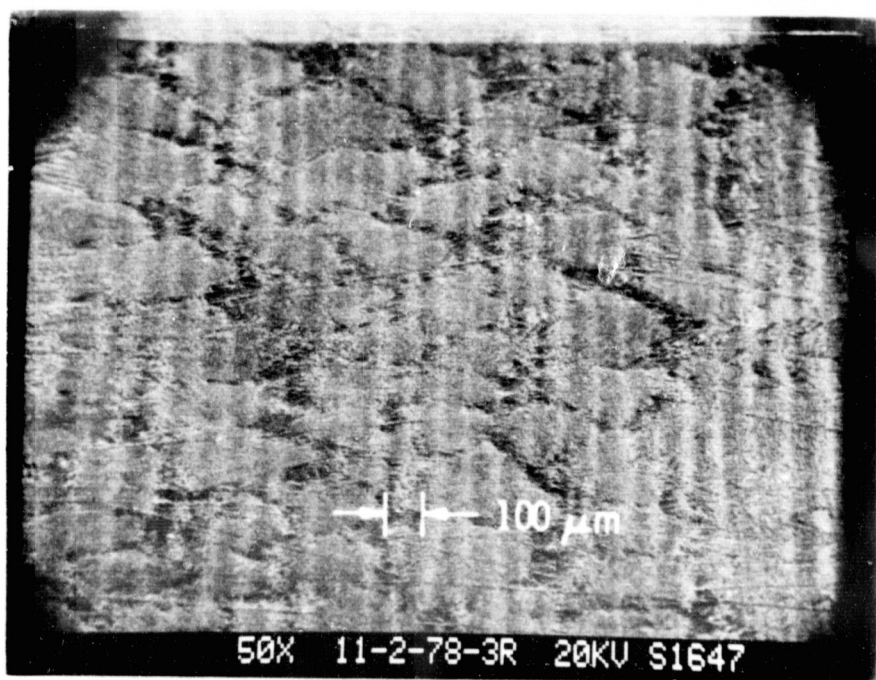


Figure 3-2. Low-Magnification SEM Photo of Recrystallized Ge Film with Single Laser Pass

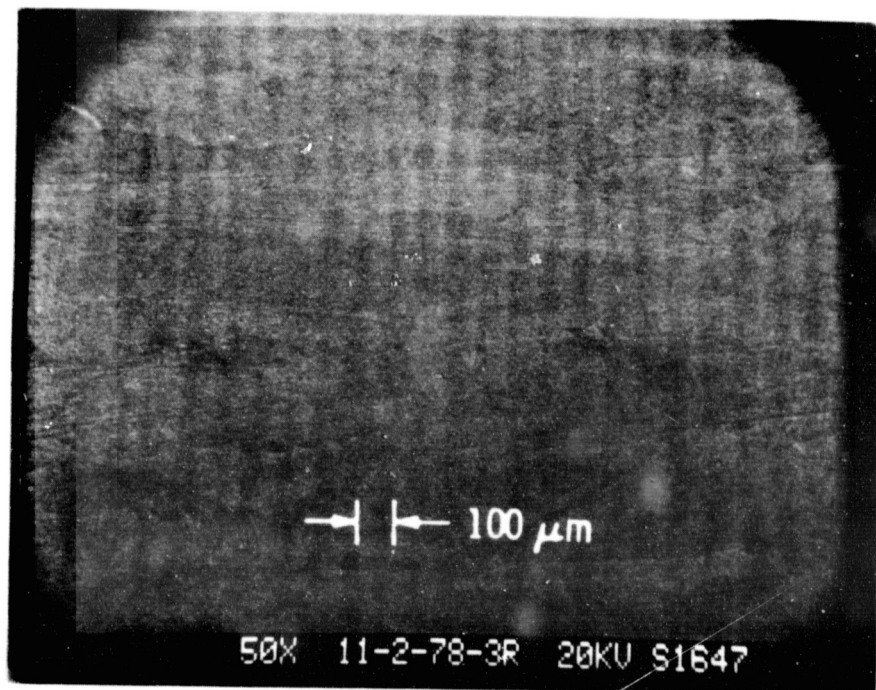


Figure 3-3. Low-Magnification SEM Photo of Recrystallized Ge Film with Three Laser Passes

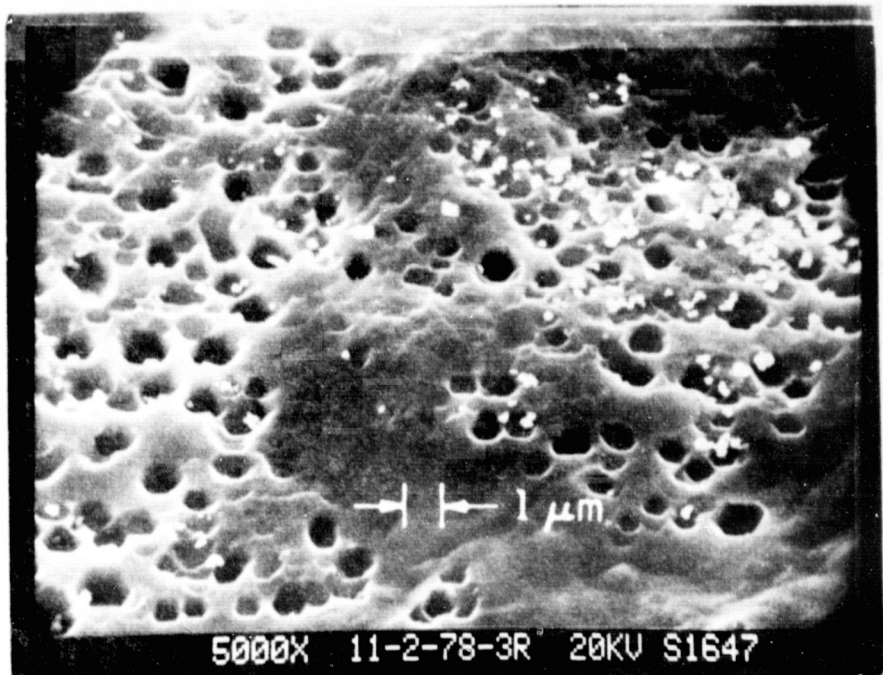


Figure 3-4. High-Magnification SEM Photo of Recrystallized GE Film with Single Laser Pass

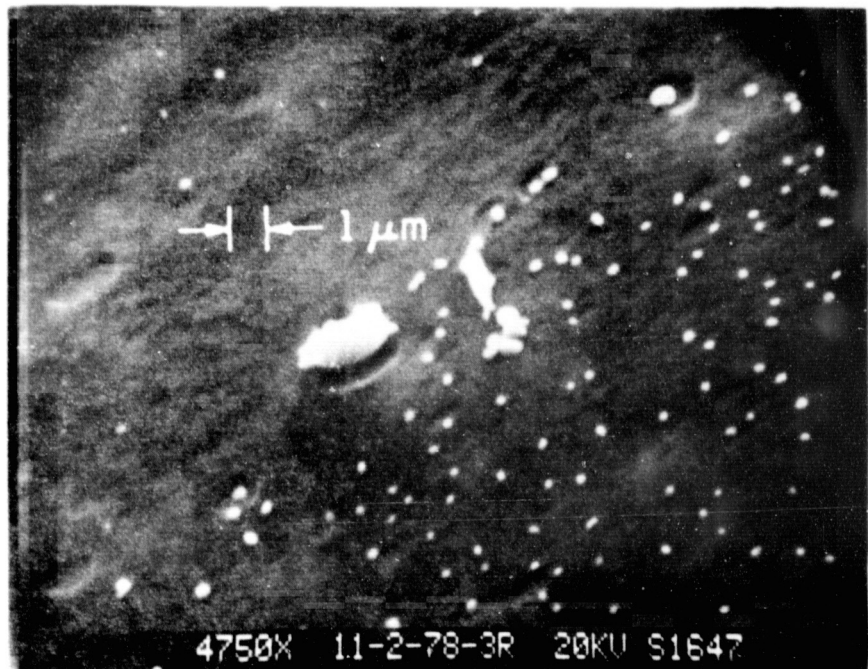


Figure 3-5. High-Magnification SEM Photo of Recrystallized GE Film with Three Laser Passes

problem, pure W liners were subsequently used in the e-gun hearth. Unfortunately, the W liners have a very limited life due to thermal stresses. Molybdenum crucible inserts were also tested; however, excessive Mo incorporated in the Ge was co-evaporated, affecting the recrystallization process. Hence, this approach was abandoned. Subsequently, CVD films of Ge deposited at Rockwell on unetched substrates of W showed good results when recrystallized, with no evidence of Cu/Fe contamination. Therefore, the growth of contamination-free Ge films by CVD methods at JPL is planned.

A brief feasibility study of recrystallized Ge films on W substrates using pulsed electron-beams was conducted in cooperation with the SPIRE Corp. The e-beam gun, operated with 80 to 100-ns pulses, a peak voltage of 12 kV, and a peak current of 500 A/cm^2 , was used to melt the Ge layer, or at least the near-surface region. Upon subsequent solidification, the Ge/W substrate was examined with the SEM. A photograph of the sample, with half portion etched to reveal the grain structure, is shown in Figure 3-6. The left portion of the photograph (unetched surface) shows a fairly smooth and featureless surface topology, while the right portion (etched surface) shows approximately symmetrical small grains with an average grain size of $\sim 10 \mu\text{m}$. Thus, it would appear that zonal melting is required in order to obtain large (\sim millimeter size) grain development in recrystallized Ge films.

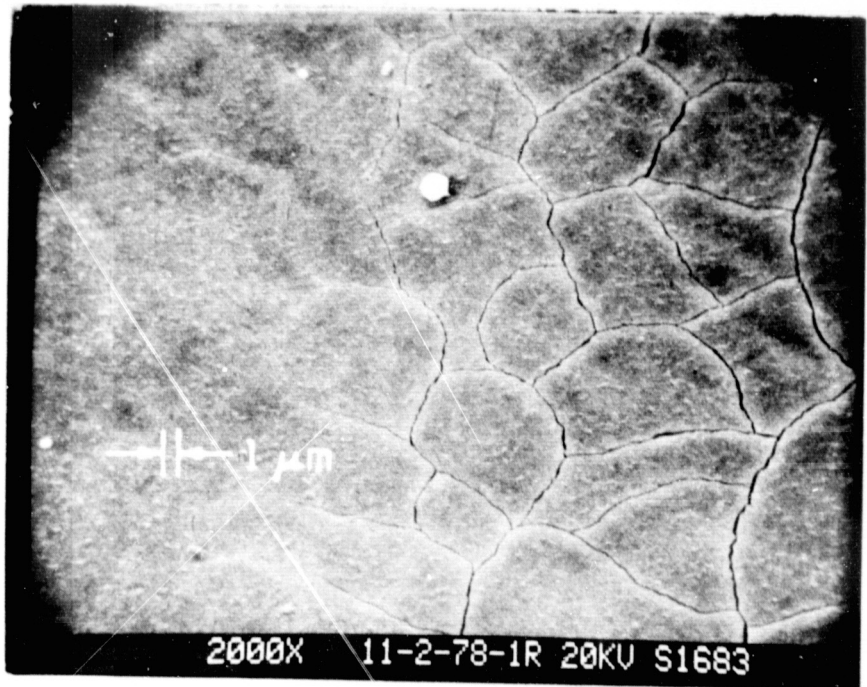


Figure 3-6. SEM Photograph of Pulsed e-Beam Melted Ge on Tungsten Substrate

2. Substrate Passivation

The use of low-cost, conducting substrates such as steel is economically desirable for thin-film solar cells. However, such substrates will also introduce metallurgical problems due to excessive alloying/diffusion of the substrate material with/into the Ge film during recrystallization, and subsequently, diffusion into the GaAs film during CVD growth. To reduce these problems, a passivation layer is needed to prevent interaction of such substrates with the semiconductor top layers. The criteria for choosing an ideal passivation layer (PL) can be described as follows (Ref. 11): (1) the rate of interdiffusion of the substrate and Ge/GaAs through the PL should be small; (2) the loss-rate of the PL into the adjacent materials should

be small; (3) the PL should be thermodynamically stable; (4) there should be strong adhesion between the PL and the adjacent materials; (5) the PL should be pin-hole free; (6) the PL should be resistant to thermal and mechanical stresses; (7) the specific contact resistance between the PL and the adjacent materials should be small; and (8) the PL should be thermally and electrically conducting. Clearly, all conditions described above cannot be fulfilled at once, necessitating a compromise. In practice, an empirical approach is needed due to lack of experimental data associated with most coatings. Because of the demonstrated usefulness of W in terms of the Ge bonding, wettability, and Ge crystallite size upon recrystallization, studies on the use of thin CVD coatings of W, or of W:C alloys in conjunction with Ni-plated layers on steel, were initiated with the Chemetal Company, Pacoima, California. The purpose of the Ni coating was to improve the bonding between the W and the steel.

Prior to using steel substrates, W films were deposited by reduction of WF_6 in H_2 ($\text{WF}_6 + 3\text{H}_2 \rightarrow \text{W} + 6\text{HF}$) at $550^\circ\text{C} - 570^\circ\text{C}$ on $2 \times 4-inch size, 25-mil thick Ni sheets. The Ni sheets were later sheared or sawed to a standard substrate size of 22×22 mm on which subsequently $0.1 \mu\text{m}$ of Si and $10 \mu\text{m}$ of Ge were deposited. The thin Si layer served to promote the bonding of Ge to W. The EDAX methods showed that at low laser-power levels (<30 W), no Ni appeared on the top surface after recrystallizing the Ge with 530°C background-heating temperature. However, when the laser power was increased to the 50 W level with other conditions unchanged, considerable amounts of Ni appeared on the surface. Figure 3-7 is a SEM picture of such a sample after recrystallization at 50 W laser-power level. The small, white lumps shown in Figure 3-7 consisted of Ni/W/Fe alloys while the large$

white lump was principally Ni. The failure of the CVD W film as a passivation layer is thus evident at higher-laser power levels. When the laser power was further increased to 80 W with all other conditions fixed, total failure of the W film as a passivation layer was evident from the observation of excessive alloying between Ge and Ni -- as shown in Figure 3-8.

Further investigation of the W passivation layer was made by analyzing a cross-section of one of the recrystallized samples with an electron microprobe. An optical micrograph of the cross-section of a sample similar to that used for Figure 3-8 is shown in Figure 3-9. A corresponding elemental map of W, Ge, Ni, and Si obtained by the electron microprobe is shown in Figure 3-10. The elemental map uses a higher magnification factor than that of the optical micrograph; hence, only part of the optical photograph is covered by the elemental map. In the elemental map, the brighter the image, the higher the concentration of the particular element of interest. From Figures 3-9 and 3-10, it is evident that the area under the center of the laser heating had excessive migration of Si and Ge through the W into the Ni substrate. (The spacing between the darker hemispherical areas in the nickel on the optical micrograph matches the calculated spacing between laser scan-lines, given the pull and scan rate.) While the optically darker Ge is concentrated in the inner part, the optically lighter Si is segregated at the periphery of the hemispheres. In addition, the Ni penetrated through microcracks of the W passivation layer and alloyed with the Ge. Microcracking is indicated by the faint, dark region appearing approximately in the center of the W photograph and the corresponding brighter region appearing in the same location on the Ni, Ge and Si elemental maps.

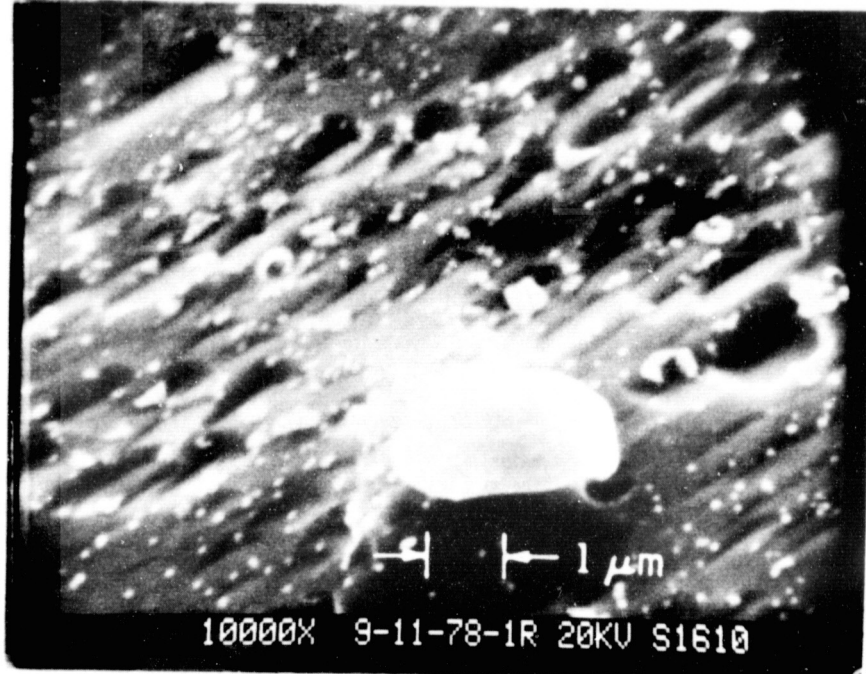


Figure 3-7. SEM Photo of Low Laser-Power (50 W)
Recrystallized Ge/W/Ni

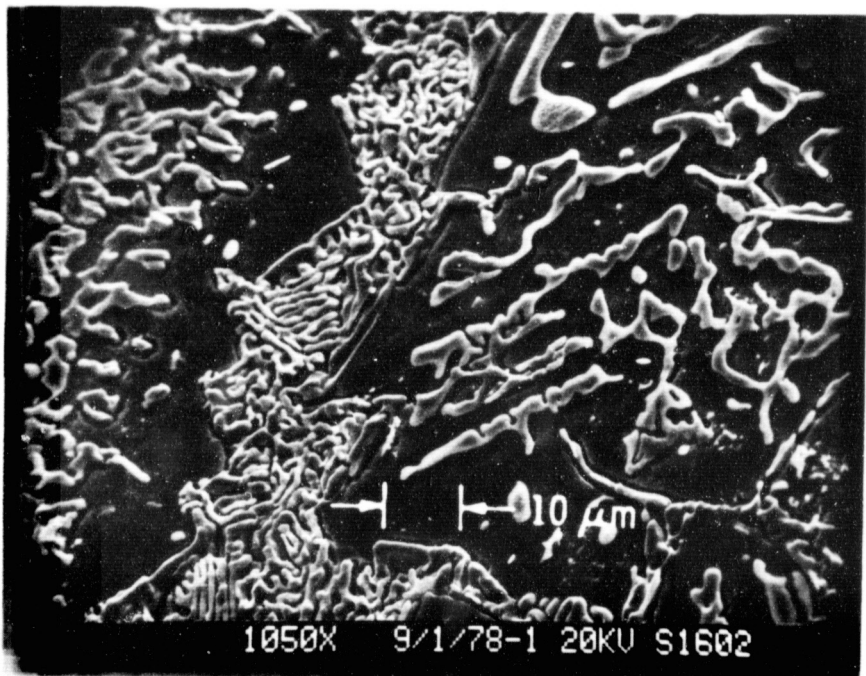


Figure 3-8. SEM Photo of High Laser-Power (80 W)
Recrystallized Ge/W/Ni

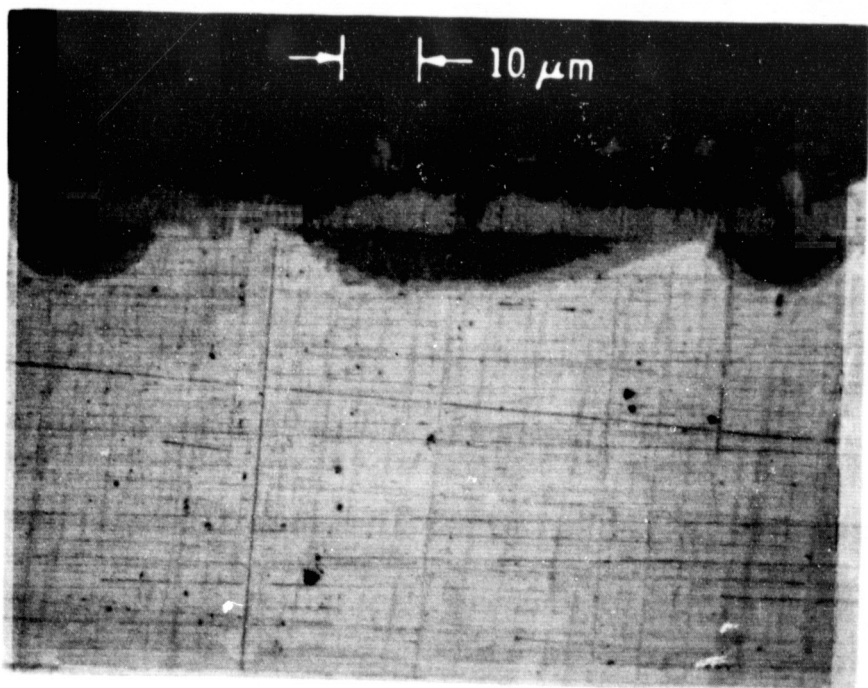
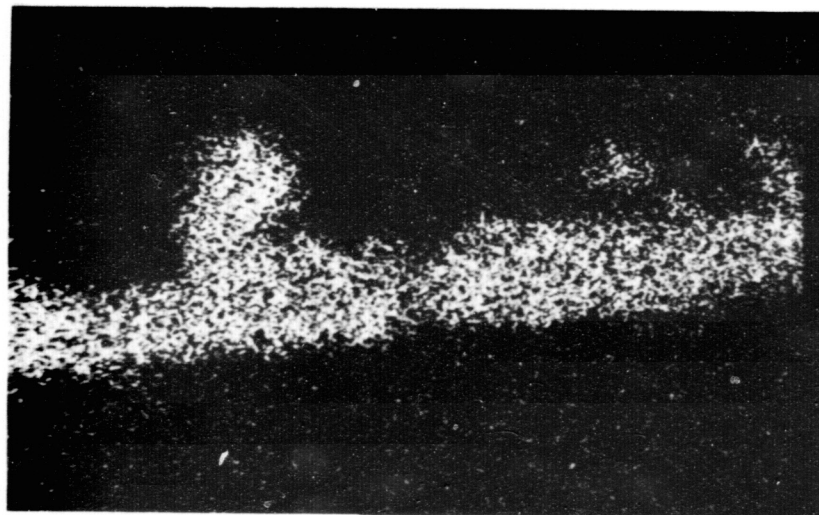
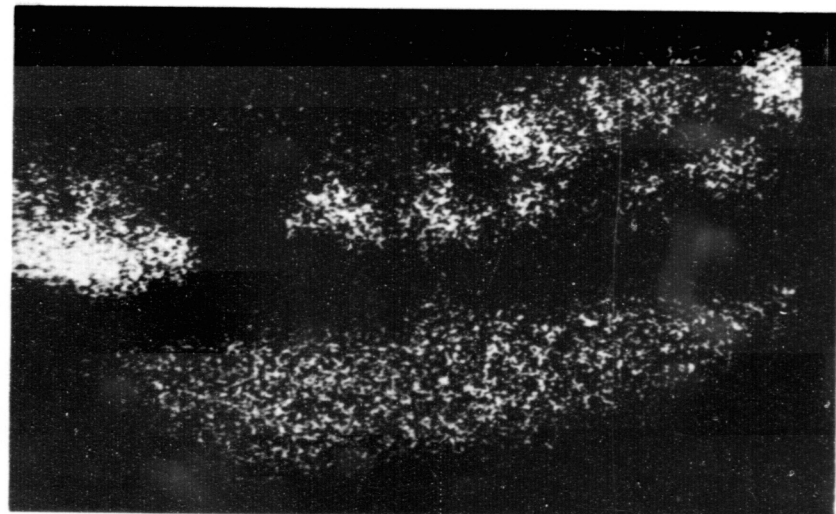


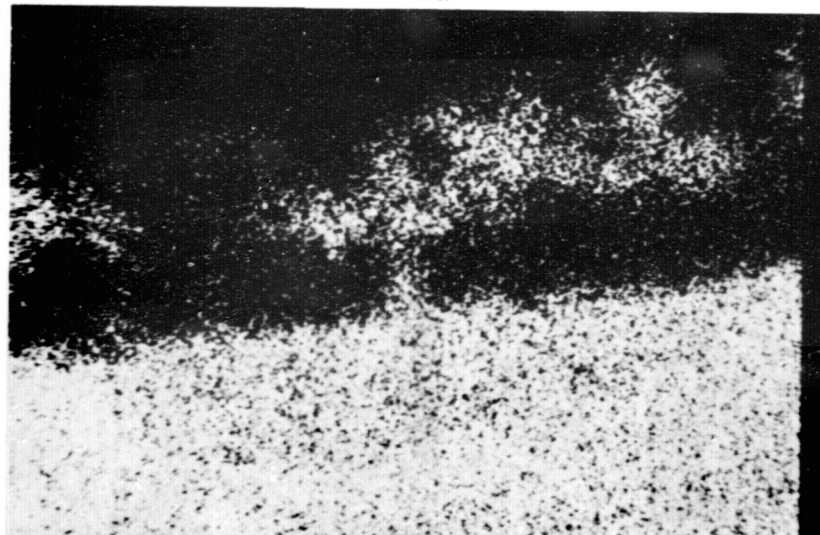
Figure 3-9. Cross-section Photomicrograph of Recrystallized Ge/Si/W/Ni Substrate with High Background Heating (530 C) and High Laser-Power (80 W)



W $L\alpha$



Ge $K\alpha$



Ni $K\alpha$



Si $K\alpha$

Figure 3-10. Elemental Map of Sample in Figure 3-9

Since these CVD W samples were subjected to shearing and sawing before the deposition of Ge, one might question whether the cutting process introduced stress in the CVD layer, thereby inducing micro-cracks. Therefore, CVD W films were deposited on Ni sheet substrates precut to the 22 x 22 mm size. In addition, different growth-temperatures (400 C - 900 C) were used to vary the built-in stresses due to mismatches between the W layer and Ni sheet. Hydrogen-to-WF₆ gas ratios were also varied with the temperature in order to maintain the desired fine-grain, noncolumnar growth of W. These samples did show reduced out-diffusion of Ni through the W and Ge films after recrystallization. However, unacceptable amounts of Ni and other metallic contaminations still appeared randomly with the standard amount of background heating (530 C) and laser power (60-80 W).

Subsequently, deposition of CVD W and W:C (1%) proprietary coatings (CM-500) were prepared at Chemetal on Cl018 low-carbon steel substrates. The steel substrate had first been plated with a thin Ni coating to improve the bonding of the CVD coatings. Conventional thicknesses of Si (0.1 μm) and Ge (10 μm) were then e-gun deposited and the samples recrystallized with 530 C background heating and 80 W of laser power. A SEM photograph of the recrystallized Ge/Si/CM500/Ni/Steel substrate is shown in Figure 3-11. In this photograph, the small, light lumps are W/Ge, as is usually seen with bulk W sheet. The large, light lump is Cu, due to contamination from the e-gun hearth. No evidence of Ni or Fe was seen, indicating that CM500/W/Ni may act as a passivation layer for low-cost Cl018 steel substrates. However, the problem of W/Ge alloying still remains, at least with the present conditions of background temperature and laser power.



Figure 3-11. SEM Photo of Ge Recrystallized on CM500/W/Ni/1018 Steel Substrate

B. GaAs GROWTH ON GERMANIUM LAYERS

1. Properties of OM-CVD GaAs Grown on Single-Crystal GaAs

It is essential to optimize the growth parameters of GaAs layers on single crystal substrates in order to improve the growth of GaAs layers on recrystallized germanium. For this reason, the growth rates, surface morphology, and electrical characteristics were investigated on OM-CVD GaAs layers grown on single-crystal substrates with the new JPL facility (Figure 3-12).

A 40-mm I.D. quartz reactor tube with susceptor designed to hold two 2.2 x 2.2 cm substrates is shown in the photograph. A Lepel 10 kW RF power supply (shown on the right side of the photograph) is used for induction heating of the graphite susceptor, which has had a glassy carbon coating for reducing contamination. The Matheson hydrogen purifier is shown in the lower center of the photograph on the far left. Trimethyl gallium (TMG) and arsine (AsH_3) were used as the Ga and As sources, respectively.

Both Te-doped n-type ($2 \times 10^{17} \text{ cm}^{-3}$) and Cr-doped semi-insulating GaAs substrates with crystal orientation approximately 2° off [100] toward the [110] direction were used for evaluation of the single-crystal growth. The Te-doped and Cr-doped substrates were obtained from Epidyne Inc. and Laser Diode Inc., respectively. Prior to CVD growth, the GaAs substrates were degreased with hot trichloreethylene, acetone, and methanol, followed by a hot $\text{SHH} (\text{H}_2\text{SO}_4:\text{H}_2\text{O}_2:\text{H}_2\text{O} = 10:1:1)$ chemical etch at 60 C for 45-60 seconds. The substrates were rinsed with running deionized water and dried with gaseous nitrogen.

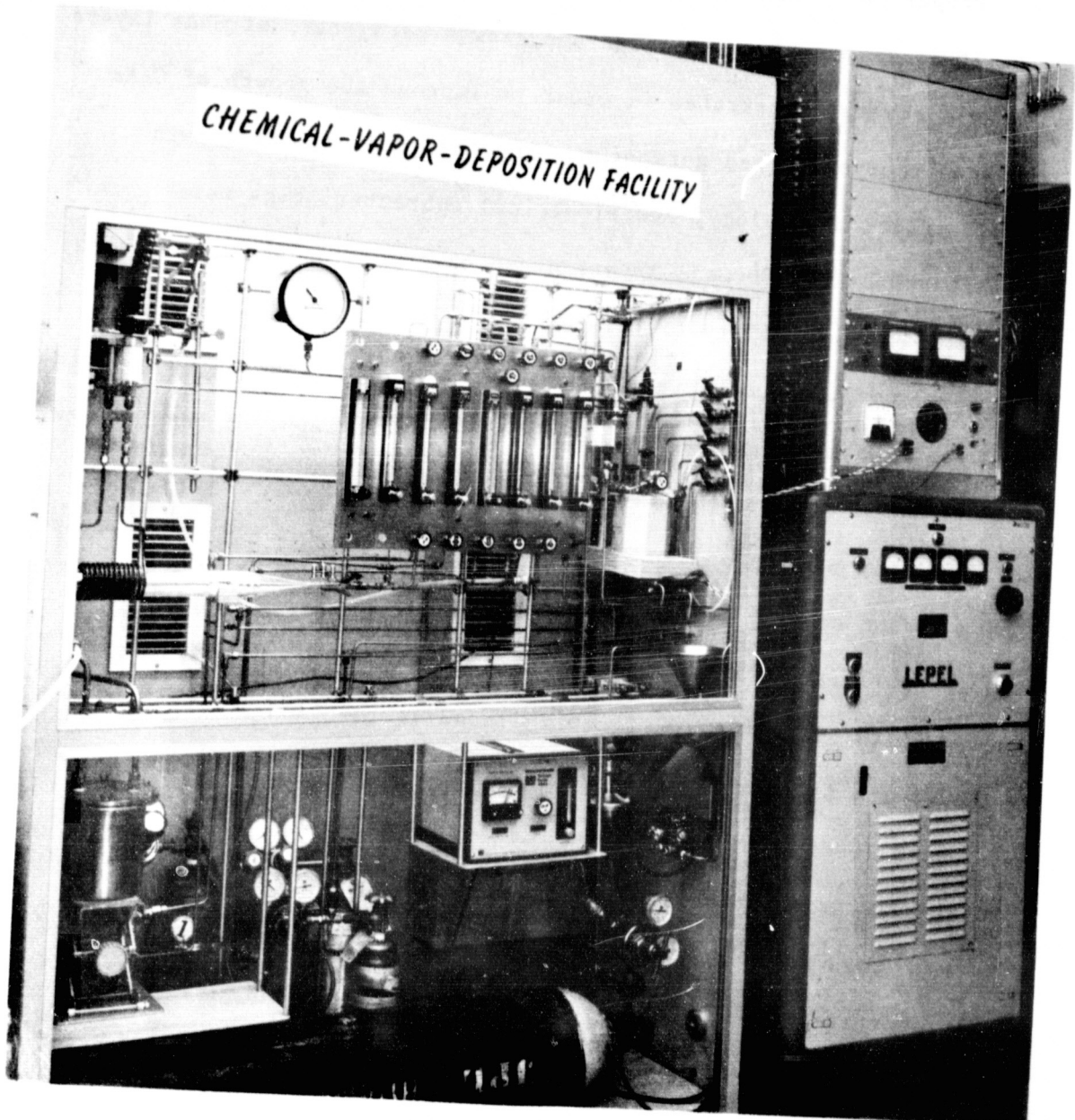


Figure 3-12. Photograph of JPL OM-CVD Facility

The growth rate of OM-CVD GaAs depends on the flow rates of the hydrogen and TMG as well as the growth temperature. The AsH_3 pressure needs to be higher than that of the TMG in order to produce stoichiometric layers. With at least 3 l/min hydrogen flow rate, uniform thickness over the entire 20 x 20 mm sample area was observed. The thickness of the epi-layer was optically measured after cleaving and etching (5 sec AB etch) the single-crystal GaAs wafer. To study the functional dependence of the growth rate, systematic experiments were performed using various gas flow rates, mole ratios, and growth temperatures. The growth rate was found to be linearly dependent on the TMG mole fraction within the experimental conditions (600 to 750 °C, 1 to 3 l/min H_2 , and 10^{-4} to 10^{-3} TMG mole fraction.) The GaAs growth rate in units of $\mu\text{m}/\text{min}$ was found to be equal to 556 times the mole fraction of TMG, within the above range of variables.

Good surface morphology was observed for GaAs growth with an As/Ga mole ratio of more than 3. When the As/Ga mole ratio was less than 3, excessive surface pits were observed as shown in Figure 3-13. Surface roughness was also observed when growth temperatures lower than 600°C were used - perhaps due to the lower surface mobility at lower growth temperatures.

Electrical characterizations were made on the epitaxial n-type GaAs layers. For undoped samples, mole ratios of As/Ga from 5 to 11 were investigated. In the case of S-doped samples, the mole fraction of H_2S was varied between 5×10^{-9} and 7×10^{-7} .

Resistivity and Hall coefficient measurements were made by the van der Pauw technique (Ref. 12), using ohmic contacts of pure indium

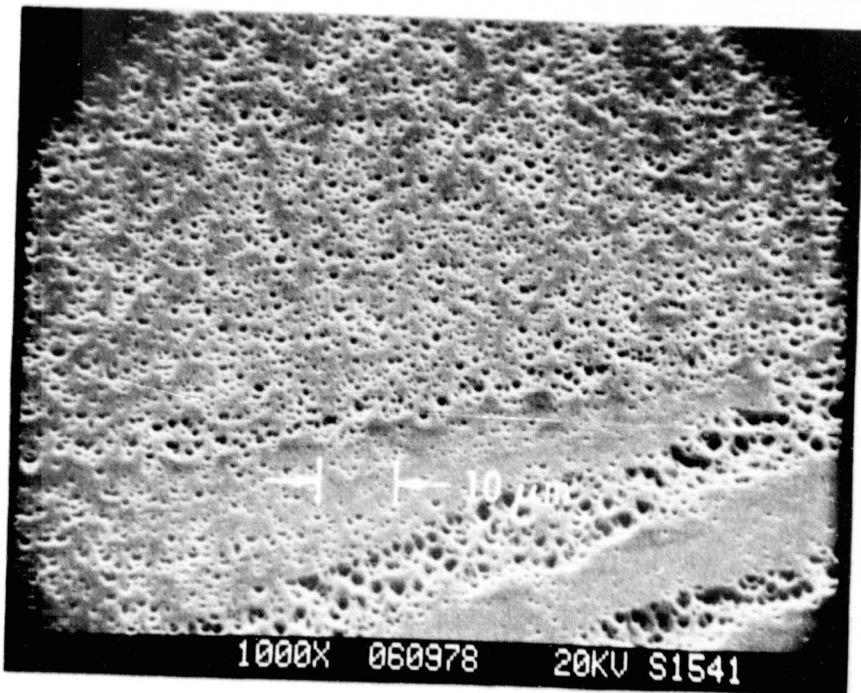


Figure 3-13. Typical SEM Photomicrograph of GaAs Grown on Single-Crystal GaAs Substrate with As/Ga Ratio of Less than 3

sintered at 350 C in H₂ for 5 minutes. When temperature-dependence measurements were made, the sample was mounted on a specimen stage in a Displex dewar (Air Products) with sample temperature controllable from 10 to 400 K.

The resistivity (ρ) and the Hall coefficient R_H were calculated according to the following equations:

$$\rho(\pi/n^2) (f) (V_c/I_c) (t) \quad \text{ohm-cm. ----- (1)}$$

$$R_H = (10^8/B) (V_H/I_C) (t) \quad \text{cm}^3/\text{coul. ----- (2)}$$

Here, V_C is sample voltage, I_c is sample current, t is the epi-layer thickness, B is the magnetic induction (usually 5000 gauss), V_H is the Hall voltage, and f is the van der Pauw geometrical symmetry correction factor. A correction is needed in using equations (1) and (2) to take into account the shorting effects of contacts with finite dimensions. For practical structures with the ratio between the total length of the contacts and the length of the boundary equal to 0.1, the maximum error introduced can be estimated to be about 10% by either the finite difference method (Ref. 13) or by conformal transformation (Ref. 14). To minimize the correction factor, mesa-etching was performed on all samples to isolate the contact pad. Hence, negligible measurement error due to finite-contact area was insured.

The resistivity and Hall coefficient measurements for undoped samples were made in the temperature range between 10 and 300 K. The temperature dependence of ρ and R_H is shown in Figures 3-14 and 3-15, respectively, for mole ratios of As/Ga from 5 to 11. The Hall coefficient decreased with increasing mole ratio, indicating an increase in carrier concentration. For samples with As/Ga equal to 5 and 8, R_H increased with $1/T$ in the usual manner. However, for As/Ga equal to 11, R_H did not increase with $1/T$ indefinitely, but showed a maximum at low temperature (~ 40 K) indicating the onset of impurity conduction.

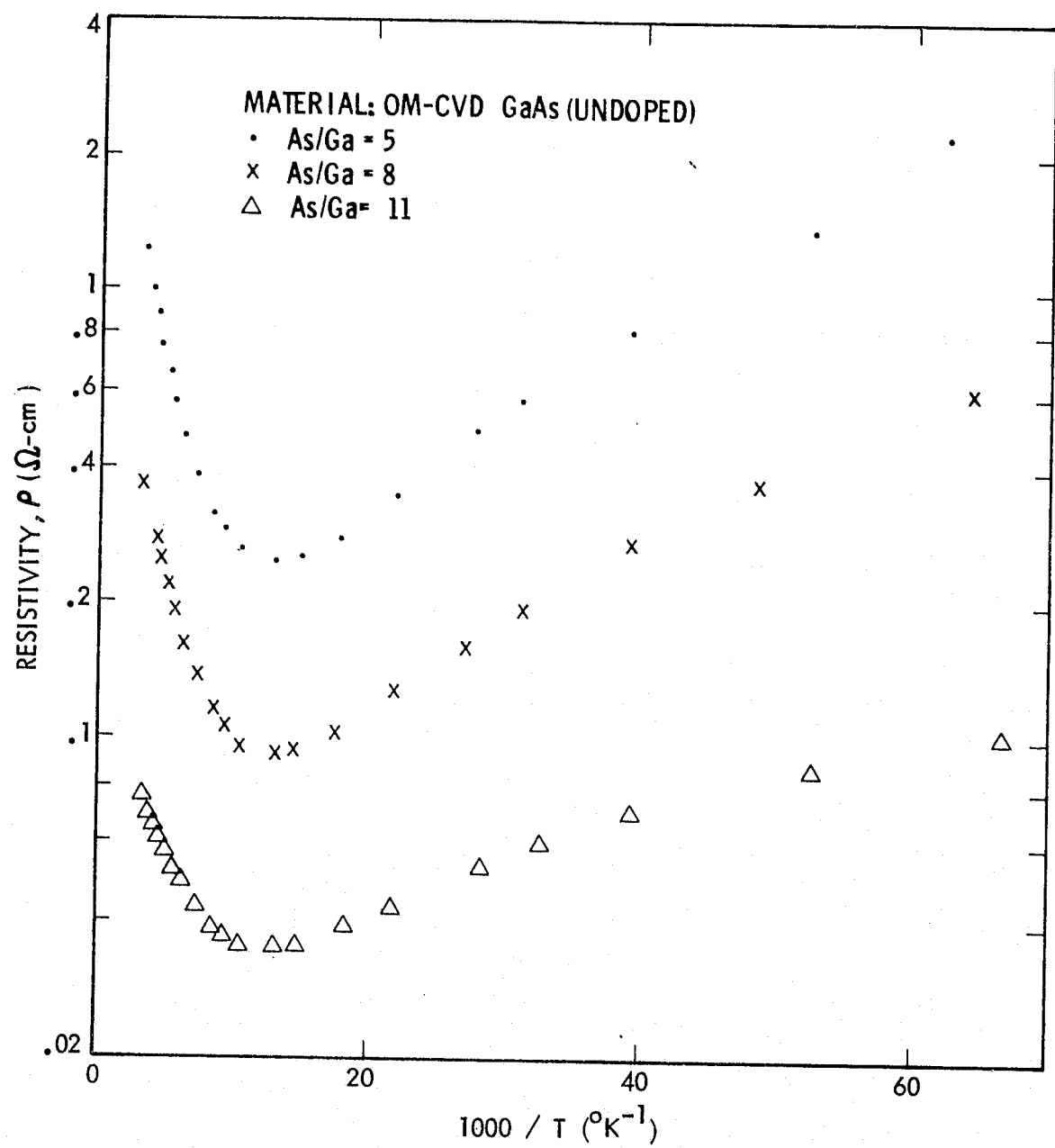


Figure 3-14. Temperature Dependence of Resistivity of OM-CVD GaAs Layers

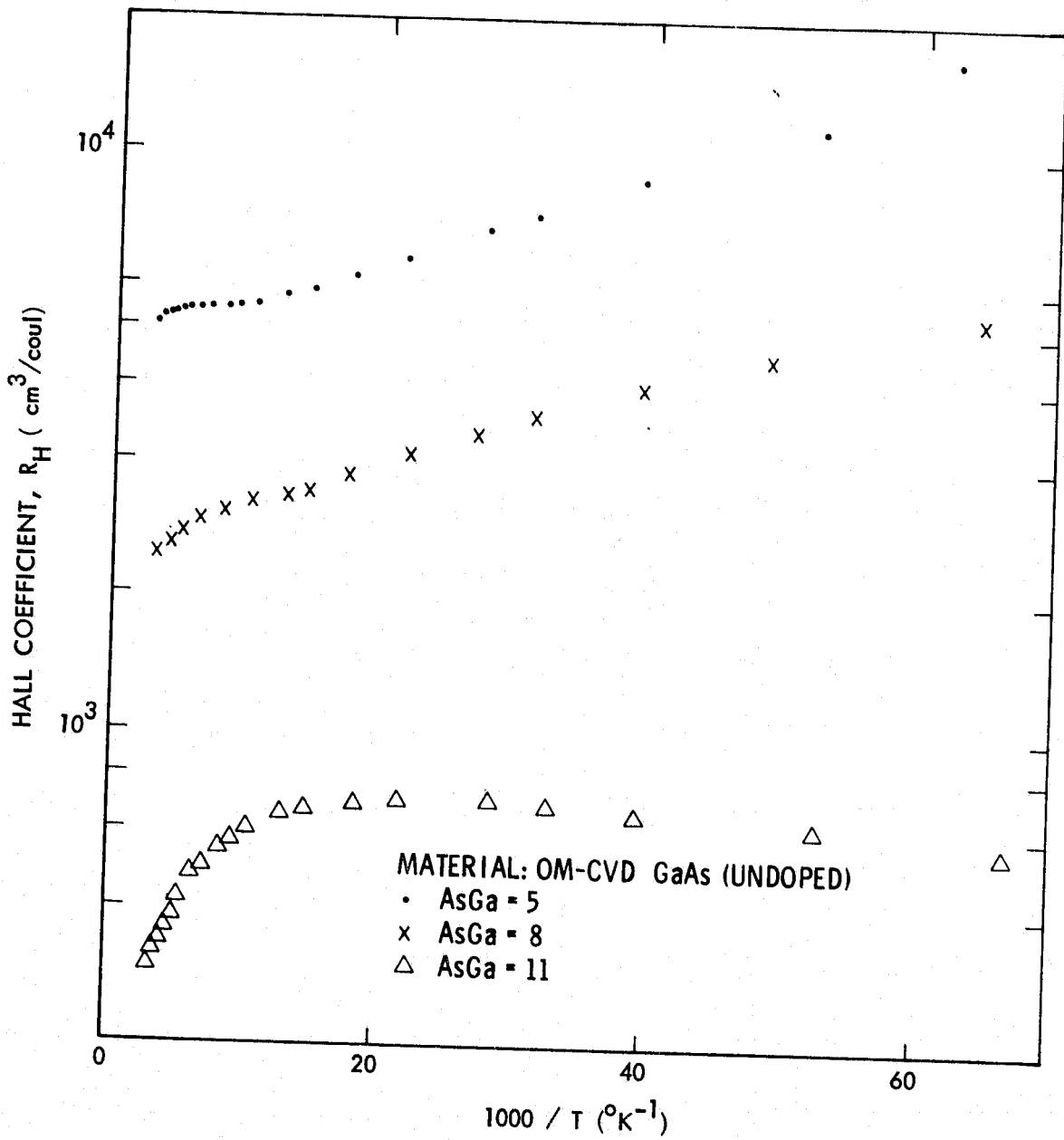


Figure 3-15. Temperature Dependence of Hall Coefficient of OM-CVD GaAs Layers

From ρ and R_H , the Hall mobility (μ_H) and the carrier concentration (n) can be calculated by:

$$\mu_H = \frac{R_H / \rho}{(cm^2/V\cdot sec)}, \quad (3)$$

$$n = (r) / (q R_H) \quad (\text{carriers/cm}^3), \quad (4)$$

where q is the electronic charge and r is the Hall factor. The Hall factor depends on the band structure, the degree of degeneracy, the scattering mechanisms, the magnetic induction, and the sample temperature. The value of r was assumed to be equal to one.

Temperature-dependence curves of the Hall mobility for samples with As/Ga mole ratio of 5, 8, and 11 shown in Figure 3-16 are typically representative of undoped OM-CVD GaAs. The mobility initially rises with increasing temperature to a maximum near 70 K. At low temperatures, impurity scattering is the dominant mechanism giving a mobility proportional to $T^{3/2}$, while at higher temperatures, lattice scattering causes the mobility to decrease with increasing temperature -- roughly as $1/T$.

From the plot of n vs. $1/T$ (Figure 3-17), the concentration of impurities (donors N_D and acceptors N_A) and the energy level (E_D) of the dominant dopant can be obtained. For samples grown with mole ratios of 5 and 8, deionization of the dominant dopant at temperature below 50 K causes a decrease in the net carrier concentration.

For a one-carrier system, the temperature dependence of the free carrier concentration $n(T)$ is given by:

$$\frac{n(T)}{\left(\frac{(N_D - N_A)}{N_A} - n(T)\right)} = \frac{N_c(T)}{g} \exp\left(-\frac{E_D}{kT}\right). \quad (5)$$

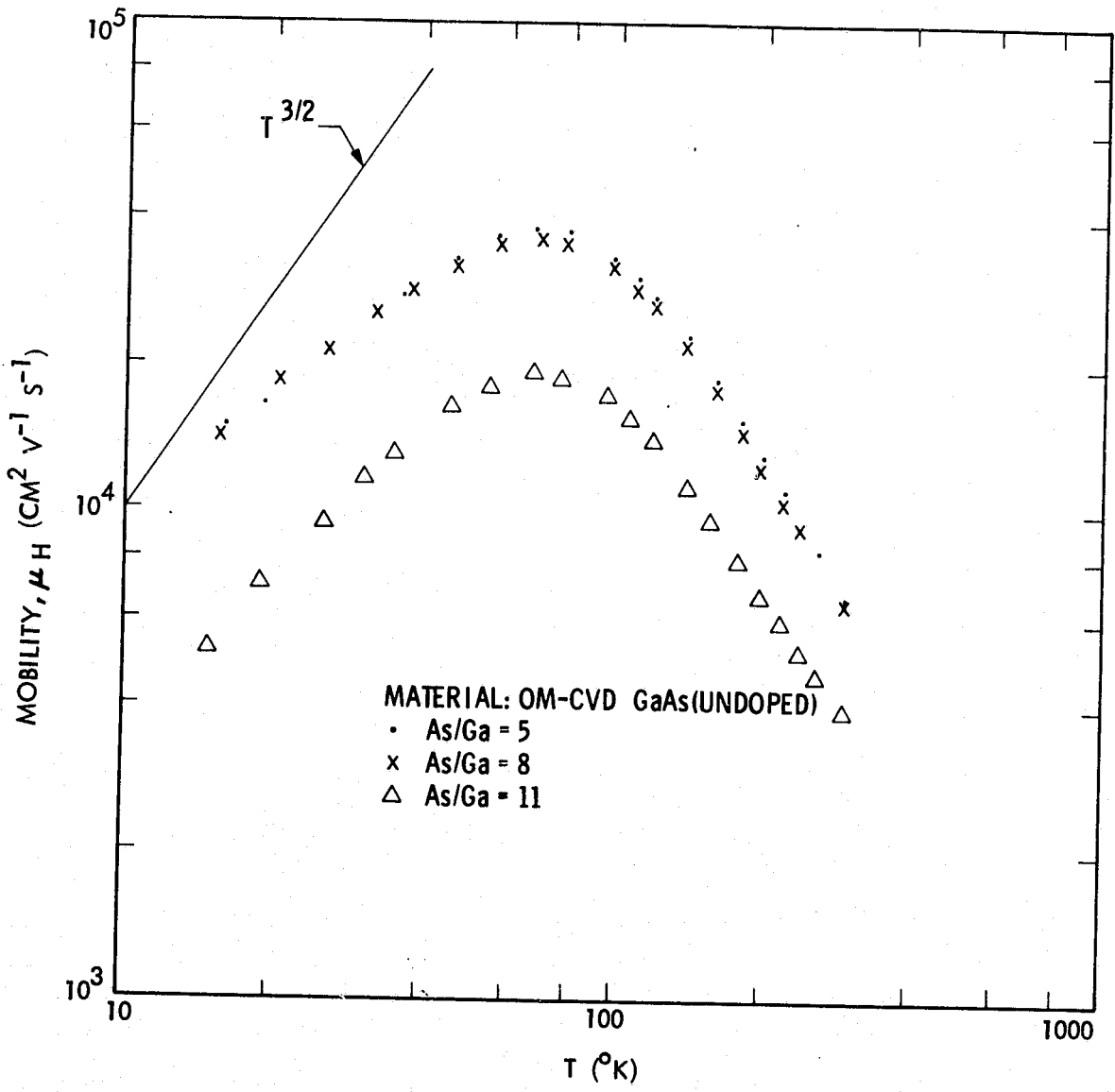


Figure 3-16. Temperature Dependence of Hall Mobility of OM-CVD GaAs Layers

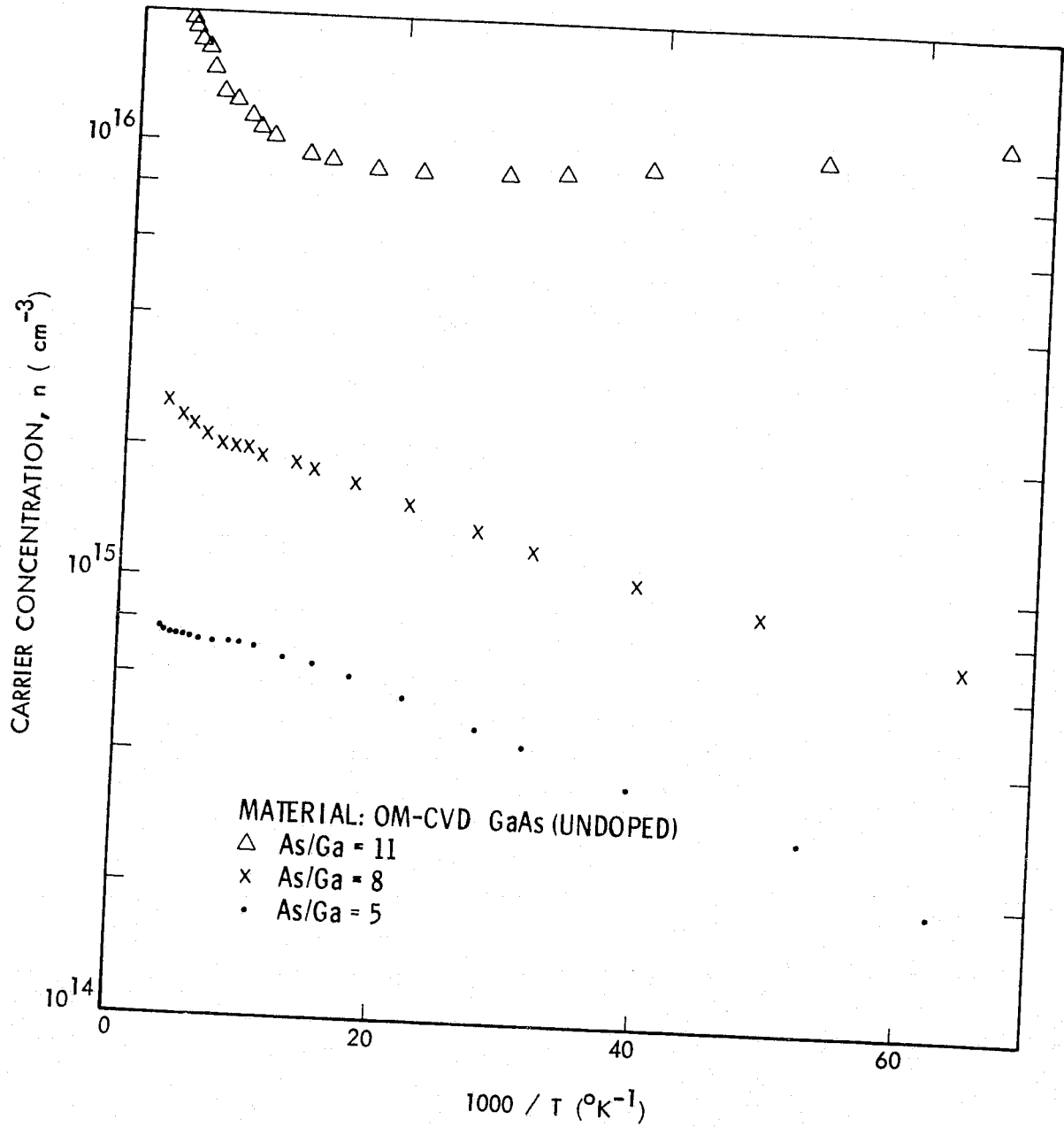


Figure 3-17. Temperature Dependence of Carrier Concentration of OM-CVD GaAs Layers

Here, N_c is the conduction-band density of states, g is the degeneracy factor (equal to 2 for n-type), and k is the Boltzmann constant. For n-type GaAs, the equation simplifies to

$$\frac{n(T) [n(T) + N_A]}{(N_D - N_A) - n(T)} = 4.188 \times 10^{13} (T)^{3/2} \exp \left[- \frac{1.61 \times 10^4 E_D}{T} \right]. \quad (6)$$

When Eq. (6) was applied to the As/Ga sample with mole ratio of 5, the measured impurity concentrations were $N_D = 2 \times 10^{15} \text{ cm}^{-3}$ and $N_A = 1.4 \times 10^{15} \text{ cm}^{-3}$. The calculated value for E_D was 2.6 meV. For an undoped epitaxial GaAs sample with $N_D = 2 \times 10^{15} \text{ cm}^{-3}$, a value of 3.3 meV has previously been reported (Ref. 15), in fair agreement with the present value. For comparison purposes, a value for the "hydrogenic" donor binding energy of 7 meV was calculated by using an electron effective mass $m_e^* = 0.067 m_0$ and a static dielectric constant $\epsilon_s = 12.8$.

For samples with As/Ga mole ratio equal to 8 or larger (see Figure 3-17), the low-temperature tail of n vs. $1/T$ begins to deviate from linearity, indicating some influence of impurity conduction. For a mole ratio of 11, this effect is clearly evident. According to Mott and Twose (Ref. 16), the critical donor concentration at which the impurity conduction becomes "free" (zero activation energy), is given by $N_{cr} \approx (0.25/a_i)^3 \approx 1.5 \times 10^{16} \text{ cm}^{-3}$, where a_i is the effective Bohr radius for an electron, given by $a_i = a_B \epsilon_s (m_e^*/m_e)$ with $a_B = 0.529 \text{ \AA}$ is the Bohr radius. This assumes a hydrogenic model, which may not be too inaccurate, since the predicted donor binding energy is about 7 meV -- reasonably close to the measured value. According to Reference 17, the Fermi level should cross the conduction

band edge at a concentration of $N_{cb} \simeq 5 N_{cr} \simeq 7.5 \times 10^{16} \text{ cm}^{-3}$ for $T \ll T_{\text{Fermi}}$.

When $n > N_{cb}$, the electrons will be totally degenerate, and n should be independent of temperature at lower temperatures. This effect has been observed for the sample with an As/Ga mole ratio of 11, where $n \sim 1 \times 10^{16} \text{ cm}^{-3}$ for $T < 100 \text{ K}$. The foregoing temperature-dependence analysis clearly indicates the non-degenerate to near-degenerate transition between the As/Ga = 5 and the As/Ga = 11 sample. Hence, the one-carrier conduction analysis is no longer valid for As/Ga = 11 and a modified two-band (the impurity and conduction band) model must be used.

The results of electrical characterization obtained at 77 and 300 K are listed in Table 3-1 for samples with As/Ga equal to 5, 8, and 11 mole ratios. In the lowest-doping case (As/Ga = 5), the room temperature Hall mobility value of $7790 \text{ cm}^2 \text{V}^{-1} \text{sec}^{-1}$ is better than most values obtained from similar CVD reactor systems (Refs. 18-20). The 77 K mobility for this sample is $41,000 \text{ cm}^2 \text{V}^{-1} \text{sec}^{-1}$. Experimentally, the best mobilities for liquid-phase-epitaxial GaAs are $8,200$ - $8,900 \text{ cm}^2 \text{V}^{-1} \text{sec}^{-1}$ (Ref. 21) and $200,000 \text{ cm}^2 \text{V}^{-1} \text{sec}^{-1}$ (Ref. 22) at 300°K and 77°K , respectively.

Table 3-1. Electrical Parameters of OM-CVD GaAs Samples
With As/Ga Mole Ratio of 5, 8, 11 at 300 and
77 K

| Mole Ratio (As/Ga) | 5 | 8 | 11 |
|---|-----------------------|-----------------------|-----------------------|
| ρ ($\Omega \text{-cm}$) | 1.17 | .371 | .085 |
| 300 K | | | |
| μ_H ($\text{cm}^2/\text{V-sec}$) | 7790 | 7250 | 4750 |
| n (cm^{-3}) | 6.86×10^{14} | 2.32×10^{15} | 1.55×10^{16} |
| 77 K | | | |
| ρ ($\Omega \text{-cm}$) | 0.25 | .095 | .039 |
| | | | |
| μ_H ($\text{cm}^2/\text{V-sec}$) | 41,000 | 38,700 | 22,800 |
| n (cm^{-3}) | 5.99×10^{14} | 1.70×10^{15} | 7.04×10^{15} |

Table 3-2 presents an estimate of compensation ratio ($K = N_A/N_D$) for samples with As/Ga = 5, 8 and 11. Typically, the lower the value of compensation ratio, the better will be the quality of crystal for samples with identical net carrier concentration. Three different methods (indicated as T-fit, Wolfe, and Rode) were used and compared to provide relative certainty in the estimation of the K value. In the T-fit method, the K value is calculated by using the N_D and N_A values obtained from fitting of $n(T)$ vs. $1/T$ using equation (6). In the Wolfe method, the empirical relation between the mobility and the concentration established by Wolfe and Stillman

(Ref. 23) is used, applied to electrical data obtained for samples with a wide range of concentrations measured at 77 K. In the Rode method, Rode and Knight (Ref. 24) formulated a theoretical estimation of the electron mobility as a function of n, including scattering factors as well as degeneracy. The K values are in fair agreement for all three methods employed to obtain the estimation.

Table 3-2. Estimates of Compensation Ratio K, Using T-fit, Wolfe, or Rode Method

| Mole Ratio (As/Ga) | 5 | 8 | 11 |
|-----------------------|------|------|------|
| T-Fit | 0.70 | 0.35 | - |
| Wolfe | 0.76 | 0.59 | 0.51 |
| Rode | - | 0.25 | 0.55 |

It has been shown in the previous discussions that the carrier concentration of undoped GaAs can be changed simply by changing the mole ratio of As/Ga. However, dopant incorporation is much preferred, since crystals with better stoichiometry are of higher quality. For this reason, a regulated H₂S source was incorporated into the CVD reactor. By using 10.8 ppm H₂S in N₂ as the n-type dopant source, samples with doping concentration from 10¹⁵ to 5x10¹⁶ cm⁻³ range were obtained. This doping range is most useful in SB solar cell applications. For doping concentrations N_D between 2 x 10¹⁵ and 5 x 10¹⁶ cm⁻³ (H₂S mole fraction between 4 x 10⁻⁸ and 7x10⁻⁷), n changes linearly with the mole fraction of H₂S at a

700 C growth temperature, using AsH_3 and TMG flow rates of 1.9×10^{-4} and 4.5×10^{-5} mole/min, respectively (Figure 3-18). Good reproducibility was observed; i.e., two runs with identical growth settings produced samples with $n = 5.2 \times 10^{16} \text{ cm}^{-3}$ and $4.7 \times 10^{16} \text{ cm}^{-3}$. However, for H_2S mole fraction below 10^{-8} , scatter in the experimental data indicates nonreproducibility of dopant incorporation.

To summarize the electrical characterization results, a plot of the experimental Hall mobility as a function of carrier concentration for both undoped and S-doped GaAs is given in Figure 3-19. Theoretical fits of the electron drift mobility (see Ref. 24) as a function of n are shown as solid curves, where each curve forms an iso-compensation fit for $K = 0, 0.3, 0.6$, and 0.9 . In undoped samples, it is apparent that the compensation effect becomes severe at $n = 2 \times 10^{16} \text{ cm}^{-3}$ for $\text{As}/\text{Ga} = 11$ and in this concentration range, much better results are obtained by S incorporation.

The fact that GaAs is a binary compound introduces stoichiometric problems which influence the incorporation of dopant atoms. The group II elements (Zn, Cd, etc.) act as acceptors on Ga sites, the group VI elements (S, Se, Te, etc.) act as donors on As sites, while the group IV elements are amphoteric; e.g., are acceptors on As sites and donors on Ga sites. Higher As/Ga mole ratios tend to increase the availability of Ga or group IV substitutional donor sites at the expense of As or group II substitutional acceptor sites. High resolution photoluminescence spectra (Ref. 25) obtained at liquid helium temperature on JPL-grown GaAs crystals show two sharp emission lines at 1.493 eV and 1.489 eV for undoped samples. The emission line at 1.493 eV has been identified as due to C acceptors (Ref. 26). This

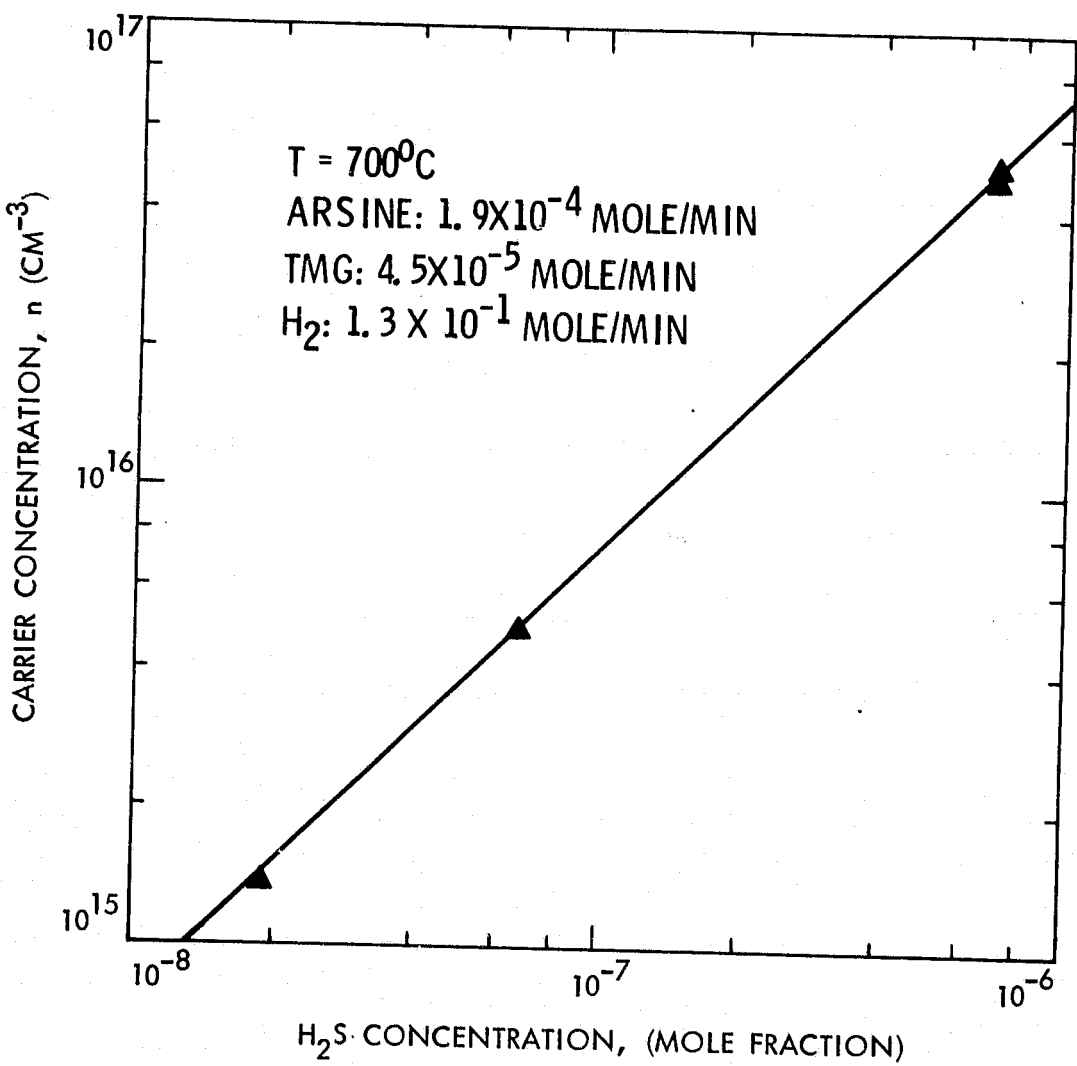


Figure 3-18. Carrier Concentration vs Hydrogen Sulfide Concentration for OM-CVD GaAs

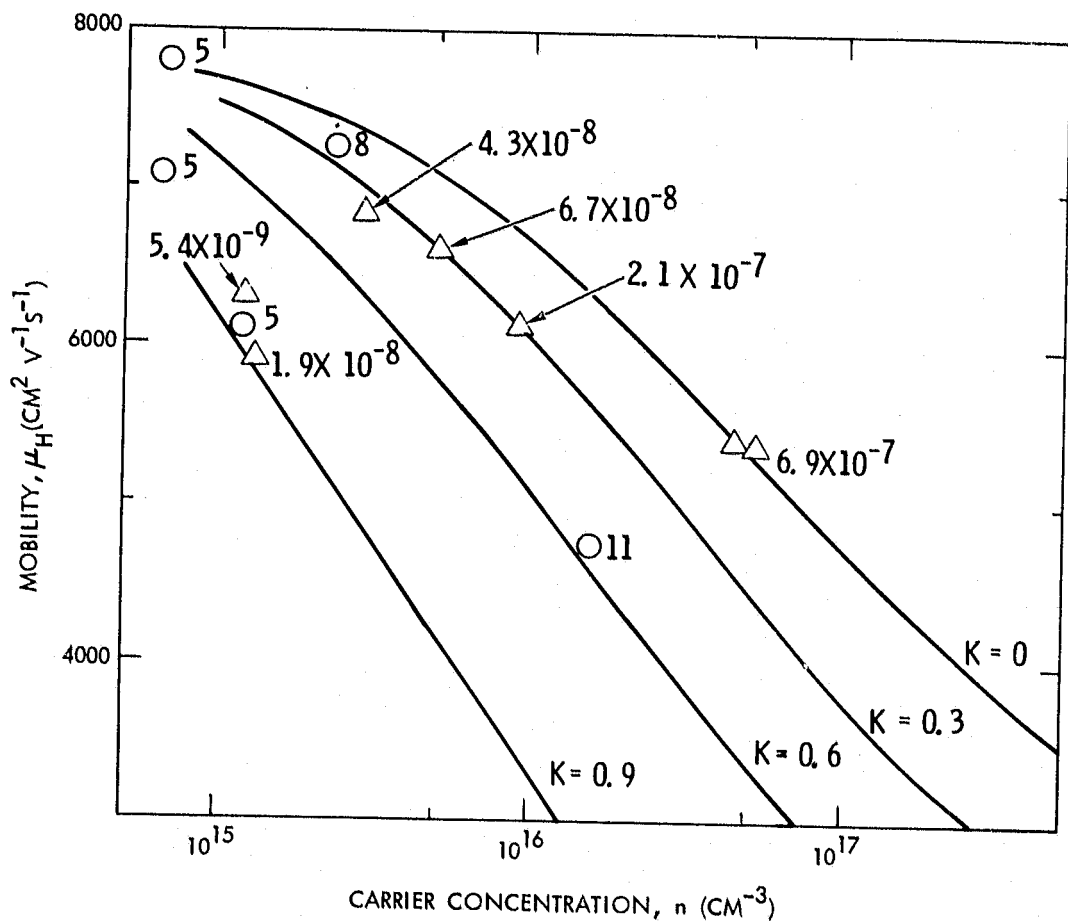


Figure 3-19. Mobility and Compensation Ratio of S-doped (Triangle) and Undoped (Circle) OM-CVD GaAs. The As/Ga ratio is indicated by numbers next to the circles and the mole fraction of H₂S is given adjacent to the triangle

line is present in all samples as might be expected from the incomplete formation of methane, which is a by-product of the reaction between TMG and AsH_3 (Ref. 27). The acceptor-like emission at 1.489 eV is gradually enhanced as the As/Ga mole ratio is increased. Although the origin is not known, this emission line is possibly due to amphoteric Si on As sites. An emission line associated with Si has been reported in the epitaxial layers grown by the Ga-AsCl_3 CVD method (Ref. 28).

Low As/Ga ratios will tend to create more available As sites into which S can be incorporated, and minimize undesirable incorporation of acceptor-like dopants, such as was observed in the photoluminescence data in the higher As/Ga mole-ratio samples. In fact, it can be shown from thermodynamics that the effective number of As vacancy sites can be increased by decreasing the growth temperature and producing conditions favorable for the incorporation of group VI substitutional donors such as S. This is verified from the experimental results (for mole fractions of 1.63×10^{-3} , 3.85×10^{-4} , and 1.94×10^{-8} for AsH_3 , TMG, and H_2S , respectively), where growth temperatures of 600, 650 and 700 C produced carrier concentrations of 9.5×10^{15} , 3.3×10^{15} , and $1.34 \times 10^{15} \text{ cm}^{-3}$, respectively. Hence, a reduction of 100 C in temperature increases the carrier concentration by almost one decade. In the present CVD system, high quality S-doped epitaxial GaAs layers can be grown in the range between 2×10^{15} and $5 \times 10^{16} \text{ cm}^{-3}$ with high reproducibility.

2. GaAs Growth on Recrystallized Germanium Thin Films

The adaptation of the single-crystal growth method discussed above to low-cost GaAs films is, of course, one important step for achieving the ultimate goal of this research task.

In an earlier portion of this reporting period, a few OM-CVD GaAs films were grown by Rockwell International on JPL-supplied recrystallized Ge/W substrates. However, most films obtained were p-type, with and without the use of HCl vapor, until the samples were recycled by GaAs etch removal at least three or four times. The occurrence of p-type layers were found to be due to copper contamination introduced in the germanium film during e-gun vacuum deposition, as discussed earlier. For these few n-type GaAs thin films grown by Rockwell with typical growth temperatures of 700°C, most portions of the films showed low breakdown voltage and large shunt currents when SB devices were made on them. However, there were a few locations on some of the n-type samples where good values of I_{sc} were observed when intentional oxidation was added for AMOS processing. The contamination problems associated with transporting Ge/W substrates and GaAs/Ge/W samples between JPL and Rockwell may have played an important role, since the normal chemical surface treatment used for single crystal AMOS solar cells could not be used on polycrystalline GaAs thin films, due to excessive surface roughness resulting from preferential etching. After investigation of the growth of undoped and doped GaAs on single-crystal substrates at JPL, a preliminary investigation on the growth of GaAs on recrystallized Ge/W substrates was begun late in this reporting period.

The hetero-epitaxial CVD growth of GaAs on recrystallized Ge thin films was studied, with growth temperatures ranging from 550 to 700°C, an As/Ga mole ratio of 5, (which gave highest mobility values for single crystal), and various H_2S mole fractions. Although tungsten sheet is now being used in the CVD study, parallel studies of the recrystallization of Ge on coated low-cost steel were also

undertaken. Some preliminary results have been presented in the earlier portion of this report. The substrates were Sb-doped n⁺-Ge layers which had been e-beam evaporated to a thickness of 10 μm onto 10-mil W sheets and subsequently recrystallized by a scanning Nd/YAG laser beam, as described earlier.

The surfaces of the GaAs layers usually contained many faceted grains with slightly uneven heights due to the surface condition of the initial Ge layer, and also due to different growth rates on different crystallographic planes. At growth temperatures of 600-750 C, the grains were usually specular in reflection. When growth temperatures below 600 C were used, the polycrystalline GaAs surfaces became rough, and in fact, whisker growth occurred when the temperature was lowered to 550 C.

Figure 3-20 shows a cross-section photomicrograph of a GaAs thin film grown on a recrystallized Ge/W substrate at 600 C using an As/Ga mole ratio of 5, 3 l/min H₂, and a 3.6×10^{-3} mole fraction of TMG. An elemental map of Ga, As, Ge, and W over the same area is also shown in Figure 3-21. By comparing the figures, one can see that the GaAs has filled the existing voids in the original polycrystalline Ge film. Hence, complete coverage of the Ge film by GaAs is expected under the present OM-CVD GaAs growth conditions. This was also confirmed by EDAX analysis which showed no gross Ge signal on the GaAs surface.*

*Very faint Ge signals were observed due to secondary fluorescence. In EDAX analysis, although the electron beam excitation volume is within the top GaAs layer, the As/K α x-ray radiation of 11.9 keV will be able to excite the Ge/K α radiation of 11.1 keV -causing secondary fluorescence. In addition, the broad-band emission spectrum from the GaAs will also cause secondary fluorescence in the Ge.

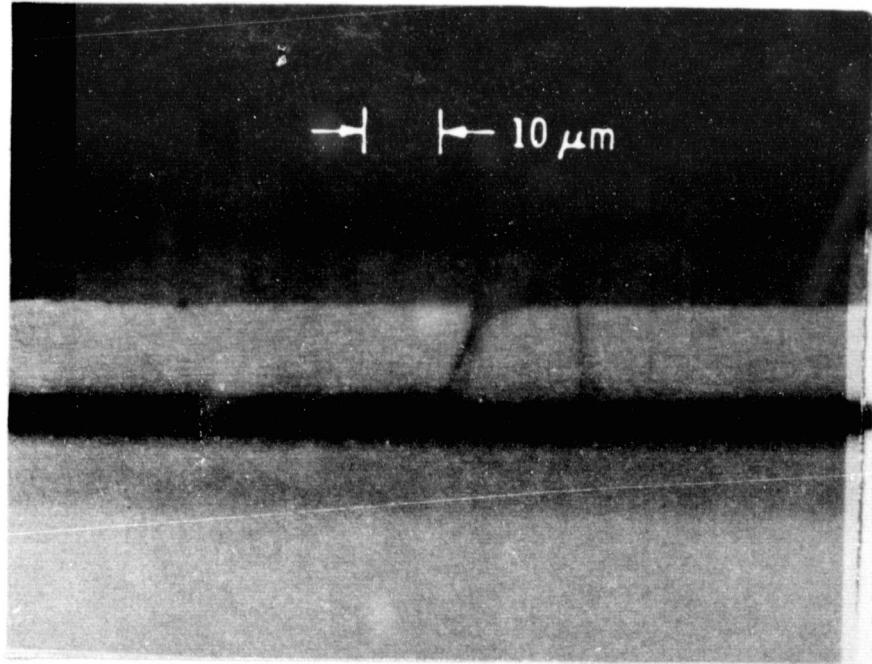
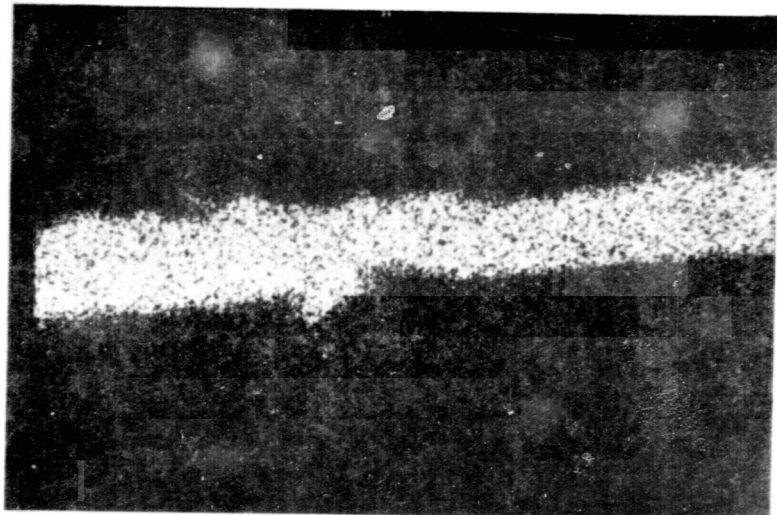


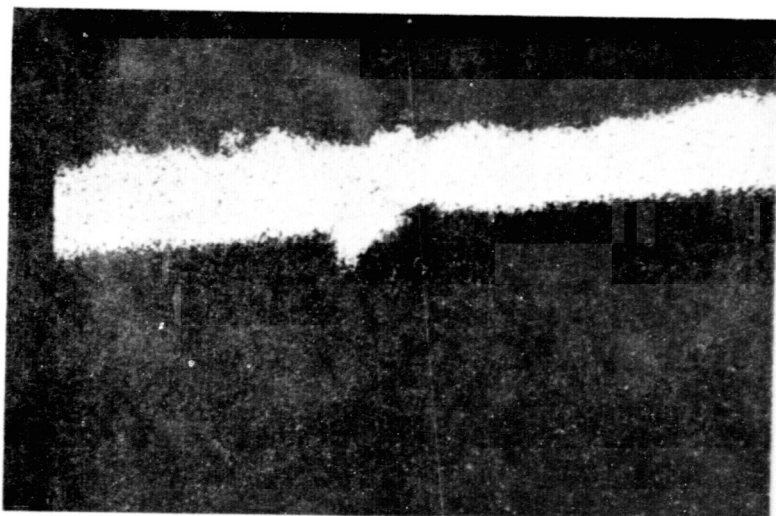
Figure 3-20. Cross-Section Photomicrograph of GaAs Thin Film Grown on Ge/W Substrate

The figures also show the stability of the W, Ge, and GaAs layer structure. One interesting observation is the apparent extension of the crack lines from the recrystallized Ge film into the GaAs. Hence, means to minimize the surface stress during recrystallization of the Ge is under investigation, in order to reduce the number of crack lines and the defect density so as to yield higher quality Ge and GaAs layers.

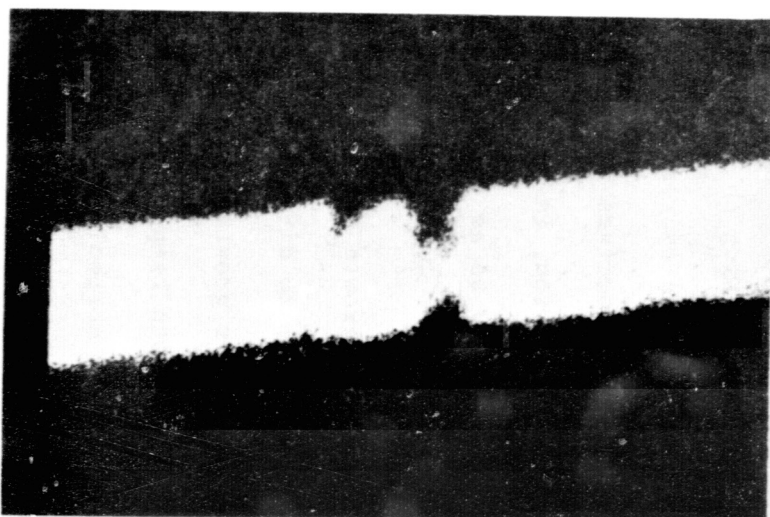
In the hetero-growth of GaAs on polycrystalline Ge thin films, auto-doping by Ge due to diffusion during GaAs growth is an important consideration. Lower growth-temperatures will reduce this effect. However, if the growth temperature is too low, poor crystalline quality and surface morphology will occur, as discussed above. Hence, the optimum growth-temperature was experimentally investigated.



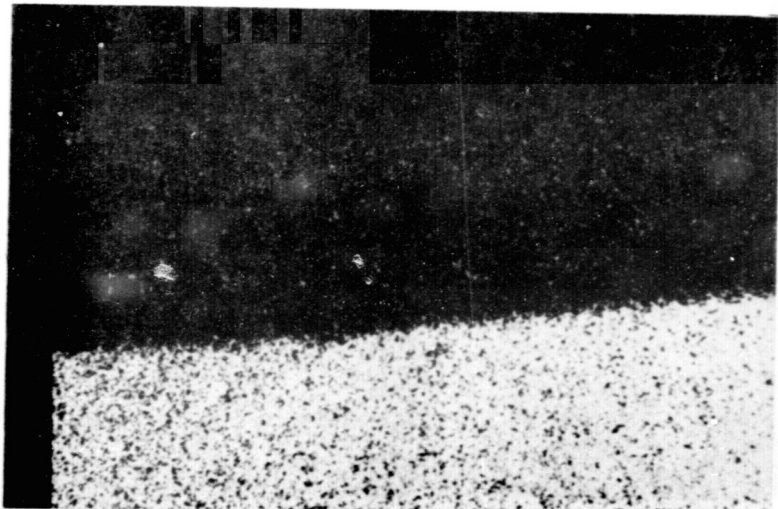
Ga K α



As K α



Ge K α



WL α

Figure 3-21. Elemental Map of Sample in Figure 3-20

Similar to the results of Rockwell's growths, most sample areas in the present work were heavily shunted, when growth temperatures of 650 to 700 C were used. On the other hand, for 600 C growth temperatures, consistently non-shunted characteristics could be observed across the sample surface. However, the best values of I_{sc} observed so far were obtained in the few non-shunted areas of the films grown at 650-700 C. For correlating surface morphology with shunted characteristics, a low-magnification SEM photograph of a sample GaAs film grown at 650 C is shown in Figure 3-22. The approximately triangular-shaped grain shown in the center of this photograph is a region with higher breakdown voltage ($BV > 12$ V), while the remaining area showed low breakdown voltages ($BV < 5$ V). Higher magnification of the "good" ($BV > 12$ V) and "bad" ($BV < 5$ V) regions are presented in Figures 3-23 and 3-24, respectively, to show the detailed structures within those regions. It appears that in the "good" region, very few pits can be found, whereas many surface pits are evident in the "bad" region.

As mentioned earlier, no shunting was observed for 600 C growth. However, variations in the I_{sc} values were observed across the sample surface, such that high values were observed at one edge of the wafer gradually decreasing toward the other edge. In order to ascertain whether the I_{sc} variation was due to the influence of the recrystallized Ge layer or due to the growth environment, several samples were recycled in order to minimize the variables in the Ge substrate. The recycled samples had GaAs grown at 600 C with all growth parameters fixed, except that the samples were rotated 90° with respect to the flow direction of the CVD gas stream. The results showed that the I_{sc} variation is dependent on the direction of the CVD gas stream.



Figure 3-22. Low-Magnification SEM Photograph of GaAs Thin Film Grown on Ge/W Substrate at 650 C

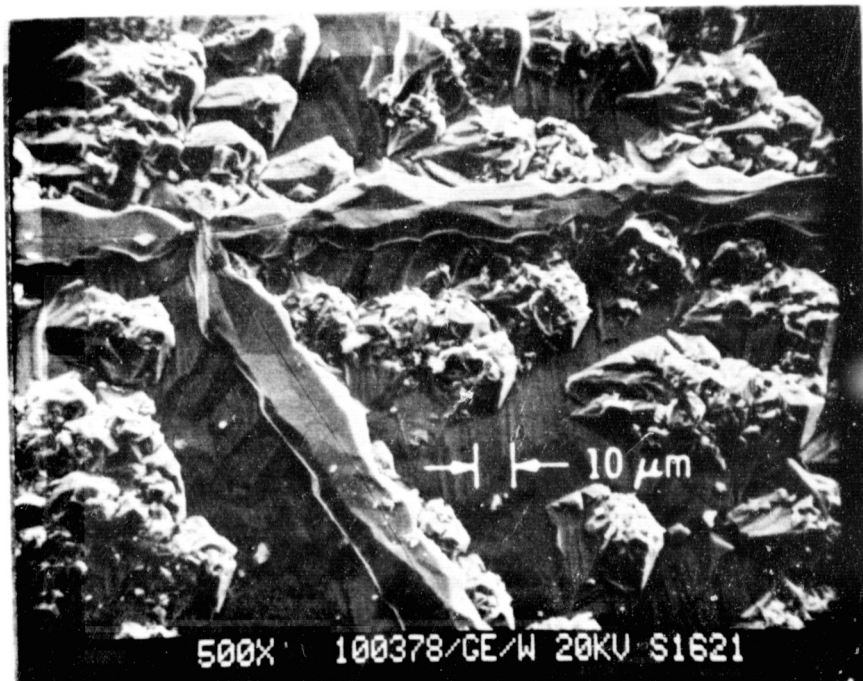


Figure 3-23. High-Magnification SEM Photograph of a Low-Breakdown-Voltage Region Inside Figure 3-22

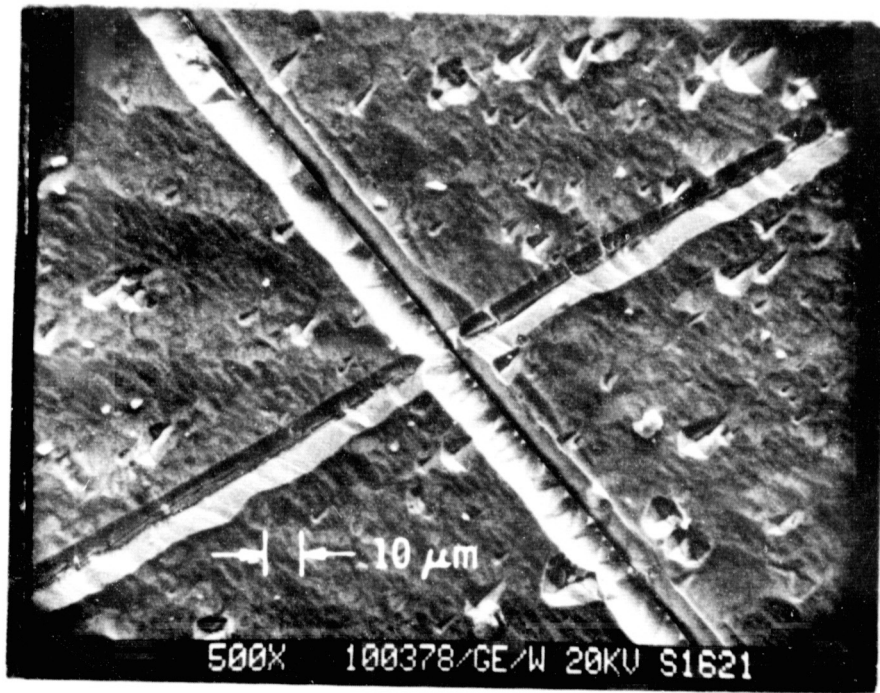


Figure 3-24. High-Magnification SEM Photograph of a High-Breakdown-Voltage Region Inside Figure 3-22

rather than on properties of recrystallized Ge layer. A low-magnification SEM photo of a low- I_{sc} region is shown in Figure 3-25. In this figure, many crystallites protruding from the surface can be seen -- indicating poor epitaxial growth. A higher-magnification SEM photograph (Figure 3-26) reveals more details of the surface and the non-epitaxial growth. The localized I_{sc} response can best be studied by using the Electron Beam Induced Current (EBIC) mode of the SEM, as was recently shown for sliced polycrystalline GaAs (Ref. 29). These studies will be described in the next subsection.

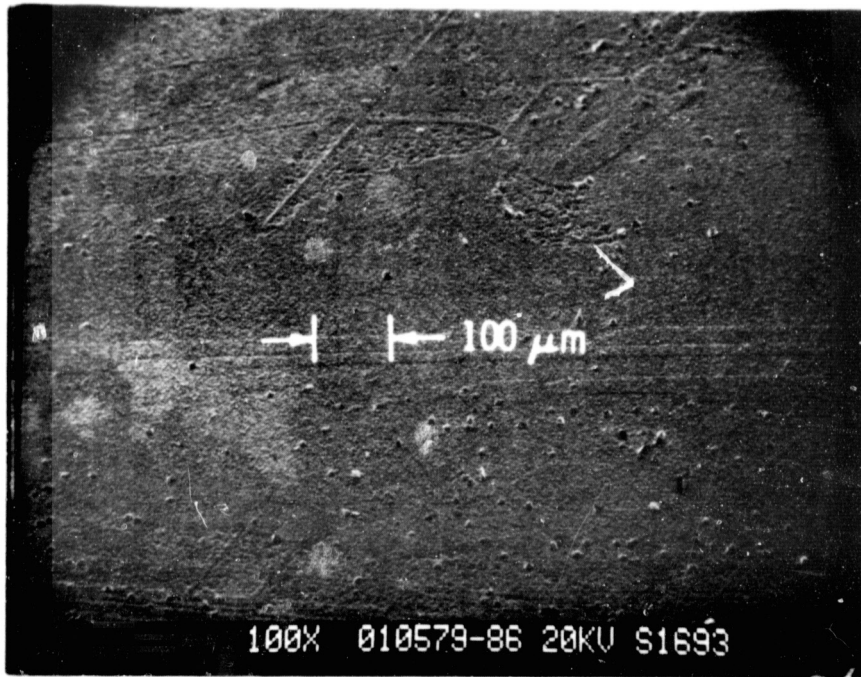


Figure 3-25. Low-Magnification SEM Photograph of a Region with Low Short-Circuit Current

The apparent (or effective) doping concentrations of sulfur-doped polycrystalline GaAs films were obtained by capacitance vs. voltage (C-V) measurements. Schottky barriers were formed on as-grown films by vacuum deposition of silver. Table 3-3 shows the results of typical runs made under various growth temperatures and H₂S flow rates. The corresponding concentration for single-crystal epi-layers grown at the same time are also listed for comparison. The doping concentration values were obtained from SB devices made in the non-shorting regions of the sample substrates. Poor correlation in doping concentration between single and polycrystalline GaAs is seen.

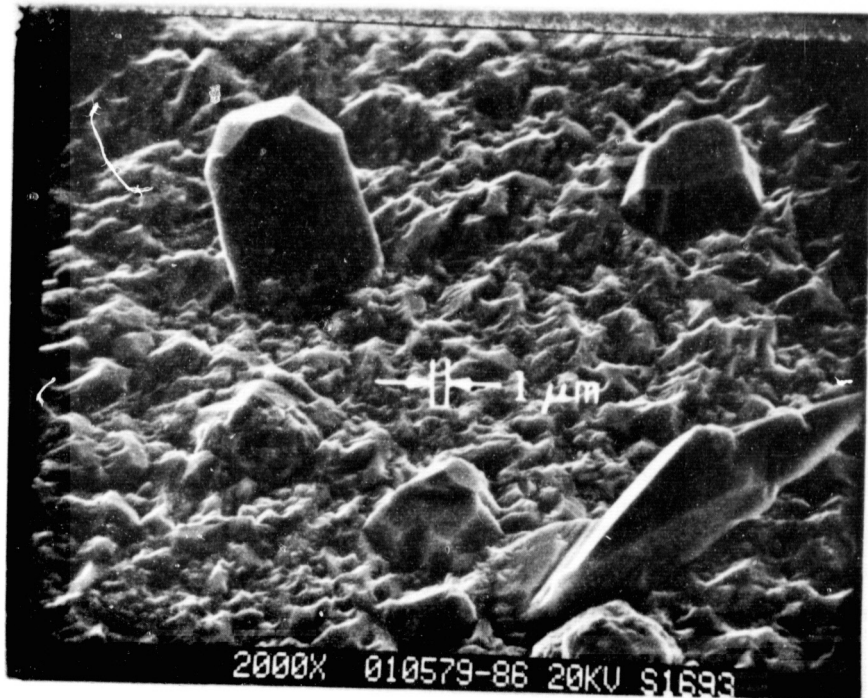


Figure 3-26. High-Magnification SEM Photograph of Sample in Figure 3-25

Table 3-3. Typical Doping Concentrations for Single and Polycrystalline GaAs Films Obtained from C-V Measurements

| Sample | T(C) | H_2S (mole fraction) | Single | $N_D(cm^{-3})$ |
|---------|------|---------------------------|----------------------|----------------------|
| | | | Poly | |
| 121478P | 600 | 1.3×10^{-8} | 9.7×10^{15} | 1.2×10^{16} |
| 121178 | 600 | 1.3×10^{-8} | 9.5×10^{15} | 3.2×10^{15} |
| 121378A | 650 | 1.9×10^{-8} | 3.3×10^{15} | 8.1×10^{15} |
| 121378P | 700 | 6.7×10^{-8} | 6.7×10^{15} | 1.2×10^{16} |

However, GaAs wafers grown at 600 C with H_2S mole fraction from 1.3×10^{-8} to 1.9×10^{-8} resulted in carrier concentrations in the 2×10^{15} to $1.2 \times 10^{16} cm^{-3}$ range - a reasonable doping range -- for AMOS solar cells.

C. THIN-FILM POLYCRYSTALLINE SOLAR CELLS

Although GaAs AMOS solar cells fabricated on sliced polycrystalline GaAs wafers have demonstrated 14% conversion efficiency (Ref. 29), similar values for AMOS solar cells made on polycrystalline GaAs thin films have not been obtainable, requiring further study to improve their performance.

Both baseline (no intentional oxide layer) and AMOS cells were fabricated on GaAs polycrystalline thin-films grown on recrystallized Ge layers. No chemical surface-etching was performed before vacuum deposition of the barrier metal (100 Å of Ag), so as to avoid excessive surface roughening due to selective etching, as explained earlier in this report.

A photograph of a typical array of solar cells consisting of 2-mm circles is shown in Figure 3-27. The photovoltaic response of each circle in the array is shown in Figure 3-28. For this sample, the GaAs film was grown at 600 C with the CVD gas stream flowing from the bottom towards the top in the photograph -- the same direction as the movement of the Ge zonal-melt region. The dashed line shown in the center of the figures indicates the boundary between the unoxidized (left) and Sb_2O_3 -oxidized (right) surface. In the figure, two numbers are shown - the upper number indicating the value of V_{oc} (in volts), and the lower number indicating the value of short-circuit current (in mA) under AM1 (ELH-lamp) illumination. By depositing Sb_2O_3 , constant V_{oc} values of 0.43 - 0.44 V have been obtained in the area with the Sb_2O_3 interfacial layer in contrast to the unoxidized area. No significant influence on the short-circuit current can be seen for the cells with the Sb_2O_3 interfacial layer.

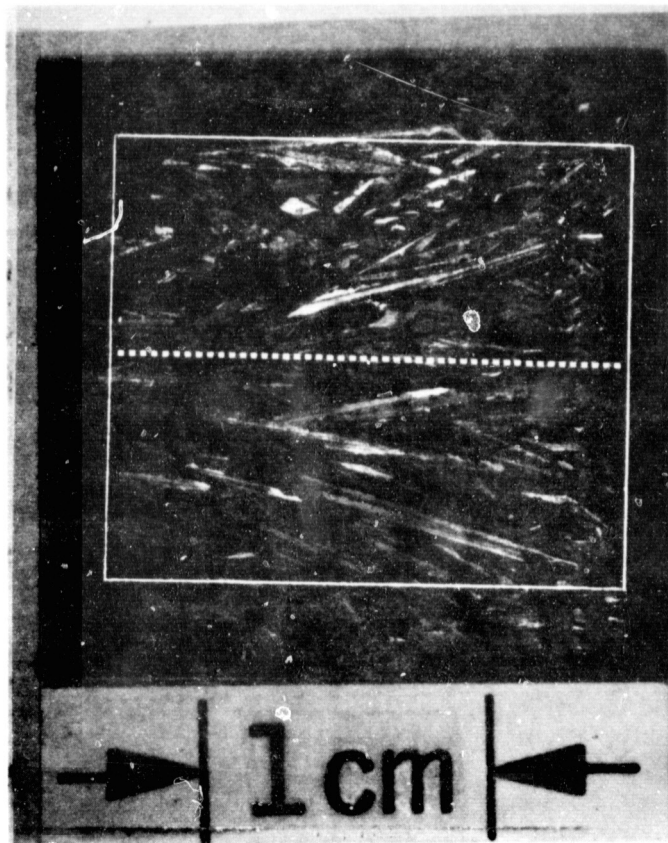


Figure 3-27. Optical Photograph of Thin-Film
GaAs Solar Cells Dot Array

Some correlation between the current output and the CVD gas flow is clearly evident in Figure 3-28. Higher average short-circuit current values are observed on the downstream side (top) of the sample. The exact nature of the correlation is not clear at present. However, it may be due to the turbulence introduced at the leading edge of the sample causing excessive cooling (epitaxial growth cannot be achieved below 600 C), resulting in non-epitaxial, fine-grain growth. Further experiments have been planned to clarify this matter.

| UNOXIDIZED | | | Sb_2O_3 | | |
|------------|-------|-------|-----------|-------|----------|
| 0.367 | 0.212 | | 0.444 | 0.442 | 0.441 V |
| 0.272 | 0.234 | | 0.309 | 0.146 | 0.279 MA |
| 0.370 | 0.366 | 0.357 | 0.436 | 0.442 | 0.442 |
| 0.185 | 0.228 | 0.246 | 0.255 | 0.176 | 0.241 |
| 0.367 | 0.374 | 0.005 | 0.315 | 0.435 | 0.432 |
| 0.193 | 0.268 | 0.033 | 0.242 | 0.185 | 0.130 |
| 0.369 | 0.366 | 0.362 | 0.435 | 0.441 | 0.432 |
| 0.171 | 0.207 | 0.170 | 0.199 | 0.250 | 0.126 |
| 0.361 | 0.355 | 0.362 | 0.435 | 0.455 | 0.432 |
| 0.120 | 0.175 | 0.151 | 0.1301 | 0.140 | 0.140 |
| 0.351 | 0.354 | 0.347 | 0.434 | 0.434 | 0.431 |
| 0.082 | 0.141 | 0.058 | 0.129 | 0.154 | 0.078 |
| 0.346 | 0.352 | 0.344 | 0.438 | 0.427 | 0.440 |
| 0.069 | 0.072 | 0.103 | 0.067 | 0.057 | 0.033 |

Figure 3-28. Diagram of Resulting Photovoltaic Parameters of Sample in Figure 3-27 (see text)

The influence of the local-current collection due to microscopic structures on the polycrystalline thin-film can best be studied by the EBIC mode of the SEM. In this mode, induced current due to minority carriers collected at the SB from electron-hole pairs generated by the scanning primary electron beam is amplified, contrast-enhanced, and displayed on a cathode-ray tube. Figure 3-29 shows a low-magnification (36X) EBIC photograph of a region with poor short-circuit current (lower-left portion of the Sb_2O_3 section with value of 0.067 mA, Figure 3-28). Figure 3-30 shows a SEM photograph of the same portion. For comparison purposes, low-magnification (36X) EBIC and SEM photographs of another region with fair short-circuit current response (upper-left portion of the Sb_2O_3 section with value of 0.309 mA, Figure 3-28) are shown in Figures 3-31 and 3-32, respectively. It is evident that for the region with poor short-circuit current, most of the EBIC photograph is dark, corresponding to poor current collection (see Figure 3-29). However, for the region with fair short-circuit current, most of the EBIC photograph area is bright (see Figure 3-31). By comparing the EBIC photographs and the corresponding SEM photographs, one can see that the darker areas in the SEM photograph correspond to the lighter-colored areas in the EBIC photograph, i.e., the regions with better photocurrent response. Higher-magnification (120X) EBIC and SEM photographs of the same areas are shown in Figures 3-33 and 3-34, respectively, and at even higher magnification (3000X) in Figures 3-35 and 3-36, respectively. The non-epitaxial fine-grain structure is clearly shown as the light-colored areas of the SEM photograph (see Figure 3-36) and as the dark (low current-response) areas of the EBIC photographs (see Figure 3-35).

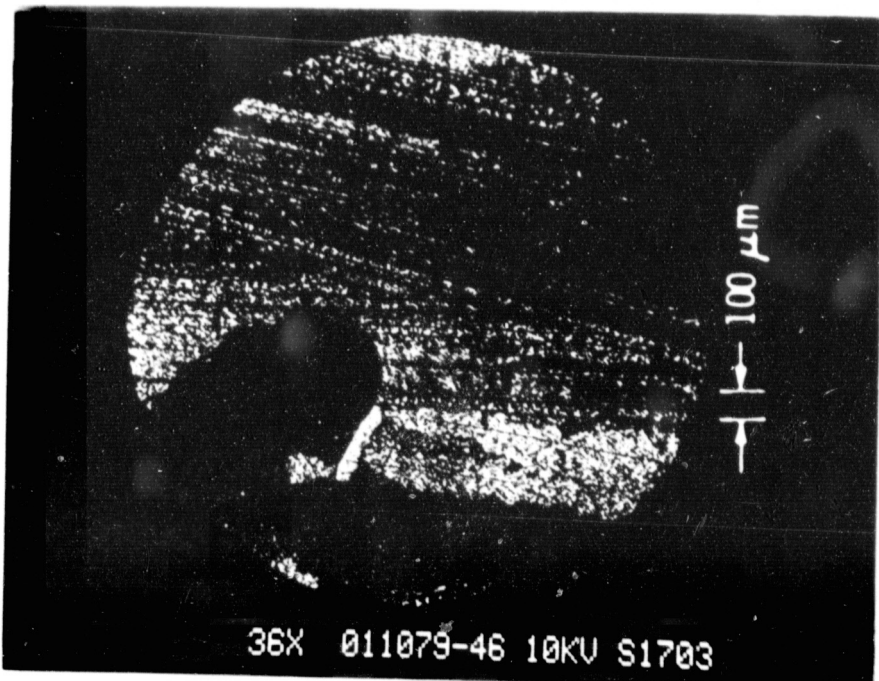


Figure 3-29. EBIC Photograph (36X) of Region with Poor Short-Circuit (see text)

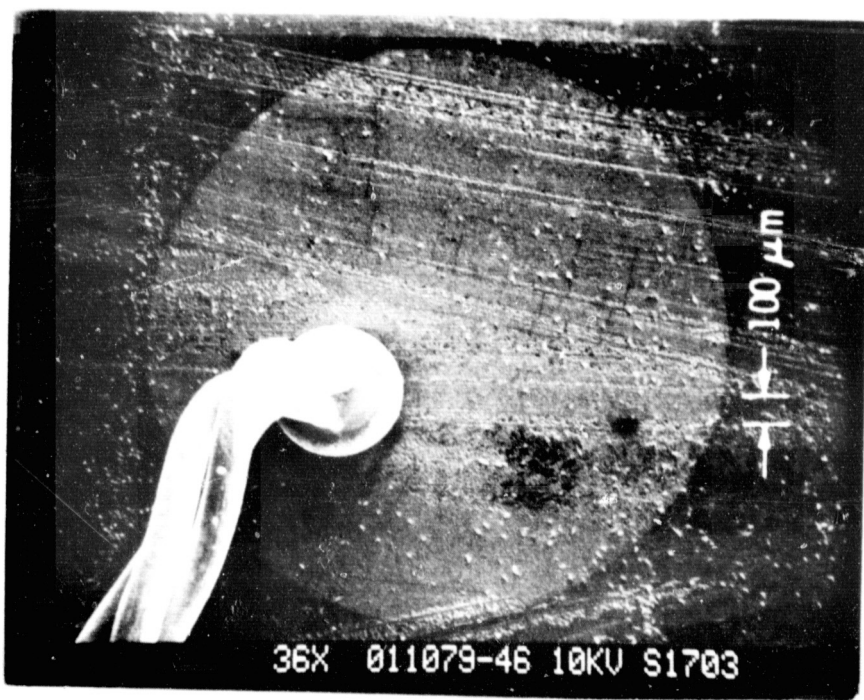


Figure 3-30. SEM Photograph of Same Region Shown in Figure 3-29 (36X)

The smoother surface morphology region shows good current-response, which is clearly seen when comparing Figures 3-35 and 3-36.

In order to obtain quantitative values for the current response of the polycrystalline solar cell, three EBIC signal traces with an identical horizontal displacement scale as used in Figure 3-31 (36X) are shown in Figure 3-37. The three traces were obtained from the EBIC signal while scanning through the upper, middle, and lower regions, as shown by the bright lines in Figure 3-31. The penetration depth of 10-keV electrons is about $0.6 \mu\text{m}$ in GaAs, comparable with the absorption depth of solar radiation. Therefore, the relative current output shown in the EBIC signal should be proportional to the actual photovoltaic response. The peak beam-induced current observed in Figure 3-37 for the three traces is about $2.6 \times 10^{-7} \text{ A}$, identical with the value observed in a single-crystal GaAs solar cell under similar EBIC conditions. Note that in the lower EBIC signal trace of Figure 3-37, there are many areas with nearly constant EBIC-signal current. These correspond to the uniform light-colored areas seen in Figure 3-31. Since a positive correlation on a microscopic scale can be made between current response and surface topology by comparing SEM and EBIC signals, plans were made to make a step-by-step correlation before and after GaAs growth. By doing so, the basic mechanism for lower current-response may be determined and optimum parameters found for Ge recrystallization/GaAs growth.

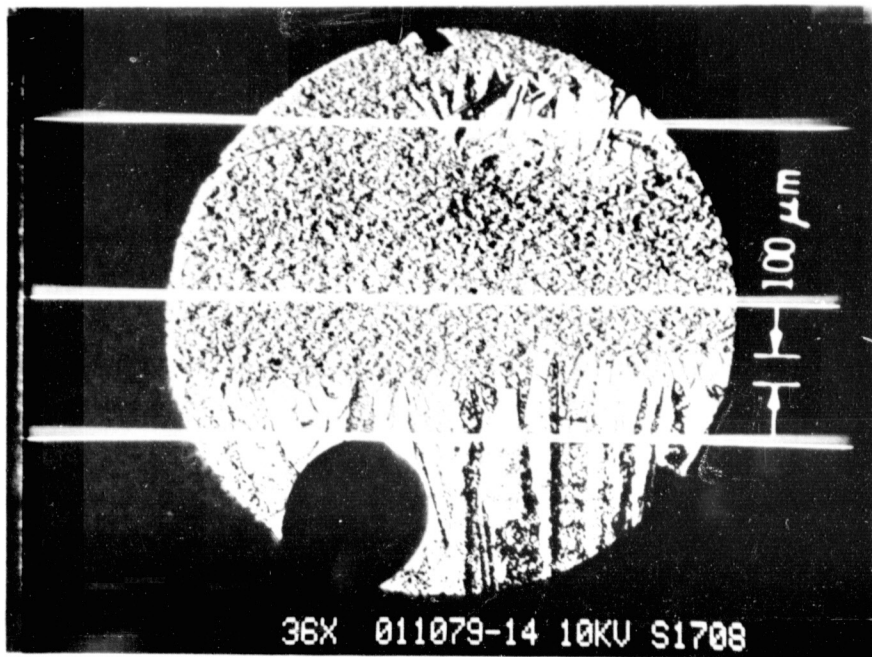


Figure 3-31. EBIC Photograph (36X) of Region with Fair Short-Circuit Current (see text)

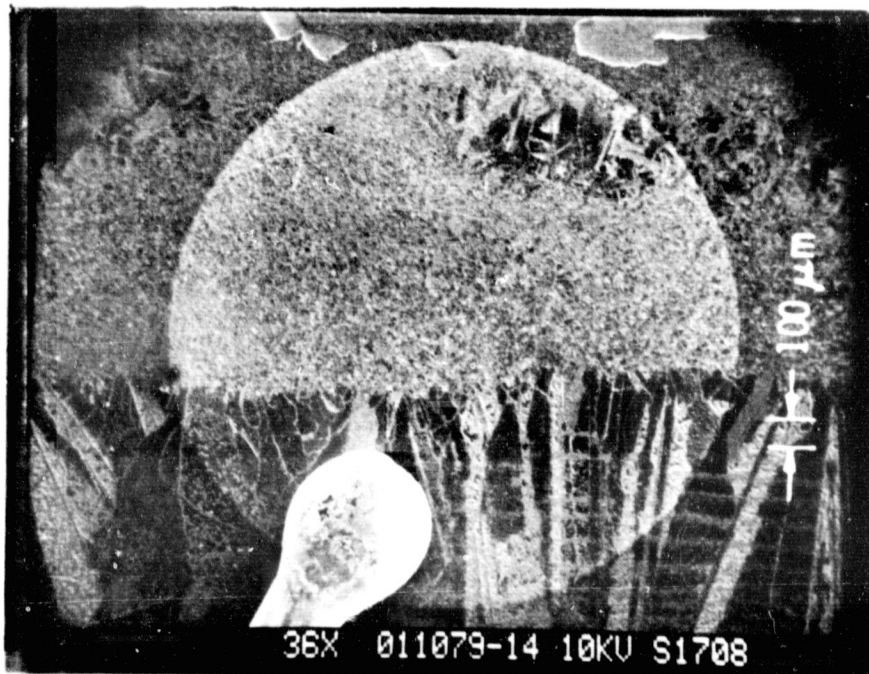


Figure 3-32. SEM Photograph of Region Shown in Figure 3-31 (36X)

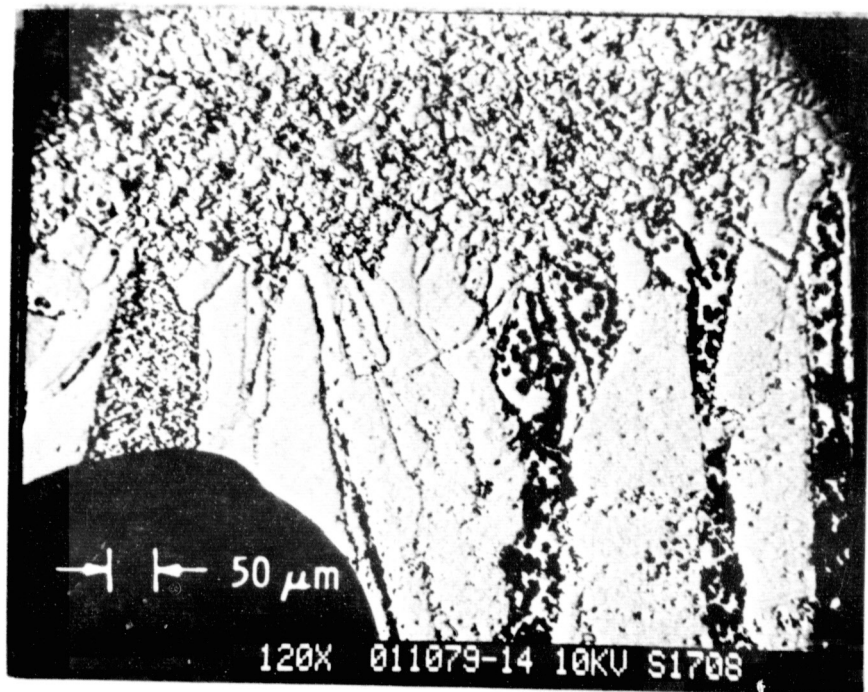


Figure 3-33. Magnified EBIC Photograph of the Region
Shown in Figure 3-31 (120X)

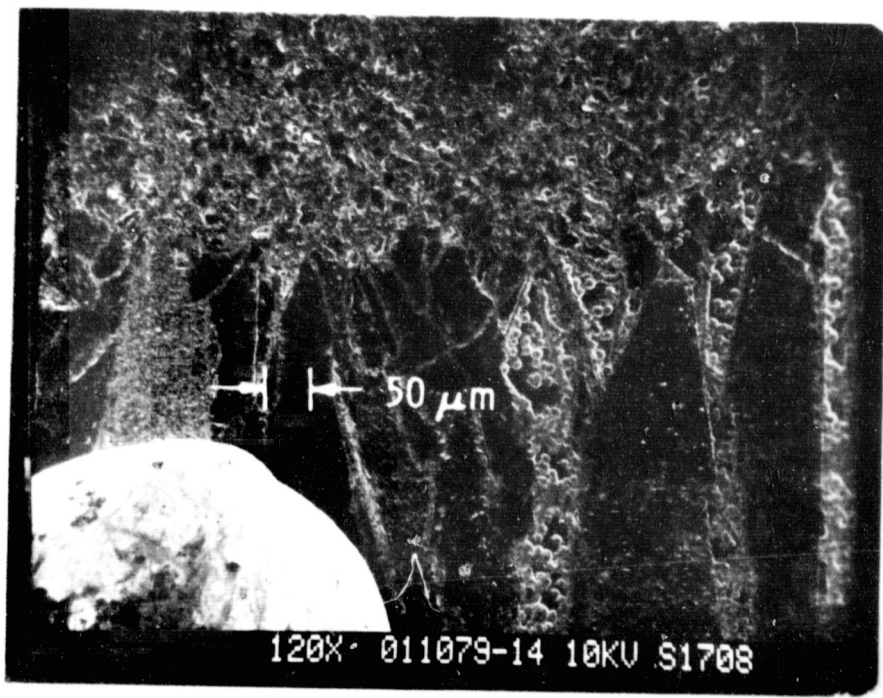


Figure 3-34. SEM Photograph of the Region Shown in Figure 3-33 (120X)



Figure 3-35. Higher-Magnification EBIC Photograph of the Region Shown in Figure 3-31 (3000X)

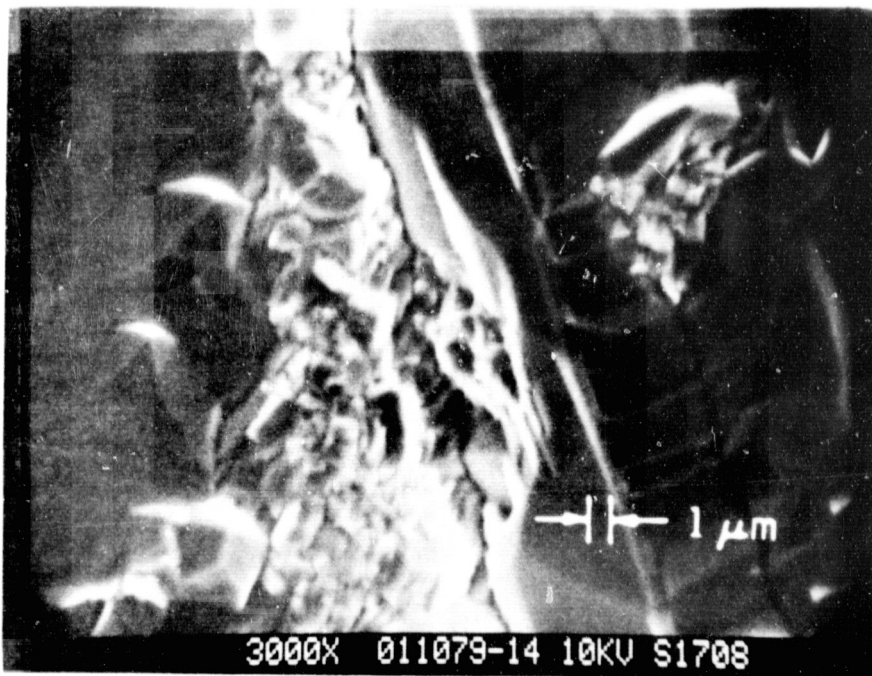


Figure 3-36. SEM Photograph of the Region Shown in Figure 3-35 (3000X)

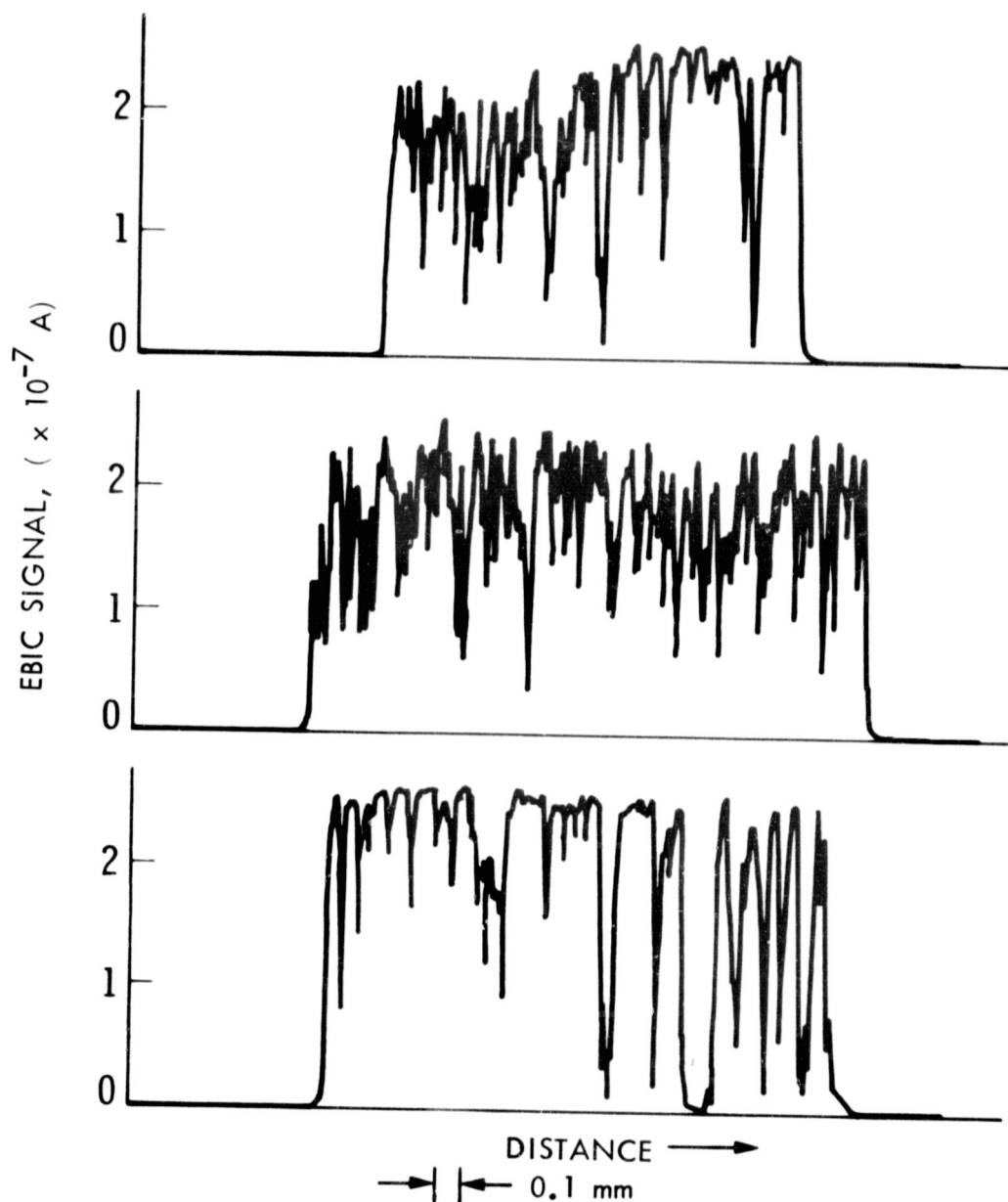


Figure 3-37. EBIC Current Signals Derived From the Three Different Line Locations Shown in Figure 3-31 as Bright Lines

The light I-V curve of the best small area (2-mm diameter circle) AMOS thin-film solar cell is shown in Figure 3-38. This cell was made with 100 Å-thick Ag barrier metal, 38-Å Sb_2O_3 interfacial oxide, and with no antireflection (AR) coating. The GaAs layer was grown at 700 C. The observed I_{sc} value was 14.7 mA/cm^2 , which would increase to about 24.5 mA/cm^2 when an AR-coating is provided. In comparison, the I_{sc} value was about 26 mA/cm^2 , using 60 Å-thick Ag on single-crystal AMOS solar cells. In view of the thicker metal used by the thin-film cell, the short-circuit current density of the thin-film cell should be about the same as that of its single-crystal counterpart because of the large grains, provided the latter has the same metal thickness. The conversion efficiency of this thin-film solar cell is 4.8% (8% if AR coated) at 28 C under AM1 (ELH lamp) illumination. The low observed conversion efficiency of the thin-film solar cell (as contrasted with the single-crystal AMOS cell) stems primarily from its relatively low output voltage and fill factor. The smaller V_{oc} value may be partially due to the variability in enhancement of barrier height caused by the oxide interlayer because of grain orientation effects. More likely, the lower values of V_{oc} and FF are caused by reduced barrier heights at localized surface defects or at grain boundaries. Experiments are planned to clarify these characteristics.

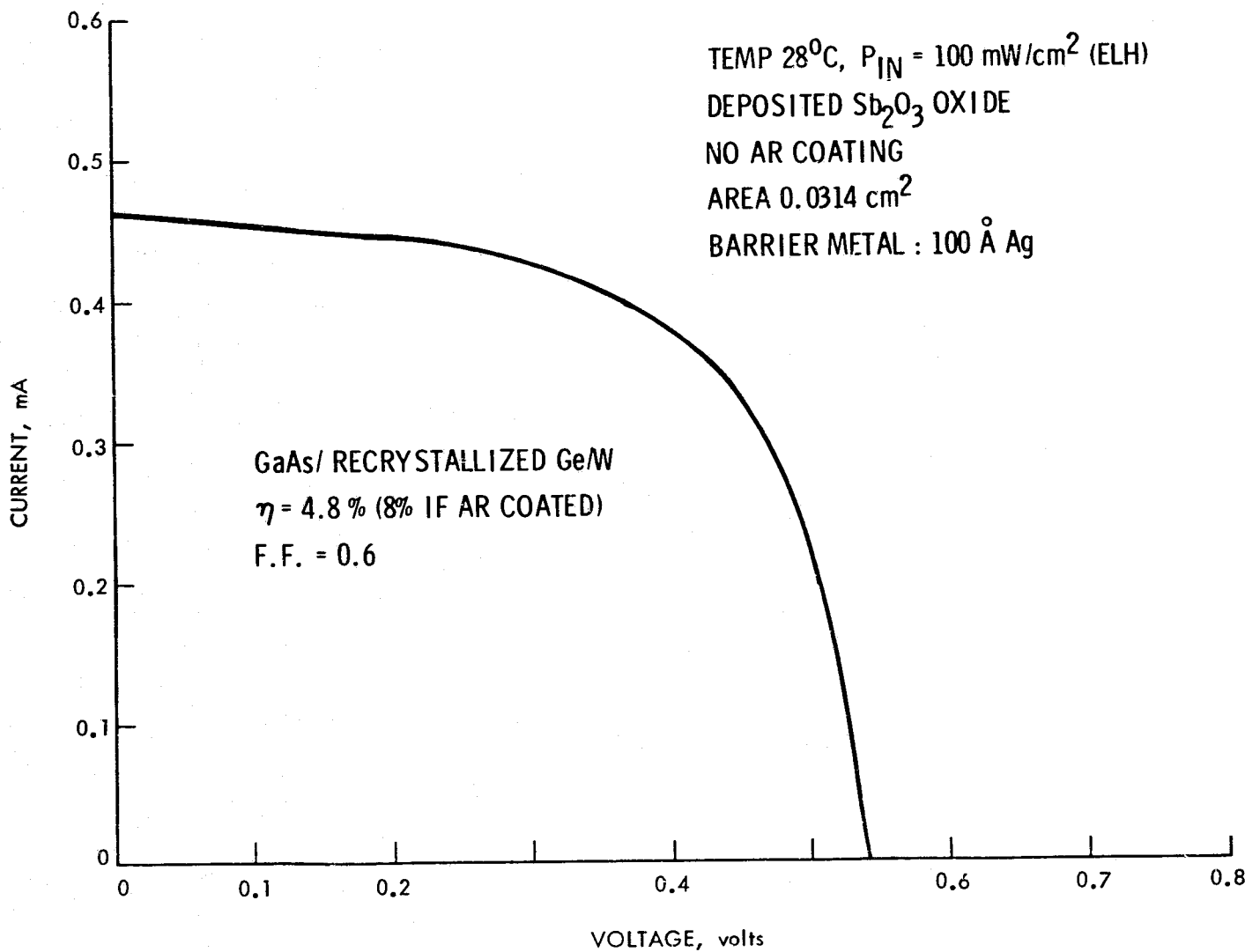


Figure 3-38. Light I-V of the Best Small-Area,
Thin-Film AMOS Solar Cell
in the Array of Figure 3-27

REFERENCES

1. Stirn, R. J., High-Efficiency Thin-Film GaAs Solar Cells, Final Report, JPL Publication 77-60. Jet Propulsion Laboratory, Pasadena, Calif., Sept. 1977.
2. High-Efficiency Thin-Film GaAs Solar Cells, First Interim Report, March 1, 1977 - August 30, 1977, JPL Internal Document 730-9. Jet Propulsion Laboratory, Pasadena, Calif., Dec. 1977.
3. High-Efficiency Thin-Film GaAs Solar Cells, Second Interim Report, September 1, 1977 - February 28, 1978, JPL Internal Report 5030-255. Sept. 1978.
4. Stirn, R. J., and Yeh, Y. C. M., IEEE Trans. Elect. Devices, ED-24, p. 476, 1977.
5. Stirn, R. J., Tech. Digest, 1977 IEDM, p. 48, Washington, D.C., Dec. 1977.
6. Vossen, J. L., Physics of Thin Films, Vol. 9, p. 43. Edited by G. Hass, M. H. Francombe and R. W. Hoffman. Academic Press, New York, 1977.
7. Kim, H. B., Sweeny, G. G., and Heng, I. S., Inst. Phys. Conf., Ser. No. 24, Chap. 5, p. 307, 1975.
8. Guha, S., Arora, B. M., and Salvi, V. P., Solid State Elect., Vol. 20, p. 431, 1977.
9. Stirn, R. J., and Hermann, W. A., Rev. Scientific Inst., Vol. 38, p. 1552, 1967.
10. Hansen, M., and Anderko, K., Constitution of Binary Alloys, Second Edition. McGraw-Hill, New York, 1958.
11. Nicolet, M. A., Thin Solid Films, Vol. 52, p. 415, 1978.
12. van der Pauw, L. J., Phillips Res. Rep., Vol. 13, p. 1, 1958.
13. Chwang, R., Smith, B. J., and Crowell, C. R., Solid State Elect., Vol. 17, p. 1217, 1974.
14. Versnel, W., Solid State Elect., Vol 21, p. 1261, 1978.
15. Blood, P., Acta Elect., Vol. 15, p. 33, 1972.
16. Mott, N. F., and Twose, W. O., Adv. Phys., Vol 10, p. 107, 1961.
17. Matsubara, T., and Toyozawa, Y., Progr. Theor. Phys., Vol. 26, p. 739, 1961.
18. Bass, S. J., and Oliver, P. E., Inst. Phys. Conf., Ser. No. 33b, p. 1, 1977.

19. Andre, J. P., Gallais, A., and Hallais, J., Inst. Phys. Conf., Ser. No. 33a, p. 1, 1977.
20. Bhat, R., and Ghandhi, S. K., J. Electrochem. Soc., Vol. 125, p. 771, 1978.
21. Hicks, H. G. B., and Manley, D. F., Solid State Commun., Vol. 7, p. 1463, 1969.
22. Wolfe, C. M., Stillman, G. E., and Lindley, W. T., J. Appl. Phys., Vol. 41, p. 3088, 1970.
23. Wolfe, C. M., and Stillman, G. E., Appl. Phys. Lett., Vol. 27, p. 564, 1975.
24. Rode, D. L., and Knight, S., Phys. Rev. B, Vol. 3, p. 2534, 1971.
25. Reynolds, D. C., AFAL/DHR, Wright Patterson Air Force Base, Ohio, personal communication (for making the high resolution photoluminescence measurements).
26. Ashen, D. J., J. Phys. Chem. Solids, Vol. 36, p. 1041, 1975.
27. Frolov, I. A., Inorgan. Mat., Vol. 13, p. 773, 1977.
28. Iwasaki, H., and Sugibuchi, K., Appl. Phys. Lett., Vol. 18, p. 420, 1971.
29. Yeh, Y. C. M., and Stirn, R. J., Appl. Phys. Lett., Vol. 33, p. 401, 1978.

APPENDIX A
RESEARCH CONTRIBUTORS

| | |
|----------------|--------------------------------|
| R. J. Stirn | Member of Technical Staff (PI) |
| Y. C. M. Yeh | Senior Engineer |
| Ke-Li Wang | Senior Engineer |
| B. K. Shin | Senior Engineer |
| F. P. Ernest | Senior Engineering Assistant |
| H. Valesquez | Senior Engineering Assistant |
| W. A. Hermann | Engineering Associate |
| B. D. Lamberty | Academic Part-time |
| J. Parsons | Academic Part-time |

END DATE

JUL. 31 1979